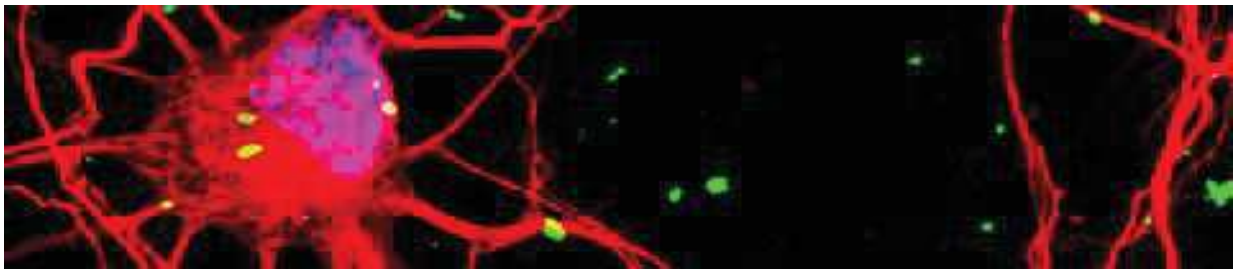

Doctoral School in **Neuroscience**
PhD course in **Neuroscience and Neurotechnology**

Cycle XXX

# Engineering mechanobiology: the bacterial exclusively-mechanosensitive ion channel MscL as a future tool for neuronal stimulation technology

Author: Alessandro Soloperto
Supervisor: Francesco Difato

ISTITUTO ITALIANO DI TECNOLOGIA

UNIVERSITÀ DEGLI STUDI DI GENOVA

# Table of Contents

Conflict of Interest ..... iii

Abstract ..... iv

List of abbreviations ..... viii

List of figures ..... x

CHAPTER ONE: Cell mechanobiology ..... 13

1.1. Introduction ..... 13

1.2. Mechanosensitive ion channels in Bacteria ..... 15

1.3. Mechanosensitive ion channel of large conductance (MscL) ..... 21

1.4. Mechanosensitive ion channels in Eukaryotes ..... 26

1.5. Mechanobiology of the brain ..... 29

CHAPTER TWO: Interfacing the nervous system ..... 35

1.6. State-of-the-art in neuromodulation ..... 35

1.7. Ultrasound stimulation of neuronal circuits ..... 41

AIM OF THE PROJECT ..... 49

RESULTS AND DISCUSSION ..... 51

2. Membrane targeting of the MscL ion channel in primary neuronal cultures ..... 51

3. Electrophysiological characterization of the engineered MscL channel functionality ..... 56

4. Functional characterization of mechano-sensitized neuronal networks ..... 63

5. Ultrasound and optical system integration layout ..... 66

6. Calibration of the ultrasound delivery system ..... 72

7. Ultrasound stimulation of neuronal networks ..... 74

CONCLUSION AND PERSPECTIVE ..... 79
MATERIALS AND METHODS ..... 85
APPENDIX ..... 101
9. PUBLICATION LIST ..... 101
10. PATENT LIST ..... 105
11. ORAL CONTRIBUTION LIST ..... 106
12. POSTER PRESENTATION LIST ..... 106
REFERENCES ..... 107

# Conflict of Interest

I, Alessandro Soloperto, declare that the following dissertation has been written by myself and part of the work here presented it has been published to the Journal of Cell Science (doi: 10.1242/jcs.210393 - Published 19 January 2018) as reported in the Appendix section.

*Genoa*, 28/02/2018

Signature

Alessandro Soloperto

# Abstract

The development of novel approaches to stimulate neuronal circuits is crucial to understand the physiology of neuronal networks, and to provide new strategies to treat neurological disorders.

Nowadays, chemical, electrical or optical approaches are the main exploited strategies to interrogate and dissect neuronal circuit functions. However, although all these methods have contributed to achieve important insights into neuroscience research field, they all present relevant limitations for their use in *in-vivo* studies or clinical applications. For example, while chemical stimulation does not require invasive surgical procedures, it is difficult to control the pharmacokinetics and the spatial selectivity of the stimulus; electrical stimulation provides high temporal bandwidth, but it has low spatial resolution and it requires implantation of electrodes; optical stimulation provides subcellular resolution but the low depth penetration in dense tissue still requires the invasive insertion of stimulating probes.

Due to all these drawbacks, there is still a strong need to develop new stimulation strategies to remotely activate neuronal circuits as deep as possible.

The development of remote stimulation techniques would allow the combination of functional and behavioral studies, and the design of novel and minimally invasive prosthetic approaches.

Alternative approaches to circumvent surgical implantation of probes include transcranial electrical, thermal, magnetic, and ultrasound stimulation. Among

these methods, the use of magnetic and ultrasound (US) fields represents the most promising vector to remotely convey information to the brain tissue. Both magnetic and low-intensity US fields provide an efficient mean for delicate and reversible alteration of cells and tissues through the generation of local mechanical perturbations.

In this regard, advances in the mechanobiology research field have led to the discovery, design and engineering of cellular transduction pathways to perform stimulation of cellular activity. Furthermore, the use of US pressure fields is attracting considerable interest due to its potential for the development of miniaturized, portable and implantation-free US stimulation devices.

The purpose of my PhD research activity was the establishment of a novel neuronal stimulation paradigm adding a cellular selectivity to the US stimulation technology through the selective mechano-sensitization of neuronal cells, in analogy to the well-established optogenetic approach. In order to achieve the above mentioned goal, we propose the cellular overexpression of mechanosensitive (MS) ion channels, which could then be gated upon the application of an US generated pressure field. Therefore, we selected the bacterial large conductance mechanosensitive ion channel (MscL), an exclusively-MS ion channel, as ideal tool to develop a mechanogenetic approach. Indeed, the MscL with its extensive characterization represents a malleable nano-valve that could be further engineered with respect to channel sensitivity, conductance and gating mechanism, in order to obtain the desired biophysical properties to achieve reliable and efficient remote mechanical stimulation of neuronal activity.

In the first part of the work, we report the development of an engineered MscL construct, called eMscL, to induce the heterologous expression of the bacterial protein in rodent primary neuronal cultures. Furthermore, we report the structural and functional characterization of neuronal cells expressing the eMscL channel, at both single-cell and network levels, in order to show that the functional expression of the engineered MscL channel induces an effective

neuronal sensitization to mechanical stimulation, which does not affect the physiological development of the neuronal itself.

In the second part of the work, we report the design and development of a water tank-free ultrasound delivery system integrated to a custom inverted fluorescence microscope, which allows the simultaneous US stimulation and monitoring of neuronal network activity at single resolution.

Overall, this work represents the first development of a genetically mechano-sensitized neuronal *in-vitro* model. Moreover, the developed US delivery system provides the platform to perform high-throughput and reliable investigation, testing and calibration of the stimulation protocols.

In this respect, we propose, and envisage in the near future, the exploitation of the engineered MscL ion channel as a mature tool for novel neuro-technological applications.

# List of abbreviations

| | |
|---|---|
| AAV | adeno-associated virus |
| AP | action potential |
| BSA | bovine serum albumin |
| CNS | central nervous system |
| c/tb | cycles per tone burst |
| DAPI | 4',6-diamidino-2-phenylindole |
| DIV | days *in vitro* |
| DM | dichroic mirror |
| DNA | deoxyriboNucleic Acid |
| DSPC | 1,2-distearoyl-sn-glycero-3-phosphocholine |
| DSEPC | 1,2-dioleoyl-sn-glycero-3-ethylphosphocholine |
| E | elastic modulus |
| ECM | extracellular matrix |
| eGFP | enhanced green fluorescence protein |
| eMscL | engineered mechanosensitive ion channel of large conductance |
| ER | Endoplasmic reticulum |
| ERexp | Endoplasmic reticulum export signal |
| EtOH | ethanol |
| FDA | Food and Drug Administration |
| GABA | γ-aminobutyric acid |
| GOF | gain of function |
| ID | inner diameter |
| LB | Luria-Bertani |
| MFR | mean firing rate |
| MS | mechanosensitive |
| MscL | mechanosensitive ion channel of large conductance |
| MscS | mechanosensitive ion channel of small conductance |

| | |
|---|---|
| Myr-GFP | myristoylated green fluorescent protein |
| NA | numerical aperture |
| OD | outer diameter |
| PBS | phosphate-buffered saline |
| PCR | polymerase chain reaction |
| PDMS | polydimethylsiloxane |
| PEG | polyethylene glycol |
| PFA | paraformaldehyde |
| PRF | pulse repetition frequency |
| RPM | rotations per minute |
| ROI | region of interest |
| RT | room temperature |
| Tbf | tone burst frequency |
| TBS | tris-buffered saline |
| tdTomato | tandem dimer Tomato |
| TMD | transmembrane domain |
| TL | tunable lens |
| TRP | transient receptor potential |
| TTX | tetrodotoxin |
| WT | wild type |
| w/w | weight/weight |
| VGLUT1 | vesicular glutamate transporter |
| VGAT | vesicular GABA transporter |
| US | ultrasound |

# List of figures

Figure 1 | Mechanosensitive ion channel function in prokaryote ..... 16

Figure 2 | Comparison of MscL and MscS ion channels ..... 18

Figure 3 | The bilayer pressure profile ..... 20

Figure 4 | Function and structure of the homopentameric MscL ..... 22

Figure 5 | MscL hydrophobic lock ..... 23

Figure 6 | Changing in conformational structure of the MscL ..... 25

Figure 7 | Gating mechanosensitive ion channels in Eukaryote ..... 27

Figure 8 | Polymodal activation of TREK1 ion channel ..... 28

Figure 9 | Mechanical signals contribute to neuronal growth in the development of the central nervous system ..... 31

Figure 10 | Mechanical properties of body tissues ..... 32

Figure 11 | Mechanical forces are generated and transduced in neurons ..... 33

Figure 12 | State of the art of neuromodulation technologies ..... 36

Figure 13 | Next generation of neurostimulation actuators ..... 40

Figure 14 | Potential applications of ultrasonic neuromodulation ..... 42

Figure 15 | Molecular engineering of the MscL ion channel ..... 52

Figure 16 | Membrane targeting of the MscL-v.2 ion channel ..... 53

Figure 17 | Morphological evaluation of neuron expressing MscL-v.2 construct ..... 55

Figure 18 | Structural analysis of the dendritic tree of single cortical neuron ..... 56

Figure 19 | Electrophysiological characterization of the eMscL channel expressed in primary cortical neurons ..... 58

Figure 20 | Characterization of the activation pressure threshold of the virally-encoded G22S eMscL construct ..... 61

Figure 21 | Mechanical stimulation of neuron expressing the G22S eMscL channel increases its firing rate ..... 62

Figure 22 | Functional characterization of cortical neuronal networks expressing the G22S eMscL channel ..... 65

Figure 23 | Schematic layout of the ultrasound stimulation system integrated in the custom fluorescence microscope ..... 67

Figure 24 | Ultrasound delivery system ..... 69

Figure 25 | Assembly of the ultrasound compatible cell chamber ..... 70

Figure 26 | Computational fluid dynamics study ..... 71

Figure 27 | Acoustical calibration of US delivery system ..... 73

Figure 28 | Ultrasound stimulation of neuronal network ..... 76

Figure 29 | PDMS lid fabrication ..... 94

# CHAPTER ONE: Cell mechanobiology

## 1.1. Introduction

Cells continuously communicate with each other through chemical, electrical and mechanical signals. The classical approach to study cell signaling is based on a biochemical concept, in which biochemical signals in the form of diffusing molecules interact with specific cellular sites, and activate transduction machineries regulating fundamental cellular activities (Kramer et al., 2009). However, cells interact with the surrounding local environment through physical contacts involving the generation and sensing of forces. As in chemical signaling, where a chemical entity interacts with a specific protein binding site to induce changes in the conformational or the phosphorylation states of the protein itself, picoNewton forces can modify the protein structure and activate cellular pathways (Yao et al., 2014).

Typically, we can identify three different routes of force transmission and transduction within cells (Eyckmans et al., 2011). In the first case, the force is directly transduced at the cell membrane by mechanosensitive ion channels, which sense the forces transmitted by the surrounding plasma membrane. These channels are broadly expressed in distinct cell types and respond to different stimuli such as: touch, substrate texture, stretch, vibration, and pressure (Gu and Gu, 2014). Moreover, membrane ion channels respond both to external and internal forces such as osmotic pressure and membrane deformation occurring

during cell reshaping and navigation (Roudaut et al., 2012). The second route for force transmission and transduction is actuated by other macromolecular structures such as cytoskeleton and ECM.

Animal cells possess three main types of cytoskeletal structures: actin filaments, microtubules and intermediate filaments (Fletcher and Mullins, 2010). These structures control the shape, motility and mechanics of cells. Microtubules are the stiffest cytoskeletal filaments presenting complex assembly and disassembly dynamics, which ensure the stabilization of cellular protrusions, shifts and adaptation to the external local environment (Brangwynne et al., 2006a). Actin filaments are much less rigid, present faster dynamics, and they are responsible of cellular motility and formation of adhesion (Kuo, 2013; Nicholson-Dykstra et al., 2005). Unlike the microtubules architecture which is always determined by a single organizing center such as the mitotic spindle (Brangwynne et al., 2006a), the actin cytoskeleton is continually assembled and disassembled in response to local mechanical cues (Cingolani and Goda, 2008). The organization of the whole cytoskeletal architecture plays an important role in fast transmitting compressive and tensile stresses through the cellular compartments, thus inducing a multifactorial cascade of events (mechanotransduction pathways), and eventually leading to modifications of the genetic expression, cell morphology, proliferation, and differentiation (Janmey and McCulloch, 2007; Neukirchen and Bradke, 2011).

At last, upstream mechanosensitive-related molecules that initiate a specific intracellular signaling can also modulate channel activity. In general, direct force transduction, as that actuated by MS channels, triggers a rapid response to force, on the order of tens of microseconds; on the other hand, indirect force transduction mediated by intracellular signaling gives a slower cell response, on the order of milliseconds to few days.

In this regards, it is worth noting that the cellular membranes and organelles behave as a dynamic medium that directly affects the function and spatial

distribution of the proteins embedded in itself (Andersen and Koeppe, 2007; Engelman, 2005), also in response to mechanical cues and forces. Indeed, the plasma membrane responds to forces in a time-varying manner as non-Newtonian fluids (Tyler, 2012), it is responsible of protein clustering and assembly on the cell surface, and have an active role in determining the mechanical properties of the brain (see section: 1.5 Mechanobiology of the brain).

## 1.2. Mechanosensitive ion channels in Bacteria

Among all the cellular constituents, the two more important sensing elements involved in such pathways are the cytoskeleton and the mechanosensitive ion channels. Considering, that not all cells present a cytoskeletal structure, MS ion channels are considered as the oldest and most important mechanosensing element evolved among all the living organisms, in order to transduce local mechanical perturbation provided by either external and internal environment to the cell membrane (Brohawn, 2015; Martinac, 2012). Nowadays, even though we acquired a wide knowledge about the cellular sensing of specific stimuli such as heat, pH, and chemical compounds, our knowledge about how cells can recognize and respond to mechanical forces is still limited. In this regards, the research field of mechanobiology has focused on the understanding of mechanotransduction pathways of the cells.

Bacterial cells, as all living systems, are subjected to a wide range of mechanical stimuli, and therefore they have evolved molecular pathways and mechanisms to sense and respond to such environmental stimuli (i.e. osmotic shock, membrane deformation, gravity, etc.), in order to guarantee proper growth, development and survival (Kung et al., 2010).

Biophysical characterization of MS proteins elucidates the ability of such channels to directly detect, and respond to mechanical forces exerted on the lipid bilayer. Today we know that bacteria cells are equipped with MS channels to balance their intracellular osmolarity (Perozo, 2006) during the navigation in

rapidly changing environmental conditions, which could generate severe osmotic shocks (Figure 1), in order to preserve the cell membrane from the lysis (Booth and Blount, 2012; Peyronnet et al., 2014).

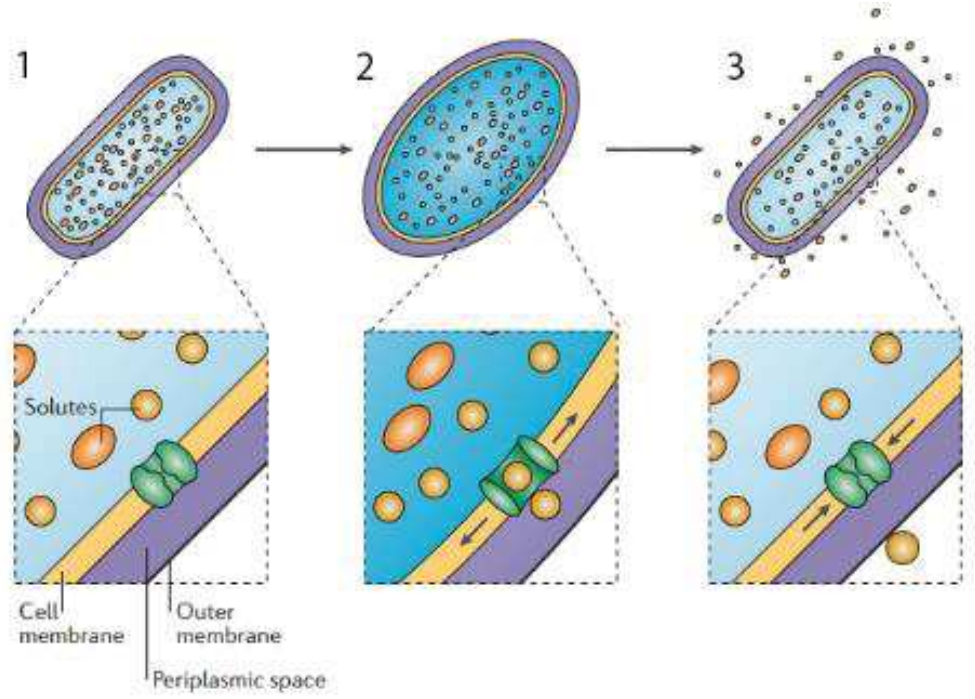


**Figure 1 | Mechanosensitive ion channel function in prokaryote**
In the prokaryotic cells, the mechanosensitive ion channels act as osmotic 'safety valves' (a generic Gram-negative bacterial cell is shown). When cells are in an osmotic equilibrium (1) with their environment, the channels remain closed; while when the environment becomes hypo-osmotic (2), water enters into the cell, and dramatic changes in the internal pressure lead to the channel opening and the release of cytoplasmic solutes (i.e. ions and small molecules) in order to achieve a rapid reduction of the inner pressure. Then, the quick equilibration of the internal and external osmotic pressures (3) induces the channel closure (image extracted from Perozo, 2006).

For example, a hypo-osmotic shock induces a huge water uptake by the bacterial cell with a rapid volume expansion: a typical 30% increase of the cell volume occurs in less than 1 second (Boer et al., 2011). During the water inflow, the cell can increase its surface area as well as exploit membrane reservoirs through regulated exocytosis, to avoid a net increase of the pressure acting on the membrane. However, bacterial cells lack an extensive phospholipid reserve, and an increasing in terms of distance between phospholipid head groups could generate only a 2-4% membrane expansion. Therefore, the successful withstanding of such augmented turgor pressure, which pushes the plasma

membrane against the cell wall during an osmotic shock, depends on the gating of specifically evolved mechanosensitive ion channels (Hamill and Martinac, 2001). When the maximum expanded state of the bacterial membrane is reached, the turgor pressure rise reaches about 0.1 ATM, and the gating of MS channels occurs (Boer et al., 2011), thus producing the efflux of cytoplasmic solutes and the reduction of the turgor pressure.

Unlike bacterial cells, eukaryotic cells have a cytoskeletal structure linked to the lipid bilayer. Such cytoskeleton, which passively transmits external forces, allows the cell to swell without increasing the total bilayer area or tension. Therefore, MS currents in eukaryotic cells cannot be detected in whole cells, but only in excised patches or membrane blebs where the cytoskeleton is absent (Morris and Horn, 1991).

The composition of the plasma membrane can influence the opening of MS channels: variations in the thickness of phospholipid bilayer or the addition of compounds inducing spontaneous membrane bending could modulate the tension required to open MS channels (Perozo et al., 2002a). For example, adding cationic amphipaths to the membrane can change the membrane geometry and lipid solubility inducing a reversible activation of MS ion channels when a lipid monolayer is present (Perozo et al., 2002a).

Therefore, the cell fate upon an osmotic shock is determined by turgor pressure, number of MS channels, strength of cell membrane, and more important by the rate of change of the osmolarity (Bialecka-Fornal et al., 2012; Kakuda et al., 2012).

After the first report on the discovery of MS channels in *Escherichia coli* (Martinac et al., 1987), multiple types of bacterial MS channels have been identified (Edwards et al., 2012). Today, two major classes of bacterial MS channels are recognized: MscS (Levina et al., 1999) and MscL (Sukharev et al., 1994). MscS and MscL are so called in regard of the amount of ions passing through the channel pore (channel conductance), which is around 1 nS or around 3 nS, respectively (Figure 2, (Martinac, 2004)).

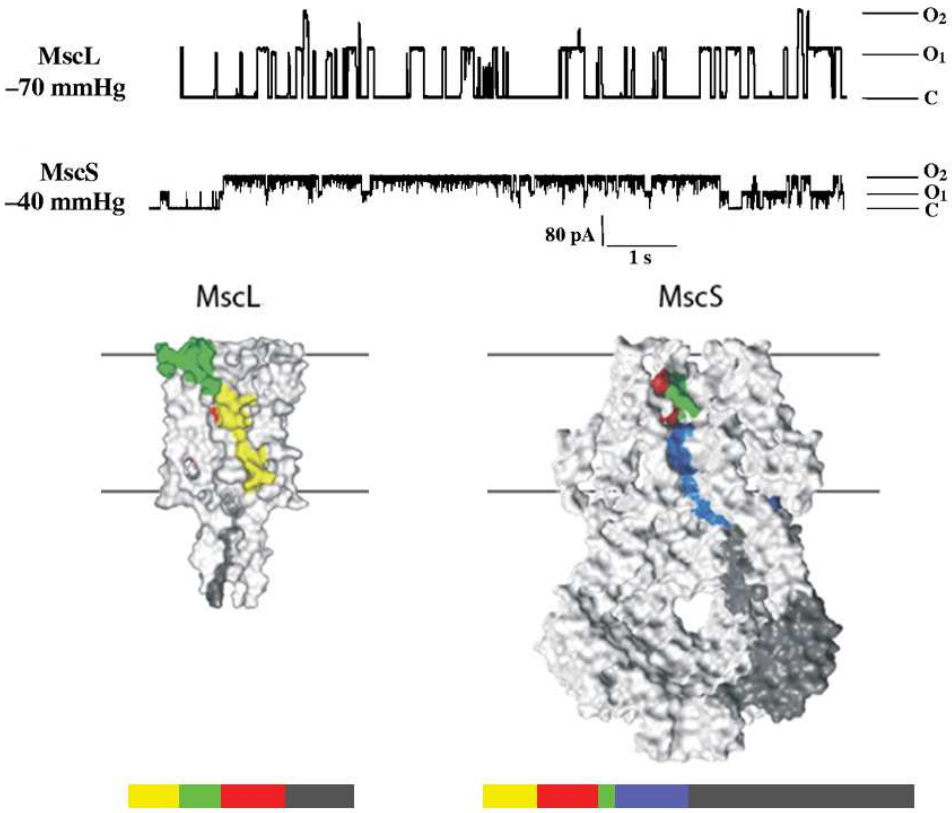


**Figure 2 | Comparison of MscL and MscS ion channels**

Top panel: Example of current traces of MscL and MscS channels recorded at a pipette voltage of +40 mV and +30 mV, respectively, in *E. coli.*; C and O indicate the closed and open state of the channel and the footstep number the amount of opened channels (image extracted from Martinac, 2004).

Bottom panel: the comparison of structures of the MscL and MscS channel is shown. The color map indicates the different structural elements of each channel. Yellow: TMD1; Green: periplasmic loop; red: TMD2; cyan: TMD3; grey: C-terminal (images extracted and modified Bezanilla and Perozo, 2002).

Moreover, these two membrane ion channels directly respond to changes in membrane tension by opening a pore of 6 Å and 30 Å diameter, respectively (Kloda et al., 2008a), thus indicating that MS channels could be gated without the requirement of any other cellular components such as the cytoskeleton or extracellular matrix (Häse et al., 1997; Martinac et al., 2014). Unlike MscL, the MscS channel shows also a marked voltage-dependence behavior in depolarizing conditions but little is yet known regarding its membrane potential sensitivity (Bezanilla and Perozo, 2002; Martinac et al., 1987).

In addition, although these two channels belong to distinct MS channel families, they present relevant sequence similarities at the transmembrane domain (TMD) constituting the channel pore (TMD1 of MscL and TMD3 of MScS), indicating a common evolutionary origin (Kung et al., 2010; Martinac and Kloda, 2003).

Martinac and coworkers identified both channels in 1987 by measuring unitary currents steps, through voltage-clamp recordings of giant *E. coli* spheroplasts subjected to pipette suction or to dilution of the solution bathing the patch (Martinac et al., 1987). However, only few years later it was proved that the expression of two MS channel proteins were necessary to the bacteria survivability upon an osmotic shock (Levina et al., 1999). The possibility to easily isolate large amounts of the MscL channel from many bacterial strains, and to reconstitute it in a cell-free system has been exploited to study the mechanical and electrophysiological properties of MscL and MscS (Häse et al., 1995; Sukharev et al., 1993).

In details, MscL can reconstitute into azolectin liposomes with a protein/lipid ratio as low as 1:10000 w/w, while MscS requires an higher reconstitution ratio, 1:200 w/w (Sukharev, 2002). However, many methods for incorporating both MscL and MscS into liposomes are now available, and the use of such cell-free systems have allowed studying the interaction of these MS channels with lipid interfaces. The periplasmic and cytoplasmic regions can modulate the interaction of MscL and MscS with the surrounding phospholipids (Meyer et al., 2006; Tsai et al., 2005; Yang et al., 2013), indicating that the cell membrane composition may actively modulate the MS channel activity (Pliotas et al., 2015). In this regard, Perozo and coworkers demonstrated that the hydrophobic mismatch between the MscL and the lipid membrane does not trigger the MscL opening, but specific mismatches could stabilize some intermediate states towards the fully open state (Bavi et al., 2016; Perozo et al., 2002b). On the contrary, the hydrophobic mismatch doesn't play a significant role in MscS (Nomura et al., 2012).

Nevertheless, the internal bilayer lateral pressure profile due to the interaction between membrane constituents (Figure 3), and the difference in size of their TMDs with respect to the bilayer thickness, may be involved in regulating the conformational changes of MscL and MscS (Meyer et al., 2006; Nomura et al., 2012).

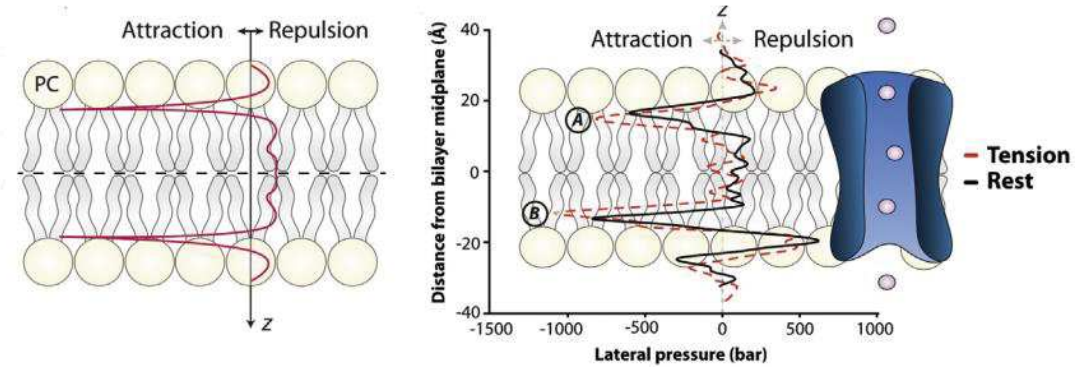


**Figure 3 | The bilayer pressure profile**

In the left panel, an idealized symmetrical bilayer pressure profile showing characteristic negative peaks at the water-lipid interface and repulsive positive peaks in the head group and tail region. In the right panel, a bilayer pressure profiles from molecular dynamics simulation of a bilayer with MscL inserted in it. Black line is the lateral pressure profile at rest, and red is in the presence of applied tension. Note how in the presence of the protein the pressure profile in a largely symmetrical lipid bilayer has become distinctly asymmetric. Peak A and peak B represent the rise in the pressure profile at lipid solvent interface (image extracted form Bavi et al., 2016).

The amphipathic nature of the lipid molecules and the presence of surrounding water makes the lateral pressure profile of the cell membrane intrinsically inhomogeneous. When MscL channels are embedded in the lipid bilayer, the latter shows an increase in intrinsic asymmetry at the lipid-water interface (Bavi et al., 2016; Cox et al., 2017). However, the effect of varying lipid composition or tension on the channel gating has not been investigated experimentally yet.

On the other hand, molecular dynamics studies have revealed that changing the hydration properties of the MscL pore leads to a change in the energy required for gating the channel (Birkner et al., 2012).

Indeed, increasing the pore hydrophilicity of a single subunit at position 22 in the MscL pore domain, it is sufficient to induce the channel opening in the absence of any applied tension.

Nowadays, genome sequencing revealed a much greater variety of MS channel across the bacterial kingdom (Kloda and Martinac, 2001), and such heterogeneity produces a variety of responses to hypo-osmotic shock, in terms of ion conductance: from 100 pS up to several nS. Over the course of evolution, different organisms have fashioned unique solutions that reflect their environmental niche (Martinac and Kloda, 2003). Indeed, distinct MS channel types offer different temporal responses for less severe hypo-osmotic stress, and their abundance allows rapid reduction of the turgor pressure (Booth, 2014).

## 1.3. Mechanosensitive ion channel of large conductance (MscL)

Between the variety of bacterial MS ion channels, the mechanosensitive ion channel of large conductance (MscL) is the first to have been discovered. MscL was isolated for the first time by the Kung's group in 1994 in giant *Escherichia coli* spheroplasts (Sukharev et al., 1994; Sukharev et al., 1997), and after decades of biophysical investigation, today it represents the most studied and characterized mechanosensitive ion channel.

In bacterial cells, MscL plays a key role as a biological emergency release valve through the release of cytoplasmic osmolytes upon osmotic shock. When MscL-knockout cells are subjected to a down shock assay, they show poor survivability, thus indicating that the MscL gene is necessary for sensing the membrane deformation occurring during the cell swelling (Levina et al., 1999).

The mechanosensitivity of the MscL channel was quantified on liposomes engineered with MscL protein isolated from *E. coli* (Eco-MscL). The membrane tension required to gate the channel was estimated to about ~12 $mN \cdot m^{-1}$ (Chiang et al., 2004; Moe and Blount, 2005; Sukharev et al., 1999), which reflects a tension near the lytic limit of the membrane itself, and the channel opening occurs

around 3-5 μs after the tension reaches such activation threshold (Shapovalov and Lester, 2004). It is worth noting that such experiments also indicate that only tension in the membrane bilayer gates MscL ion channel without requiring other cellular elements.

The MscL channel structure was resolved for the first time from the MscL homologues isolated in *Mycobacterium tuberculosis* (Tb-MscL), which presents a 67% similarity when compared to Eco-MscL, by X-ray crystallography at a resolution of 3.5 Å (Chang et al., 1998). However, the crystal structure of the channel was resolved only in its close state, while the open state conformation has been simulated through molecular dynamic studies (Perozo et al., 2002b).

The crystallography studies revealed a pentameric structure of five monomers organized around a central pore (Figure 4).

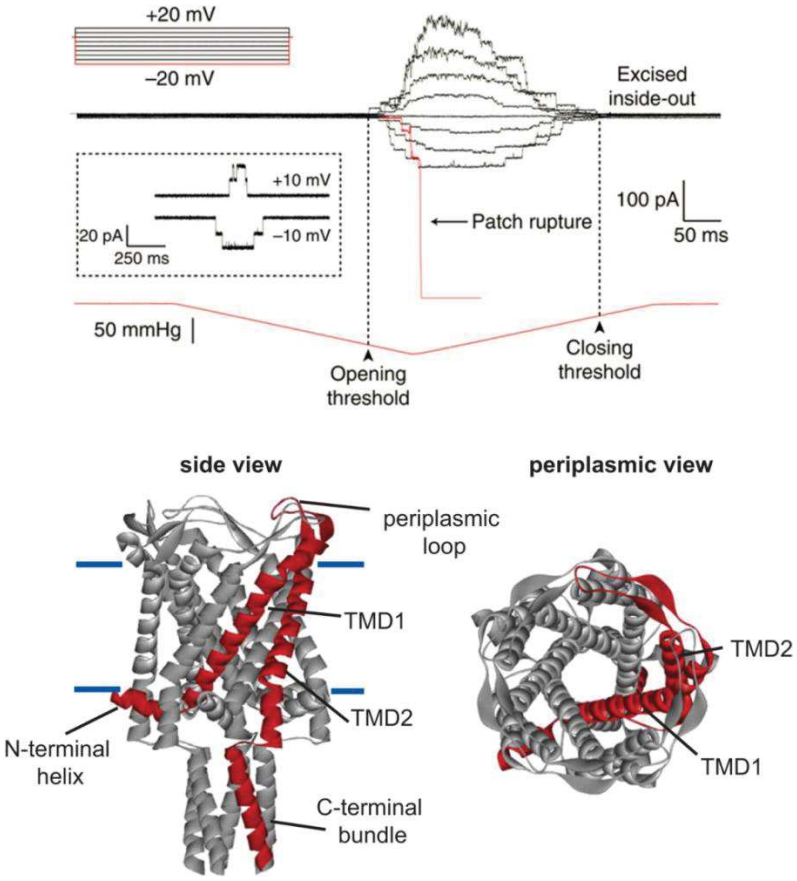


**Figure 4 | Function and structure of the homopentameric MscL**

Top panel: MscL current activity in an excised inside-out patch in response to pressure ramps (300 s to peak) at voltages ranging from +20 to −20 mV (image extracted from Cox et al., 2016).

Bottom panel: Tb-MscL is used as model for determining the structure of the Eco-MscL. The horizontal blue lines indicate the approximate collocation of MscL in the lipid membrane. The N-terminal helix lies along the membrane in the intracellular side. TMD1 crosses the membrane, shaping the pore of the channel, and connects the TMD2 by a periplasmic loop. TMD2 creates the protein-lipid interface. Finally, a cytoplasmic loop connects TMD2 with the C-terminal bundle at the C-terminal end of the channel (image extracted from Iscla and Blount, 2012b).

The non-selective pore size of about 30 Å allows the release of large compounds (Cruickshank et al., 1997), reaching a channel conductance value up to 3 nS (Kloda et al., 2008b). Each monomer is composed of 136 amino acids, organized in two transmembrane α-helices domains with both amino (N-terminal), and carboxyl (C-terminal) tails located on the cytoplasmic side of the membrane (Chang et al., 1998).

The first transmembrane domain (TMD1) forms the channel pore, while the second transmembrane domain (TMD2), located in the lipid bilayer, senses the lipid contents of the membrane, and it is involved in the channel self-assembly. The two domains are connected by a periplasmic β–sheet loop. The constriction point (Figure 5) of the pore of 2 Å occurs at the cytoplasmic half of TMD1 at position 22, and constitutes a hot-spot site where mutations led to gain of function (GOF) phenotypes of the channel (Woe et al., 1998; Yoshimura and Sokabe, 2010).

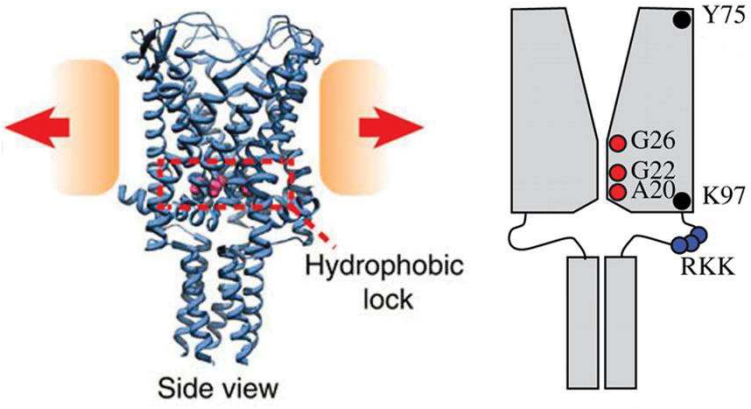


**Figure 5 | MscL hydrophobic lock**

Cartoon of Eco-MscL structure with reference to the hydrophobic lock. The pore is constricted between A20 and G26. Y75 and K97 describe the extremities of the TMD2 interfacing the lipid bilayer. Gating threshold changes with the hydrophilicity of G22. Charged residues RKK are

involved in oligomer assembly (image extracted and modified from Yoshimura and Sokabe, 2010).

In this region, the substitution of a residue with a hydrophilic amino acid decreases the energy barrier to open the channel, thus increasing the mechanosensitivity of the channel, and concomitantly decreasing the channel dwell time (the amount of time a channel remains in the closed position) (Birkner et al., 2012; Kocer, 2015).

Furthermore, while the C-terminal region is not necessary for the channel function, the deletion or mutation on the N-terminal disrupts the channel function (Blount et al., 1996; Iscla et al., 2008).

MscL shows structural similarities with other eukaryotic MS ion channels such as the ATP-gated cation channel, the inward-rectifier potassium channel and the epithelial sodium channel (North, 1996). Although a recent crystal structure of MscL from *Staphylococcus aureus* shows a tetrameric complex (Liu et al., 2009), this appears to be a detergent-specific oligomeric organization not reflecting a physiological state (Dorwart et al., 2010).

The opening mechanism of the channel was first hypothesized by Sukharev in the 2001 and described in the so called Sukharev-Guy (SG) gating model (Sukharev et al., 2001). The suggested model, known also as "iris opening mechanism" (Betanzos et al., 2002; Perozo et al., 2002b; Sukharev et al., 2001), suggests that during the increase in membrane tension the TMD1 rotates within the thinning membrane portion, thus causing the opening of the channel pore (Figure 6). The possibility to isolate large amounts of channel from many bacterial strains, facilitates the design and development of genetically modified variants of the MscL (Maurer and Dougherty, 2003), and attracts a lot of attention in exploiting the MscL channel in medical and biotechnological applications (Iscla et al., 2013).

Moreover, MscL can be translated *in-vitro* (Berrier et al., 2004) or synthetically synthesized (Clayton et al., 2004), reconstituted into lipids and self- assembled

into a functional complex. Insertion of specific compounds into the channel pore, by site-directed mutagenesis, allows to influence the channel permeation to charged molecules (Levin and Blount, 2004; Yang et al., 2012).

For all the above reasons, there has been a boost in the design and development of new genetically modified variants of the MscL with distinct channel sensitivity (Yoshimura et al., 1999), conductance (Yang et al., 2012) and gating mechanism (Doerner et al., 2012; Kocer et al., 2005).

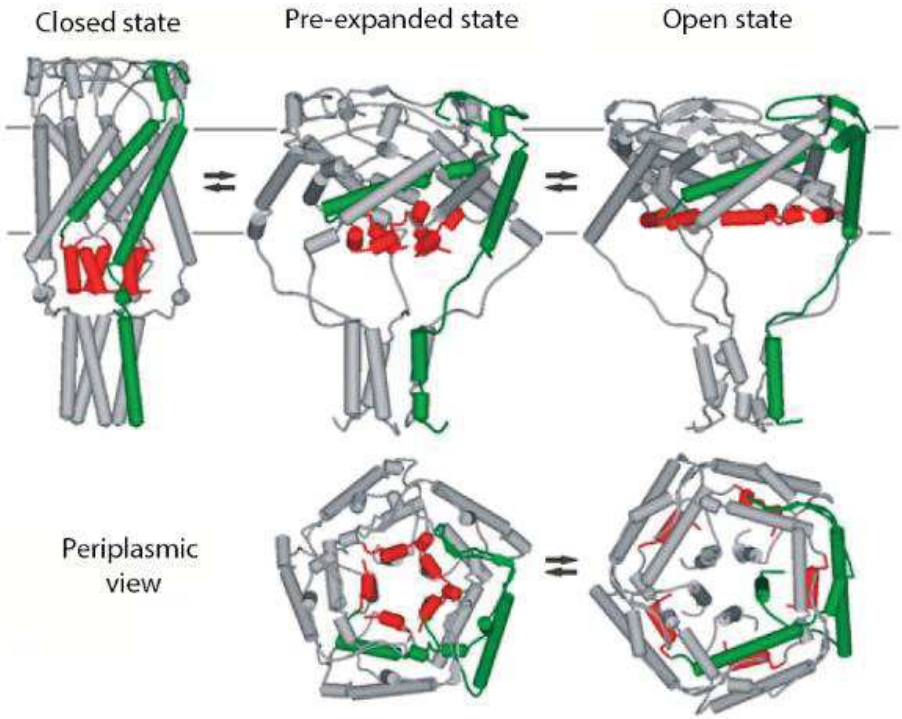


**Figure 6 | Changing in conformational structure of the MscL**

Cartoon of the movement of the MscL components upon stretching of lipid bilayer. For clarity, the N-terminal region of the channel is shown in red, and a single MscL subunit in green. The Sukharev-Guy (SG) model predicts that the N-terminal region plays the role of a "second gate", occluding the pore even when most of the expansion of the channel has already occurred (image extracted from Iscla et al., 2008).

In conclusion, MscL is the best characterized mechanosensitive channel, from any species, with a crystal structure and a detailed model of how the channel senses and responds to mechanical forces, and many mutated variants are already isolated and characterized (Iscla and Blount, 2012). Therefore, MscL represents the reference model for studying newly discovered mechanosensitive channels

and a tunable nanovalve for controlled delivery of membrane impermeable molecules (Bae et al., 2013; Cox et al., 2016).

## 1.4. Mechanosensitive ion channels in Eukaryotes

Although the mechanosensation is crucial for touch perception, proprioception, hearing and balance, blood pressure regulation, and many other physiological processes in living organism, the molecular characterization of mechanosensitive ion channels in eukaryotic cells proceeded much slower with respect to bacterial cells. Indeed, structural and functional studies of bacterial MS ion channels posed the bases for studying the mammalian ion channels.

Almost all eukaryotic MS channels have been recognized on the basis of the phenotype of mutant animals, as abnormalities of MS channel functions in neuronal development (Hong and Driscoll, 1994; Koser et al., 2016a), cardiac arrhythmias (Reed et al., 2014), hypertension (Köhler et al., 1999) and polycystic kidney disease (Köhler et al., 1999); or through the selective expression of proteins in mechanosensitive cells and *in-vitro* studies, rather than protein sequence homology.

However, the identification of mechano-transduction pathways in eukaryotic cells is still hindered by the genetic redundancy of some ion channels (Árnadóttir and Chalfie, 2010; Li et al., 2011).

In general, bacterial MS channels are gated by forces within the lipid bilayer transmitted by the interaction of the membrane lipids with the channel itself: the so called 'Force-from-lipids' concept (Cox et al., 2017; Teng et al., 2015). On the other hand, eukaryotic MS channels can also be gated by changes in the membrane tension (Maingret et al., 2000), and by the interaction of the plasma membrane with cytoskeletal proteins (Prager-Khoutorsky et al., 2014) or extracellular matrix (Akinlaja and Sachs, 1998; Poole et al., 2014), which is stretched accordingly to the tethering mechanism (Figure 7, (Lin and Corey, 2005)).

Such tethering mechanism has been identified in auditory hair cells in *Drosophila melanogaster* (Hudspeth and Jacobs, 1979) and in the touch receptor neurons in *Caenorhabditis elegans* (Chalfie and Au, 1989).

Several types of eukaryotic channels are mechanically gated. The transient receptor potential channels (TRP), the two-pore domain $K^+$ channels (K2p), TREK-1, TREK-2 and TRAAK, can be gated mechanically *in-vitro* (Maingret et al., 1999; Patel et al., 1998), but few evidences exist regarding their mechanical gating *in-vivo*.

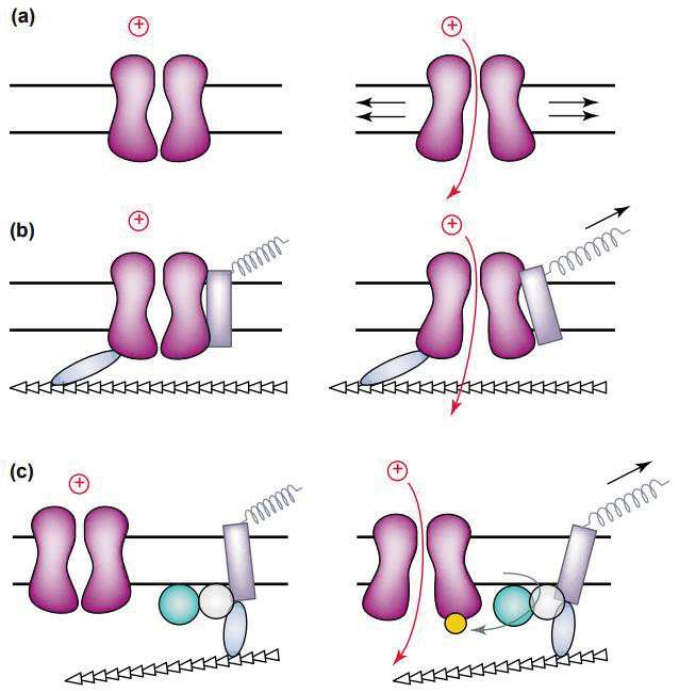


**Figure 7 | Gating mechanosensitive ion channels in Eukaryote**
Cartoon showing a mechanosensitive ion channel gated by (a) tension along the membrane, (b) the interaction with ECM or cytoskeletal protein through a tethering mechanism, and (c) upstream molecular pathways (image extracted from Lin and Corey, 2005).

Moreover, all these channels also open in response to other type of stimuli (Figure 8, (Honoré, 2007)) as membrane depolarization (Maingret et al., 2002), changes in cytosolic pH (Sandoz et al., 2009), heat (Kang et al., 2005) and polyunsaturated fatty acids as well as phospholipids (Lesage et al., 2000). Therefore, the sensitivity to the membrane stretch may represent only a way of modulating the response of these channels to other stimuli (Zheng, 2013).

Only recently, in eukaryotic cells have been identified an exclusively mechano-gated channel, which does not require any interaction with other cellular proteins: the Piezo family (Coste et al., 2012; Nourse and Pathak, 2017). Moreover, there are not evidences of accessory proteins tethering the Piezo channels to the cellular matrix, thus suggesting a mechanism of channel opening similar to the bacterial MscL (Lewis and Grandl, 2015).

In details, Piezo channels are expressed in a variety of tissues including DRG neurons, bladder, lung and colon, forming large pores that rapidly induce cation currents (Wu et al., 2017).

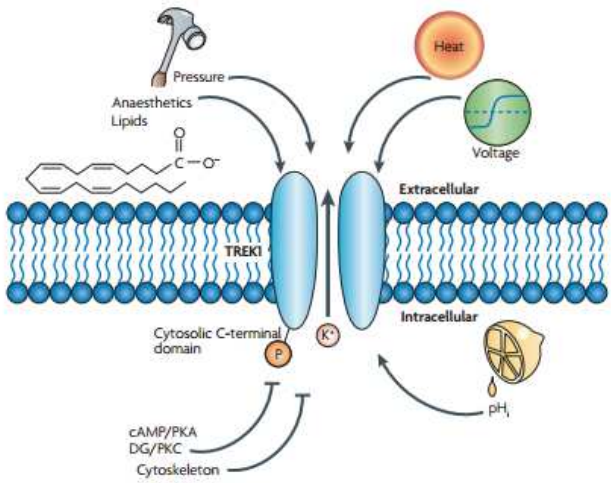


**Figure 8 | Polymodal activation of TREK1 ion channel**

The cartoon shows some physical and chemical stimuli including stretch, heat, pH, depolarization, and some phosphorylation pathways that may activate and inactivate the activity of most of eukaryotic mechanosensitive ion channels (image extracted from Honoré, 2007).

Piezo channels can be activated in a dose-dependent manner by mechanical stimuli, and unlike MscL channel, it presents a characteristic fast inactivation mechanism, that occurs after ~30 ms, and turns the channel in a non-conducting state, playing an important physiological function in the modulation of the channel activity. Additionally, the channel inactivation can be modulated by divalent ion concentration (Gottlieb et al., 2012), resting membrane tension (Lewis and Grandl, 2015), local changes in pH and transmembrane voltage (Bae et al., 2015), and alterations of channel inactivation kinetics is linked to several

human diseases, including dehydrated hereditary stomatocytosis (Albuisson et al., 2013), xerocytosis (Bae et al., 2013) and distal arthrogryposis (Coste et al., 2013).

## 1.5. Mechanobiology of the brain

In the recent years, there has been a growing evidence of the important contribution of physical parameters and tissue mechanics to the development of the central nervous system. During development, the cell systems undergo dramatic rearrangements, and many cellular processes as growth and motion on distinct length and time scales, rely on the generation and sensation of forces.

For example, during development, the mechanical properties of nervous tissue vary, and neurons are subjected to different mechanical cues during developmental stage (Gefen et al., 2003; Koser et al., 2016b), which in turn influences axonal navigation and cell migration as the well-established chemical cues (Elkin et al., 2007; Franze et al., 2011; Moore and Sheetz, 2011). However, also the adult nervous tissue is mechanically inhomogeneous (Franze et al., 2013), and its stiffness changes with age (Sack et al., 2009), thus suggesting that tensions along neuronal axons may be involved in neuronal network formation, stabilization (Anava et al., 2009; Franze et al., 2009) and folding of the brain (Figure 9).

Moreover, it has been shown that an axonal pretension of about 1 nN, it is necessary to establish functional neuronal connections *in-vivo* (Tofangchi et al., 2016).

The folding of the gyrencephalic mammalian cortex is the definitive mechanical consequence in the central nervous system development. In fact, the degree of cortical folding increases with brain size. Therefore, neurons in different layers maintain their sizes and network architecture while adapting their shape, while glial cells and blood vessels maintain size and shape and modify their relative

arrangements, in order to conserve the volume of the respective layers of gyri and sulci (Tallinen et al., 2016).

In this regard, the hypothesis of tangential expansion of cortical regions driven by the local cellular proliferation and changes in cell size and shapes is assumed to be the main factor involved in cerebral convolutional development (Richman et al., 1975; Ronan et al., 2014). On the other hand, another theory assumes that the tension along the axons in the white matter is the driving force inducing the formation of cortex folds (Essen, 1997). However, the two hypotheses are not mutually exclusive and both mechanisms could contribute together to shape the brain.

*In-vitro*, it has been shown that many neuronal cell types (e.g. dorsal root ganglion, hippocampal and some cortical neurons) adapt their viscoelastic properties, soma morphology (Hanein et al., 2011) and the dendritic arborization to the stiffness of the substrate (Georges et al., 2006; Norman and Aranda-Espinoza, 2010), and neuronal growth is likely a mechanical process. Indeed, it has been reported that cytoskeletal forces are required for neuronal network development (Anava et al., 2009; Lamoureux et al., 2002), as well as to regulate neuronal function as vesicle accumulation (Siechen et al., 2009), exocytosis and synaptic plasticity (Matus, 2000).

Although in physiological conditions, the overall central nervous system (CNS) is not subjected to external mechanical stresses, this tissue is highly susceptible to mechanical damage and strain resulting from trauma, and that the apparent stiffness of the brain strongly depends on the rate and extent of deformation as a complex viscoelastic material (Betz et al., 2011; Renema et al., 2007).

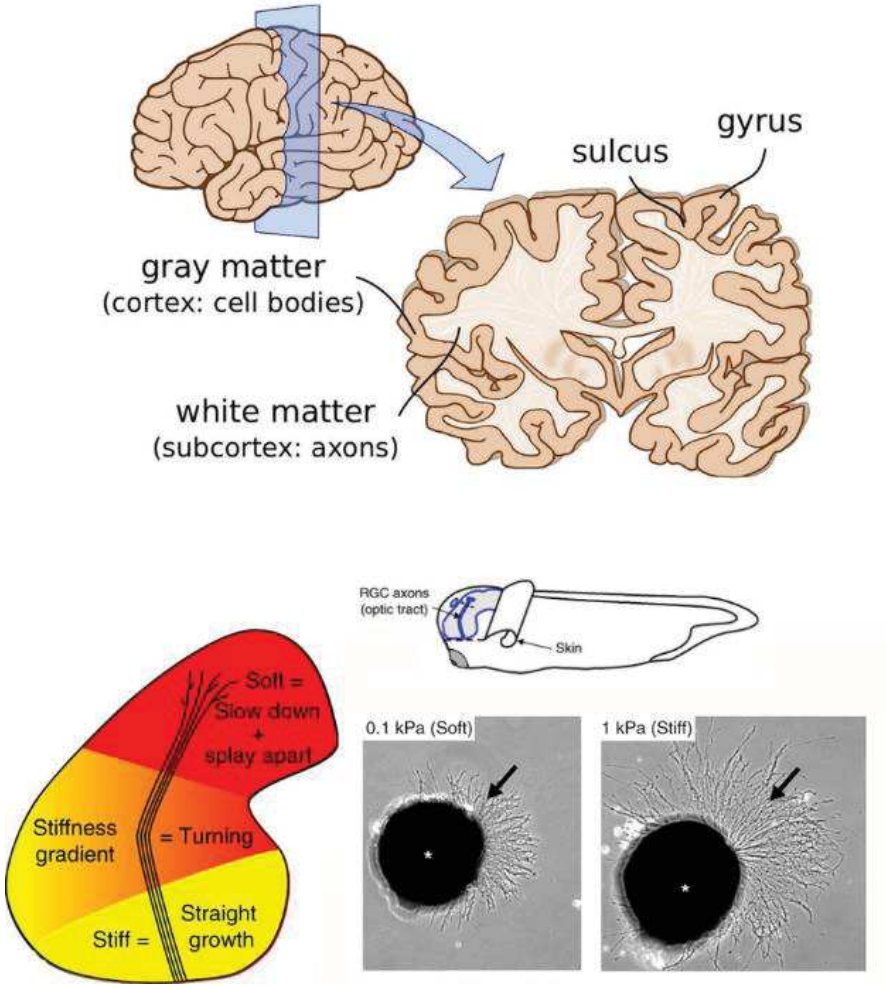


**Figure 9 | Mechanical signals contribute to neuronal growth in the development of the central nervous system**

Top panel: illustration of the macroscopic structures that can be identified in the human brain. Bottom panel: *Xenopus* retinal ganglion neurons (RGC) spread their axons in a faster, straighter, and more parallel manner on stiffer substrates. Moreover, a higher stiffness causes persistent growth and facilitates fasciculation. On the other hand, lower stiffness substrates promote slowed exploratory growth, playing beneficial role for those brain regions in which the axons have to search for their targets and form synapses. On the left of the panel is shown *Xenopus* retinal ganglion neurons spreading their axons on soft (0.1 kPa) and stiff (1 kPa) substrates (image extracted Koser et al., 2016b).

Therefore, the brain is modeled as a nonlinear viscoelastic material, which maintains a steady-state elastic modulus showing a significant degree of strain stiffening (Franze et al., 2013). The Young's, or elastic, modulus (E) describes the amount of force required to deform a substance in terms of units of force/area ($N \cdot m^{-2}$) or Pascals (Pa). This modulus can be quantified for each tissue and cell,

revealing their relative stiffness. The elastic properties of the brain have been measured through different technologies including magnetic resonance elastography (Riek et al., 2012), micrometer scale atomic force microscopy (Bernick et al., 2011; Christ et al., 2010) and other rheological measurements (Lee et al., 2011; Shulyakov et al., 2009).

Rodent and human brains present the smallest elastic modulus (Figure 10) with respect to other tissues types, which ranges from few Pascals to several gigaPascals (Barnes et al., 2017; Tyler, 2012).

In the last years, it has been reported that such elastic properties, of ultra-soft tissue, are important determinant of cell differentiation and proliferation (Jiang et al., 2015), morphology (Corey and Feldman, 2003) and function (Zhang et al., 2015). Furthermore, alteration of these mechanical properties or in the mechanosensing of neurons and glial cells have significant impact on patho-physiological state (Elkin, 2009; Iwashita et al., 2014; Murphy et al., 2011; Streitberger et al., 2012).

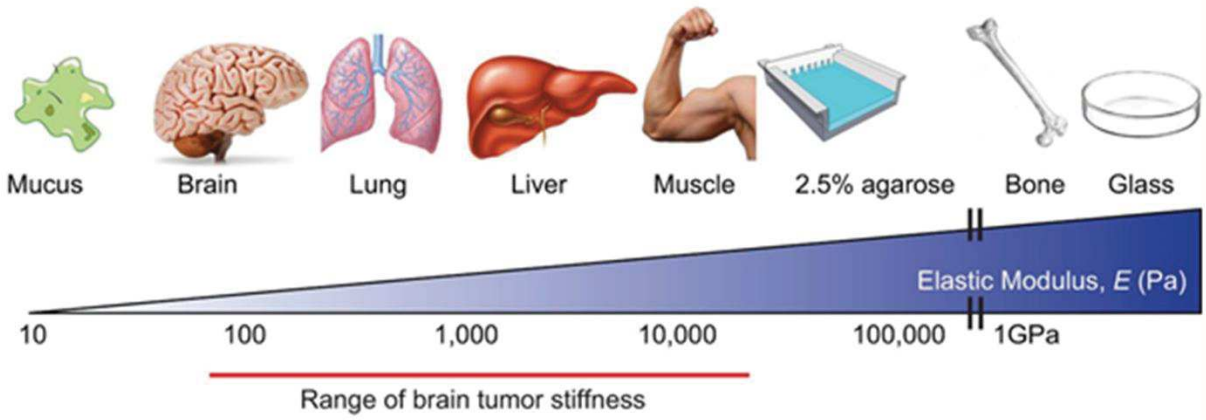


**Figure 10 | Mechanical properties of body tissues**

All tissues have distinct intrinsic physical properties, which are important in their structure and function. The stiffest tissues of the body are bones ($E \geq 10^9$ Pa), and the softest are lung and brain ($E \leq 10^2$ Pa). For reference, a tissue culture glass is in the order of gigaPascals (image extracted from Barnes et al., 2017).

Moreover, the viscoelastic properties of the brain are relevant to the development of minimally invasive surgical methods (Kaster et al., 2011) and insertion of neuro-prosthetic devices (Harris et al., 2011; Jorfi et al., 2015).

In neuronal cells, many cellular elements are involved in sensing and transducing the mechanical cues, including the mechanosensitive ion channels, the cell adhesion molecules (integrins, cadherins, proteins linking the cell adhesion sites to the cytoskeleton and focal adhesion kinases), the cytoskeleton and the nucleus itself (Figure 11, (Franze et al., 2013; Tyler, 2012)). Remarkably, the cytoskeleton has been proposed as an epigenetic determinant of cell shape, function and fate (Fletcher and Mullins, 2010). Neuronal cells contain an actin cortex and densely packed polarized bundles of microtubules and neurofilaments, a type of intermediate filament (Mukhopadhyay et al., 2004). The nucleus is mechanically connected to the cell plasma membrane through the cytoskeleton (Maniotis et al., 1997; Wang et al., 2009), which transmits and generates mechanical forces (Brangwynne et al., 2006b).

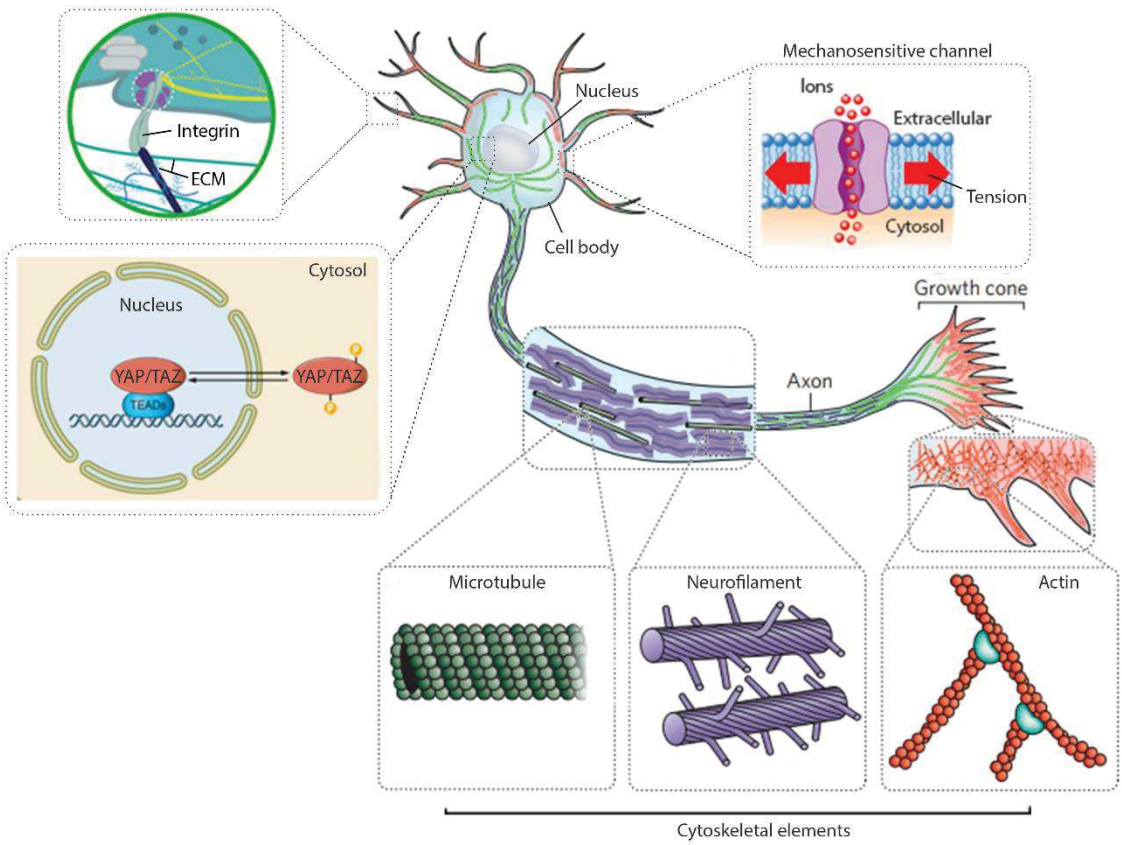


**Figure 11 | Mechanical forces are generated and transduced in neurons**
The cell body of a neuron, showing cellular and molecular components that transduce or sense micromechanical forces (image extracted and modified from Fletcher and Mullins, 2010).

For example, the F-actin network together with myosin motors supports neurite pre-tension, generates contractile forces within the navigating growth cone (Betz et al., 2011) as well as on the nuclear membrane and the internal nuclear scaffolding (Mazumder et al., 2008). In summary, many cellular pathways in the nervous system seem to be controlled by mechanics, and that mechanical and chemical cues work in synergy to activate signaling pathways (Zhang and Labouesse, 2012), functional outcomes of the brain tissue.

# CHAPTER TWO: Interfacing the nervous system

## 1.6. State-of-the-art in neuromodulation

The central nervous system constantly collects sensory information generated by external the stimuli, and process them in order to actuate decisional tasks and actions, which are thus influenced from previous experiences. Therefore, understanding how neuronal circuits process these information, and how the external stimuli can modulate the computation of the neuronal network represents a critical task to link the sensation of the environmental stimuli with the behavioral outcome of the living organisms.

In this regard, neuronal stimulation techniques are essential tools to perform modulation of the neuronal network activity (neuromodulation), and thus investigate the causality between external stimuli, network electrophysiology, and physiological and behavioral responses (Panzeri et al., 2017). Moreover, dissecting the neuro-computation of brain circuits constitutes the primary knowledge to develop neuroprosthetic devices and/or identify effective strategies to treat neurological disorders, and allow the design of alternative and more effective strategies to treat neurological disorders.

Usually, the simulation of external environmental stimuli is accomplished through the direct alteration of the neuronal activity in the form of electrical or chemical signals (Figure 12).

However, other approaches are currently in use to manipulate the activity of brain circuits, and starting from the classical chemical and electrical interfacing (Cohen and Newsome, 2004), other methods as the optical (Wells et al., 2005) and more recent magnetic (Tay and Di Carlo, 2017; Wheeler et al., 2016) and ultrasonic stimulation technologies are undergoing a consolidation phase to go beyond the research development, and thus targeting the clinical scenario (Tufail et al., 2010).

Each stimulation strategy presents advantages and disadvantages with respect to clinical use and field of application, degree of invasiveness, penetration depth of target region, cell type specificity or spatial resolution, and technological/clinical maturity.

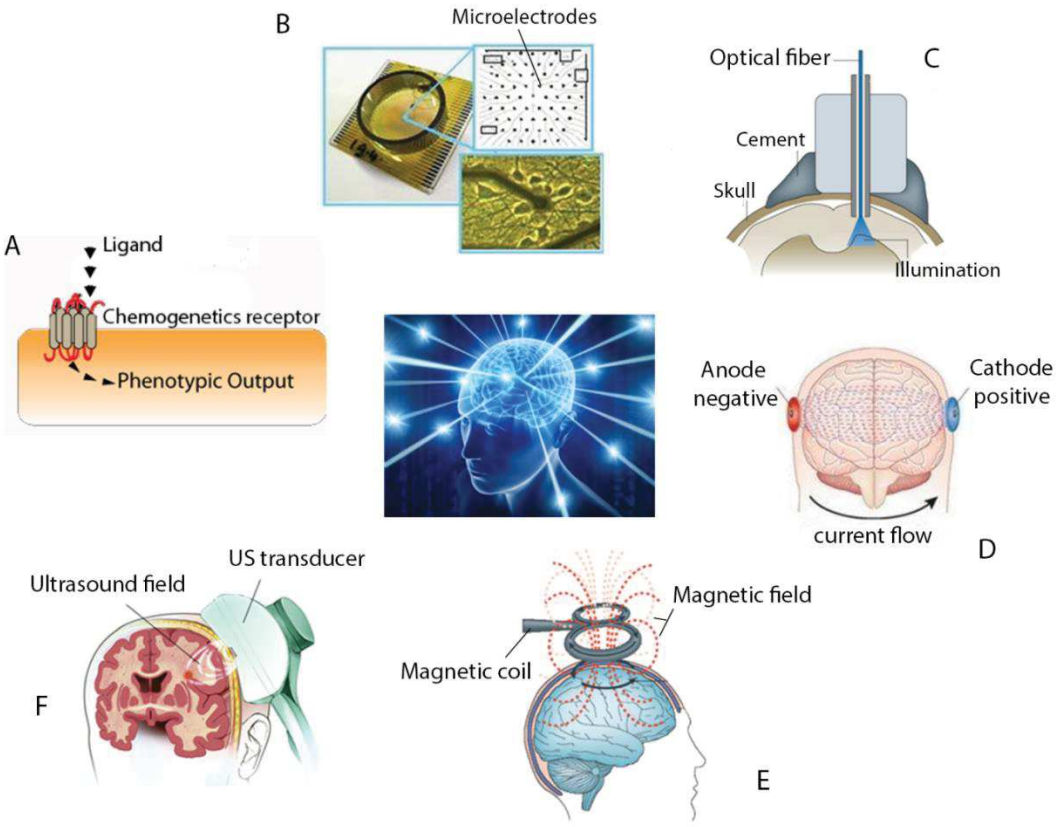


**Figure 12 | State of the art of neuromodulation technologies**

A) Chemogenetics receptor constructs are injected into selected brain areas through gene therapy approaches. These receptors are engineered in order to do response exclusive designed drugs that have no effect on organisms native receptors.

B) Multi Channel Systems MEA is shown. The inset shows a magnified planar image of the array of electrodes and further electron microscopic image showing a single electrode and its interaction with surrounding neurons.
C) Optogenetics approach is shown. In the image and optical fiber is implanted and inserted through the bone skull for illuminating the subcortical area of the brain.
D) A transcranial direct current stimulation device is used to apply a small amount of electrical current to the scalp via two electrodes; a positive "anode," and negative "cathode".
E) The transcranial magnetic stimulation is achieved through the application of a magnetic coil in order to create a steady electromagnetic pulse above the scalp. Currently transcranial magnetic stimulation is the most commonly practiced brain stimulation technique in the medical field.
F) Transcranial ultrasound waves are applied through the scalp overlying the frontal temporal cortex.

Nowadays, the state of art of electrical and/or optical stimulation is paving the way for the development of neuro-prosthetic systems operating at single cell resolution, and with an high temporal bandwidth either working in open or close loop configuration (Cash and Hochberg, 2015).

In particular, the advent of optogenetics, with the concomitant breakthrough of optical technologies, allows to modulate the firing patterns of neuronal network by providing both cell type-specific expression of light-sensitive ion channels (Beltramo et al., 2013), and subcellular targeting of the light focus spot on single neuronal units. Furthermore, a concomitant use of synthetic or genetically encoded fluorescent sensors allows the simultaneous readout of neuronal network activity at incomparable spatial resolution, in order to achieve an all optical interfacing of the brain tissue.

For all the above reasons, optical approaches and optogenetics represent the most effective strategies for dissecting the physiology of neuronal circuits in the neuroscience research.

However, optogenetics presents several challenges to achieve its effective clinical translation, because it requires the insertion of stimulation probes to achieve deep region of the brain, as in electrical stimulation methods, which could induce severe side effects (i.e. glial scar formation, inflammation, and deterioration of the implanted probes (Grill et al., 2009)).

Another recent technology relying on the genetic manipulation of tissues and cells, which does not require the implantation of devices, it is the so called chemogenetics. Chemogenetics, also known as designer receptors exclusively activated by designer drugs (DREADDs) technology (Armbruster et al., 2007), is currently employed in many studies of behavioral neuroscience. This technology exploits the cell specific expression of molecularly modified muscarinic G protein-coupled receptors (GPCRs) for controlling a defined subset of neuron cells in order to activate or silence neuronal firing. When compared with optogenetics, DREADDs shows a lower temporal resolution in controlling the neuronal activity, and for this reason it is suited for modulation of cell activity in the range of minutes–hours depending on the pharmacokinetic properties of the synthetic agonist employed. However, also in this case the translation of the approach to the clinic, it isn't yet safely achievable because of the use of viral vectors, for inducing the targeted expression of engineered ion channels, could generate critical immune responses.

The ideal stimulation technology should avoid implantation of probes, and favor wireless remote-modulation of neuronal circuits activity. Moreover, it should be safe under long-term exposure, and provides high spatial-temporal control of the stimulus (Tay et al., 2016).

Today, the alternative approaches to bypass surgeries associated with the implantation of devices include transcranial electrical, thermal, magnetic, and ultrasound stimulation (Fregni and Pascual-Leone, 2007). Transcranial electrical stimulation suffers poor spatial resolution, and it has a pure modulatory effect on the network activity (Grossman et al., 2017). Thermal stimulation of temperature-sensitive ion channels demand the use of functional nanoparticles to obtain spatially localized stimulation, as the heat fast diffuses in the neighboring tissue (Wang and Guo, 2016). On the other hand, magnetic and ultrasound (US) fields could deeply propagate in dense tissues through the intact skull bone, and they could be focused in small focal volumes (Tyler et al., 2008). In the first case, the

weak interaction of magnetic fields with biological molecules provides safety and low-invasiveness, but it demands the use of targeted magnetic nanoparticles, in order to locally transduce magnetic-to-mechanical forces, and thus accomplish selective cell stimulation (Hughes et al., 2008). In the latter case, US fields guarantee deeper penetration and sharper spatial focus in dense tissues, and US generators could be easily miniaturized (Li et al., 2009). Moreover, low-intensity US pressure fields can stimulate *per se* untreated neuronal cells and tissues, and the targeted delivery of micro- (Carugo et al., 2017a) and nano-particles (Marino et al., 2015) is otherwise exploited to increase its stimulation efficiency and spatial selectivity. Therefore, the use of US pressure field is attracting much attention, as it has the potential for the development of portable implantation-free stimulation devices.

Nowadays, US waves are already widely employed in the clinical environment for imaging, rehabilitation physiotherapy, thrombolysis, and targeted tumor ablation protocols. Such applications rely on well-defined physical processes, leading to reliable and tunable results. In contrast, the application of low-intensity US fields is still in its infancy due to the lack of a clear biophysical explanation of the involved phenomenon. A similar debate has been raised regarding the use of magnetic field, as a unifying theoretical and experimental framework is missing (Meister, 2016).

Nowadays, it is becoming more clear that the mechanism behind the US-induced neuromodulation is pressure-dependent, however a clear identification of the generated local pressures with respect to the delivered US intensities is still missing (Younan et al., 2013).

The emerging field of mechanobiology has led to the discovery, and subsequent engineering and exploitation of cellular mechanical transduction pathways, as shown into recent studies (Ibsen et al., 2015; Wheeler et al., 2016) which report the use of mechanosensitive ion channels for triggering a cellular response by either magnetic or low-intensity ultrasound fields (Figure 13A).

The extraordinary achievements of these studies establish the foundation of two new research areas called magnetogenetics and sonogenetics in addition to the well-established optogenetic approach.

However, the use of channels, such as TRPV, with intrinsic sensitivity to several other endogenous stimuli including voltage, heat, pH, etc., has not yet been fully evaluated. Indeed, as suggested by the authors of the aforementioned study (Wheeler et al., 2016), the overexpression of non-exclusively MS ion channels may compromise the physiology of the neuronal circuits, thus further molecular engineering of such tools is required in order to render them non-responsive to other stimuli.

An alternative route to achieve stimulus specific sensitization of tissues and cells is represented by the emerging field of nanotechnology (Figure 13B). Smart nanoparticles are designed and developed to obtain local enhancement of the stimulating field, or local transduction of the penetrating signal to a biological one, leading to a modulation of the cellular activities (Rivnay et al., 2017).

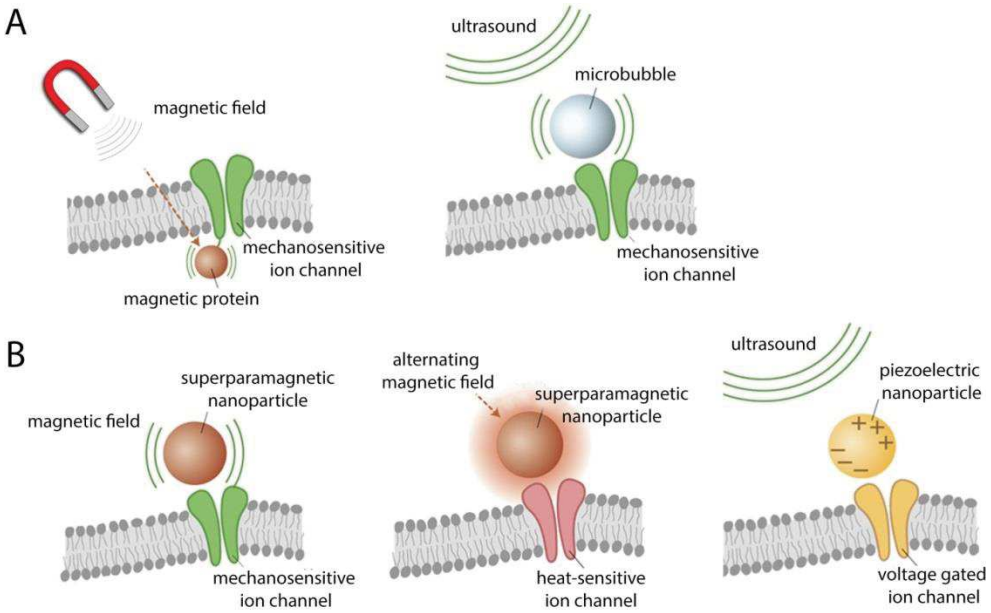


**Figure 13 | Next generation of neurostimulation actuators**

A) Magnetogenetics and sonogenetics approach combine magnetic proteins or air filled microbubbles, respectively, for stimulating mechanosensitive ion channels.

B) The mechanical stimulation of the cells may be achieved through the combination of superparamagnetic nanoparticles (left) or magnetic proteins acting on a heat-sensitive channel

(middle) with magnetic fields. Alternatively, the ultrasound stimulation through piezoelectric nanoparticles may be used for modulating voltage gated ion channels (extracted from Rivnay et al., 2017).

Nanoparticles are engineered accordingly with biological molecules to target specific cellular component or tissue portions, to avoid toxicity, or to bypass biological barrier as the blood brain barrier. In this regard, prominent examples are represented by the use of gold nanoparticles to perform both thermal cell stimulation (Marino et al., 2017) or ablation, and the use of barium titanate piezoelectric nanoparticles (Marino et al., 2015) to locally transduce ultrasound field in electric potential stimulating cellular growth and development.

In conclusion, taking into account the several advantages and drawbacks of each approach, it is worth to note how novel methods take inspiration from the previously developed, and how distinct combination of core technologies such as genetic engineering, nanotechnology, and DNA origami to design ion channels, is becoming a common practice to overcome the current limitation of cell stimulation technologies.

## 1.7. Ultrasound stimulation of neuronal circuits

Nowadays, ultrasound waves are already exploited in many clinical applications from imaging to rehabilitation physiotherapy and targeted tumor ablation (Figure 14, (Tyler et al., 2010)). The range of US frequencies goes from tens of kHz to tens of MHz.

The main advantage of US waves is that they penetrate several centimeters of soft and hard tissue with low attenuation, and moreover, they can be focused from outside the human skull to a tight focal stimulation volume (in the range of $mm^3$) in the brain. In this context, while higher frequency ultrasound provides better spatial resolution, lower frequency ultrasound enables deeper brain penetration (10 - 15 cm or more) and therefore they are more effective for brain neuromodulation (Tufail et al., 2011).

The effects of the ultrasound waves can be divided into thermal and non-thermal ones, accordingly to the applied US frequency and intensity, and the corresponding acoustic pressures (Rezayat and Toostani, 2016).

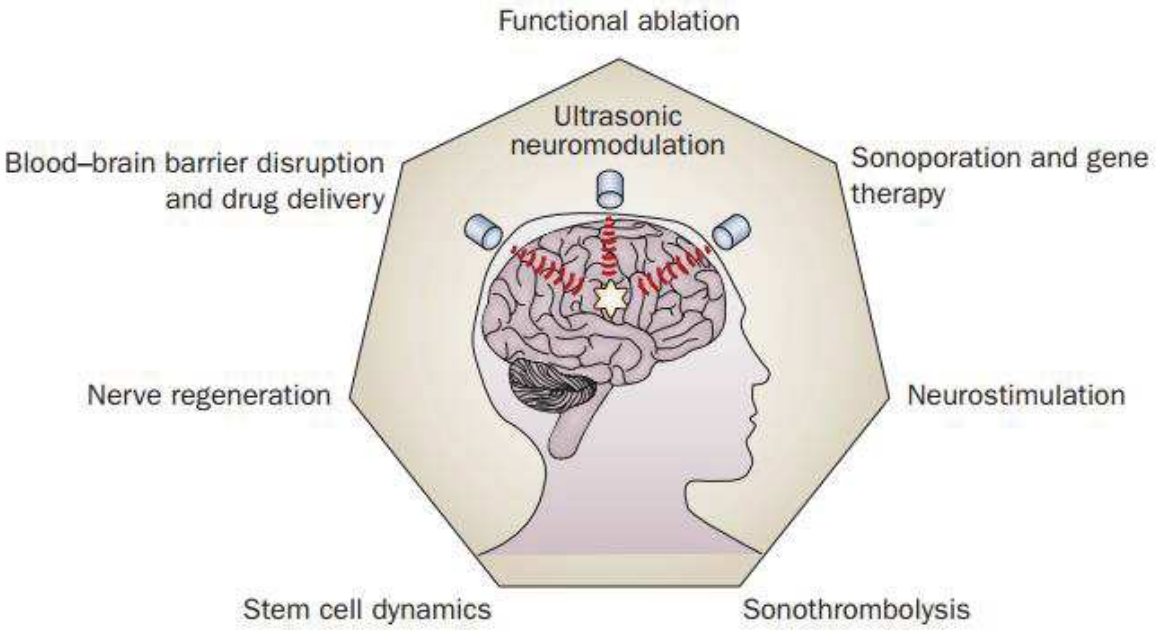


**Figure 14 | Potential applications of ultrasonic neuromodulation**
Through both thermal and non-thermal (mechanical) mechanisms, ultrasound has been shown to exert numerous bioeffects on brain tissues that could provide a basis for noninvasive therapies for neurological and psychiatric disorders (extracted from Tyler et al., 2010).

There are several units for measuring the ultrasound intensity, as example, it may be measured as function of the acoustic pressure amplitude or as function of the spatial peak–temporal average intensity, where the latter represents the highest intensity measured at any point in the ultrasound beam averaged over the pulse repetition period (Nelson et al., 2009).

Three main regimes of pressure amplitude: i) low pressure, for delicate and reversible alterations in cells and tissues with pressure amplitudes on the order of 0.1 MPa ($I_{spta}$ equal to ~ 0.3 W·cm$^{-2}$ for a propagating wave); ii) medium pressure, for imaging with pressure amplitudes up to about 5 MPa (~ 10 W·cm$^{-2}$); and iii) high intensity focused US with acoustic pressures reaching about 10 MPa (~ 1000 W·cm$^{-2}$) at the focal zone (Bailey et al., 2003).

In the latter case, USs usually induce local heat (up to 70°C in 1 - 3 seconds, (Bailey et al., 2003)), formation of gas microbubbles (cavitation), lesioning and ablating local tissues (Carstensen et al., 2000). On the other side, low-intensity US fields have also been shown to be capable of inducing bio-effects in cells and tissues with no evidences of cavitation or temperature rise being present (Dalecki, 2004; O'Brien Jr., 2007), demonstrating great potential for safe biomedical applications (Rezayat and Toostani, 2016).

It is worth noting that ultrasound stimulation of neuronal circuits has already been demonstrated by several studies (Table 1), including in brain slice (Tyler et al., 2008), in retina (Menz et al., 2013), *in-vivo* in mice (Tufail et al., 2010) and even in humans (Legon et al., 2014).

A prominent example of low-intensity US application (as low as 0.05 $W \cdot cm^{-2}$ at 2 MHz of US frequency), it is the use of focused ultrasound for the modulation of neuronal activity. Tyler and colleagues demonstrated that focused ultrasonic energy pulses could be used for the stimulation of neural structures within the mammalian brain both *in-vitro* and *in-vivo* through the intact skull bone (Tufail et al., 2010; Tyler et al., 2008; Yoo et al., 2011). In the last few years, similar modulatory effects have been reported by other research groups in different brain areas (Li et al., 2016; Ye et al., 2016a). However, although the safety of using US waves has been well-established for some clinical applications as biomedical imaging, rehabilitation physiotherapy, thrombolysis, and tumor ablation, the principle behind the use of US for stimulating cellular activities, it is still not well understood.

Recent progresses in technology have also allowed the miniaturization of the US sources, attracting more attention for the development of portable devices, which would present the potential for noninvasive applications in neuromodulation research (Li et al., 2009).

Moreover, in the noninvasive therapeutic application of ultrasounds, the use of ultrasound-responsive agents, in the form of hard-shell and soft-shell

microbubbles, is also exploited (Carugo et al., 2017b; Kiessling et al., 2012; Scarcelli et al., 2014), and clinically approved (Paefgen et al., 2015), in order to target specific tissues, and to locally amplify the US-cells interaction, thus enhancing the stimulation efficiency and the spatial selectivity.

| Publication | Ultrasound parameters | |
|---|---|---|
| **(Legon et al., 2014)** | Organism: humans<br>Frequency: 500 kHz<br>Duration: 0.5 s | PRF: 1 kHz<br>TBD: 0.36 ms<br>Energy: 8.6 $W \cdot cm^{-2}$ |
| **(Kim et al., 2014)** | Organism: rats<br>Frequency: 350 - 650 kHz<br>Duration: 40 min<br>PRF: Variable | TBD: 1- 5 ms<br>Stimulus duration: 300 ms<br>Energy: 2.5 - 2.8 $W \cdot cm^{-2}$ |
| **(Deffieux et al., 2013)** | Organism: monkeys<br>Frequency: 320 kHz<br>Pulse duration = 100 ms | Single pulse<br>Energy: ≈ 0.023.3 $W \cdot cm^{-2}$ |
| **(Choi et al., 2013)** | Organism: rats<br>Frequency: 500 kHz<br>Duration: 55 s over 5 min | PRF: 10 – 100 Hz<br>TBD: 20 μs<br>Energy: 0.016 – 0.093 $W \cdot cm^{-2}$ |
| **(Tufail et al., 2010)** | Organism: mice<br>Frequency: 25 - 50 kHz<br>Duration: 40 cycles/pulse<br>at 2 kHz for 650 pulses | Energy: 0.036 – 0.084 $W \cdot cm^{-2}$ |
| **(Tyler et al., 2008)** | Organism: mice<br>Frequency: 44 - 66 kHz<br>TBD: 22.7 ms | Cycles/tone: 10<br>Pulse repetition: 0 – 100 Hz<br>Energy: 0.023 $W \cdot cm^{-2}$ |
| **Legend**<br>PRF: pulse repetition frequency TBD: tone burst duration<br>Energy reported as function of the spatial peak - temporal average intensity | | |

**Table 1 | Summary of recent ultrasound parameters employed**

The soft-shell microbubbles are gas-filled bubble, having a size as low as 3 - 4 μm, and the shell largely made of phospholipids (Ferrara et al., 2007). Due to the presence of a compressible core and a thinner and flexible shell, the lipid-coated microbubbles can respond, accordingly to their resonance frequency and size, to a specific ultrasound frequency, and this phenomena is known as cavitation.

Accordingly to the US intensity, the cavitation can be divided in two different types: (i) stable cavitation, occurring when low-intensity ultrasounds are used and (ii) inertial cavitation, occurring at higher ultrasounds intensities (Lentacker et al., 2014).

When the inertial cavitation is too strong, the microbubble may collapse on itself, fragmenting into many smaller microbubbles. Such fragmentation creates a much more strong mechanical perturbation than the one occurring in stable cavitation, and it may lead to perforation of the cell membrane as previously reported in literature (Postema et al., 2004). On the other hand, at very low acoustic pressures, microbubbles likely go toward an volume oscillatory behavior, alternating expansion/compression phases in an inversely proportional manner to the local ultrasound pressure (Sboros, 2008). When such oscillation occurs nearby cell membranes, cells experience the generated mild mechanical perturbations of the surrounding environment, in terms of shear stress (Vanbavel, 2007), microstreaming (Wu et al., 2002) and radiation forces on the cell membrane (Fan et al., 2013), which may potentially trigger the activation of many biological pathways (Wu and Nyborg, 2008).

Recently, in order to decrease the level of invasiveness of such micro-scaled tools, ultrasound-contrast agents in the form of genetically encoded nanostructures (Shapiro et al., 2014) or phase-shift protein-polymer nanodroplets (Lee et al., 2015) have also been designed and successfully applied to improve ultrasound imaging performance.

As already mentioned early in the chapter, the interaction of ultrasound alone and the ultrasound coupled with contrast agents may induce nonthermal effect (mechanical one) and thermal effects, depending on the ultrasound intensity, exposure and tissue properties (Miller et al., 2012). It is worth noting that any temperature rise could change the biophysical properties of the cell membranes and could make them more susceptible to membrane deformation, thus eliciting unwanted cellular responses (Bioeffects Committee, 2008). However, in the range

of diagnostic ultrasound, temperature rises and triggering of potential adverse bioeffects are kept relatively low or negligible (Johns, 2002). This evidence has also been confirmed when ultrasounds are employed for eliciting neuronal responses through the use of transcranial pulsed low-intensity and low-frequency ultrasounds (US frequency: 25 – 50 kHz, energy: 0.026 – 0.160 $W \cdot cm^{-2}$ (Tufail et al., 2010)). Several models for low-intensity US-mediated bioeffects have been proposed (Sassaroli and Vykhodtseva, 2016), including those based on intramembrane cavitation (Krasovitski et al., 2011; Plaksin et al., 2016), and modulation of mechanosensitive ion channels (Tyler, 2011). In the latter case, the hypothesis is that US waves convey a pressure signal which could generate a mechanical perturbation of the cells, and thus activate cellular mechanotransduction pathways. Indeed, it is becoming more evident that all cells have some intrinsic mechanism of mechanosensation, and that the brain itself is a highly mechanosensitive organ (Tyler, 2012).

In this regards, the pressure field generated by the low-intensity US may modulate neuronal excitability by changing the viscoelastic properties of the neuronal lipid bilayers (Johns, 2002) and/or induce the gating of mechanosensitive membrane proteins (Tyler et al., 2008).

It is worth noting that direct experimental evidence of US pressure waves affecting the activity of mechanosensitive ion channels has been provided only recently (Kubanek et al., 2016), thus corroborating the hypothesis that low-intensity US can potentially modulate cellular mechanotransduction pathways (Hertzberg et al., 2010). Recent studies also suggested that the mechanisms of excitation involve voltage-gated sodium and calcium channels eliciting synaptic transmission, however, the question of how low-intensity ultrasound waves with millimeter wavelength transduce these nano-scale perturbations is unanswered yet (Kubanek et al., 2016).

One of the first experimental demonstration of the so called sonogenetic approach, in analogy to the optogenetic method, has been carried out in *C.*

*Elegans* model, through the mechano-sensitization of the animal by overexpressing the mechanosensitive ion channel TRP4. The genetically modified animals, navigating in presence of sparse air-filled microbubbles, showed a behavioral response to low-intensity US stimuli in 40% of the cases (Ibsen et al., 2015). However, a parallel study presenting the design of an ultrasound neuromodulation chip delivering surface confined acoustic energy to perform US stimulation on wild type *C. Elegans* model reported a proportion of 85% of responsive animals (Zhou et al., 2017).

The results of these two independent studies, carried out using the same type of organism, external stimuli, and behavioral tests, indicate that both the genetic engineering and manipulation of living organism, and/or the accurate design of US delivery systems may allow achieving efficient low-intensity US stimulation strategy on living organism.

However, further understanding of the mechanosensitive pathways involved in US-mediated cell activation needs to be fully confirmed in order to reliably perform remote tissue modulation.

# AIM OF THE PROJECT

Development of remote stimulation techniques of neuronal tissues represents a challenging goal. They would allow the combination of functional and behavioral studies, and development of novel and minimally invasive prosthetic approaches. Among the potential approaches to achieve remote non-invasive stimulation, the ones exploiting mechanical stimuli are the most promising, because mechanical signals can convey information into intact brain tissue. In this regards, the selective mechano-sensitization of neuronal circuits would pave the way for the development of a novel cell-type specific stimulation approach.

In this dissertation, we report the use of the exclusively-mechanosensitive bacterial ion channel MscL to obtain an experimental model of mechano-sensitized mammalian neuronal networks, which could be used to study and understand the mechanism of US cell stimulation, and thus pave the way for the engineering and development of a cell-type specific ultrasonic neuromodulation approach.

The cDNA sequence encoding for bacterial MscL channel was optimized for the mammalian neuronal expression and trafficking to the plasma membrane through the use of a neuron-specific promoter, and a membrane targeting motif. Additionally, we tested and validated that the expression of the engineered MscL construct (eMscL) does not affect the functionality and the physiological development of neuronal networks in terms of morphology, synapse formation

or excitability, and network activity, while providing an efficient mechano-sensitization of the neuronal cells.

Moreover, we report the design, and the accurate calibration of a prototyped ultrasound delivery system integrated with a custom-built fluorescence microscope, to perform high-throughput studies of the effects of US stimulation on *in-vitro* neuronal with single cell resolution. The optical system has been designed to perform functional calcium imaging of neuronal networks, and thus to simultaneously monitor the activity of hundreds of neurons through an automated analysis algorithm. The US generator has been equipped with a US transmission element to deliver a relatively uniform pressure field at a pre-defined distance from the ultrasound source (without the need for a water tank apparatus), thus facilitating its integration with fluorescence imaging in a sterile and physiological conditions for the cells during US stimulation.

Overall, our data demonstrate the successful development of a mechano-sensitized neuronal network model to allow reliable investigation, and testing the stimulation of excitable circuits through the use of mechanical energy remotely-generated by US generating devices. Moreover, considering the ease engineering of MscL channel properties, through the genetic modification of its well-known sequence and function and more worth its exclusively mechanosensitivity, we believe that the mammalian-engineered MscL may represent the ideal starting point to develop a mechanogenetic approach analogous to the optogenetic method.

## 2. Membrane targeting of the MscL ion channel in primary neuronal cultures

In the present work, we have established an experimental model to advance and leverage many aspects of the sonogenetic approach. Initially, we designed an exclusively-mechanosensitive molecular tool for sonogenetic applications, analogous to the sensing elements giving specific sensitivity in the well-established opto- and chemogenetic techniques. In particular, we designed a mammalian expression vector encoding for the bacterial Eco-MscL ion channel fused to tdTomato fluorescent protein under the control of the neuronal-specific synapsin 1 promoter (MscL-v.1 in Figure 15). However, a first functional assessment of MscL-tdTomato expression in primary neuronal cells revealed a significant impairment in the delivery of the heterologous protein to the plasma membrane. In fact, transfected neurons showed large intracellular accumulation and clustering of MscL-tdTomato that consequently resulted in low membrane expression (Figure 16A, left column panels). We reasoned that the accumulation and clustering of MscL could likely depend on the lack of a mammalian-specific export signal that prevents protein retention in the endoplasmic reticulum (Li et al., 2000). Following previous studies that optimized the mammalian expression of optogenetic actuators (Gradinaru et al., 2008), we fused the export signal of

Kir2.1 ion channel (MscL-v.2 in Figure 15) to cytoplasmic C-terminus of our MscL-tdTomato protein.

The Kir2.1 ER export sequence (FCYENEV) has been extensively studied, and it is known to mediate efficient trafficking and surface expression of the channel (Hofherr et al., 2005; Stockklausner et al., 2001).

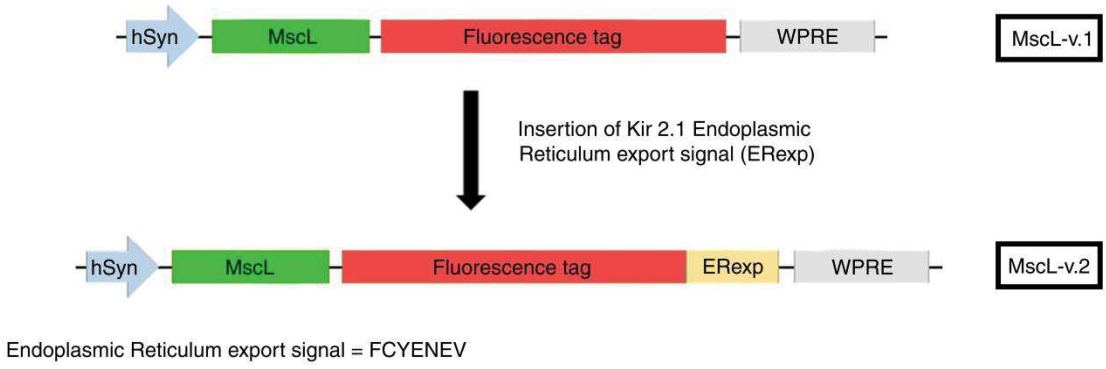


**Figure 15 | Molecular engineering of the MscL ion channel**

Construct map of the MscL-v.1 (top) and MscL-v.2 (bottom) plasmid in adeno-associated viral vectors. MscL-v.2 is optimized for expression in mammalian primary neurons.

Moreover, Kir channel monomers present structural similarities (e.g. two transmembrane domains, cytoplasmic N- and C-terminals) with MscL monomers, likely suggesting a similar pathway in protein trafficking. In order to assess the membrane localization of naïve MscL (MscL-v1) versus MscL-v.2 bearing the ER export signal, we co-transfected primary neuronal cell cultures with two plasmids: the tdTomato-tagged MscL (either MscL-v.1 or MscL-v.2) and a membrane-targeted myristoylated GFP (myr-GFP). Confocal microscopy examination confirmed enhanced localization of the MscL-v.2 channel along the neuronal membrane (Figure 16A, right column panels), presumably due to prevention of ER retention and aggregation. In fact, a representative fluorescence intensity profile (along a cross-section line from the center of the cell soma to the plasma membrane, Figure 16B, top panel) of tdTomato-tagged MscL-v.1 (red line), together with the membrane-targeted GFP (green line), shows prominent intracellular localization of MscL-v.1, resulting in the absence of fluorescent co-

localization with myr-GFP at the plasma membrane of the cell (vertical dashed lines). Conversely, tdTomato-tagged MscL-v.2 fluorescence largely co-localized with myr-GFP (Figure 16B, bottom panel), indicating efficient plasma membrane delivery of the channel.

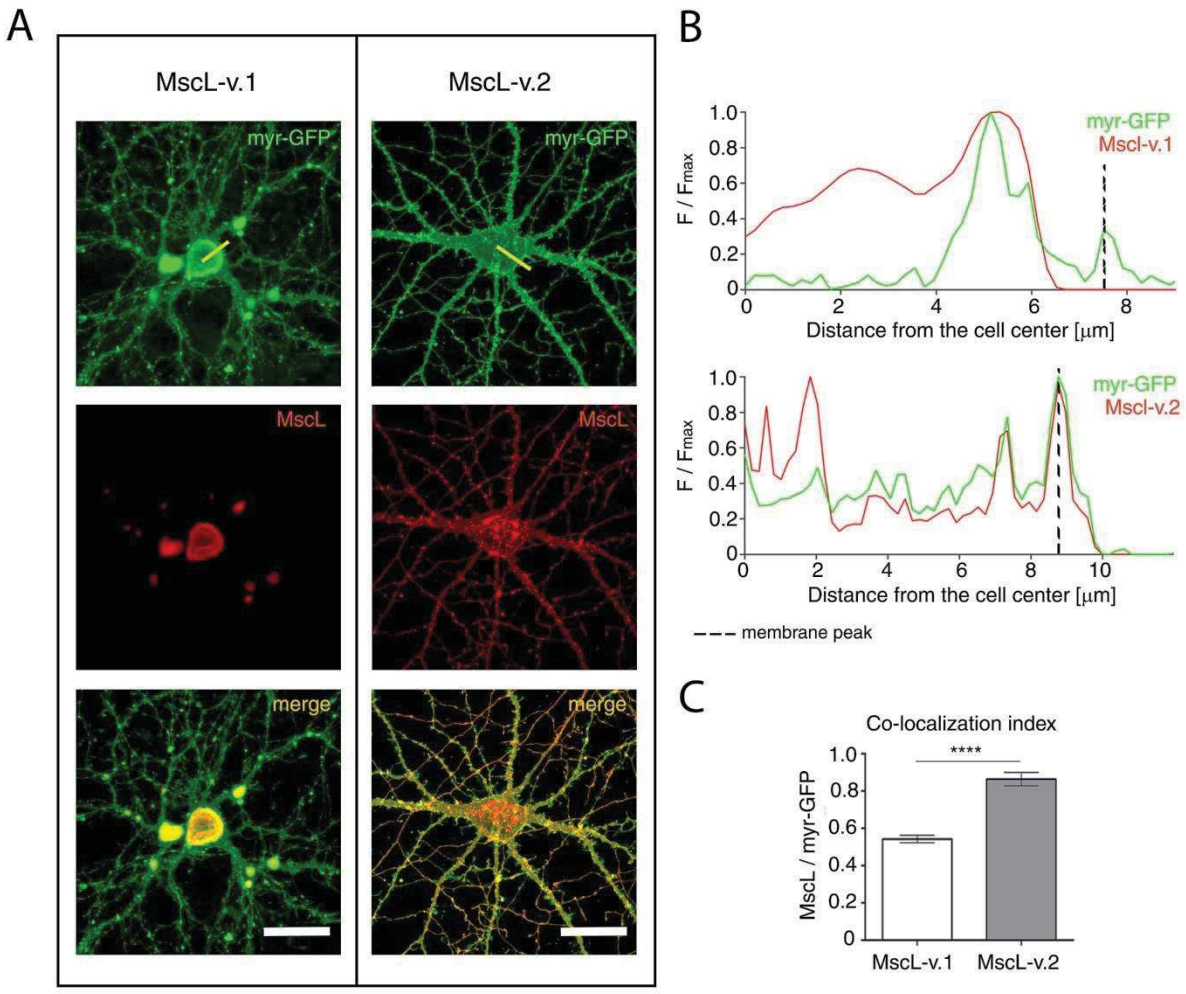


**Figure 16 | Membrane targeting of the MscL-v.2 ion channel**

A. Cortical primary neurons expressing the MscL-v.1 (left) and MscL-v.2 (right) constructs. Myristoylated GFP (green) and MscL fused to tdTomato (red), and their fluorescence signal merged (yellow) are shown to illustrate the reduced aggregation of MscL in ER (endoplasmic reticulum), as well as its improved membrane expression after addition of the Kir2.1 ER export signal. Scale bar= 50 μm.

B. Normalized fluorescence intensity profile of the myr-GFP with either the MscL-v.1 (top) or MscL-v.2 (bottom). The intensity profiles are extracted along the yellow cross-sectional line reported in panel B.

C. Co-localization analysis of the myr-GFP with either the MscL-v.1 or the MscL-v.2 channel. The signal of the myr-GFP is correlated more strongly with the MscL-v.2 (r= 0.86±0.04, n= 8) when compared to MscL-v.1 (r= 0.54±0.02, n= 11), at the membrane edge. Values are reported as mean ±

standard errors of the mean (SEM). The difference between the means of the two data sets is statistically significant, with a p value < 0.0001.

Quantitative evaluation of the co-localization index of the two fluorescent proteins by Pearson correlation analysis showed a coefficient of 0.54±0.02 (n= 11) for the MscL-v.1 construct, indicating no significant co-dependency between the two fluorescence signals, and a coefficient of 0.86±0.04 (n= 8) for the MscL-v.2 construct, which confirmed a successful increase in membrane expression of the engineered MscL ion channels (Figure 16C).

Importantly, neurons expressing the MscL-v.2 protein showed a good expression level of the channel even at later days in culture (20 DIV), both in the soma, neurites, and spine-like structures, thus indicating that MscL-v.2 expression was well-tolerated in primary neurons (Figure 17A). However, considering that an enhanced mechanosensitivity could affect neurite growth and branching during network development, we compared the complexity of the dendritic tree of neurons expressing the MscL-v.2 channel with respect to neurons expressing only the membrane-targeted GFP.

Furthermore, this analysis was carried out on both wild-type (WT) MscL-v.2 channel and on a gain of function MscL variant bearing a serine to glycine substitution at position 22 (G22S MscL-v.2), which leads to a lower activation pressure threshold (Yoshimura et al., 1999). In this regard, the lower activation threshold reported by the G22S MscL channel may represent a desirable feature for accomplishing the selective mechanical stimulation of neurons within neuronal circuits.

As illustrated in Figure 17B, the morphology of neurons expressing either WT or G22S MscL-v.2 channel did not show any significant alteration in terms of neurite length and number of primary branches, when compared to the control neurons expressing only the myr-GFP. In addition, the complexity of the overall neuronal arborization was unaltered, as determined by the similar number of endpoints

between neurons expressing the myr-GFP or neurons expressing one of the two versions of the MscL-v.2 channel (Figure 18B).

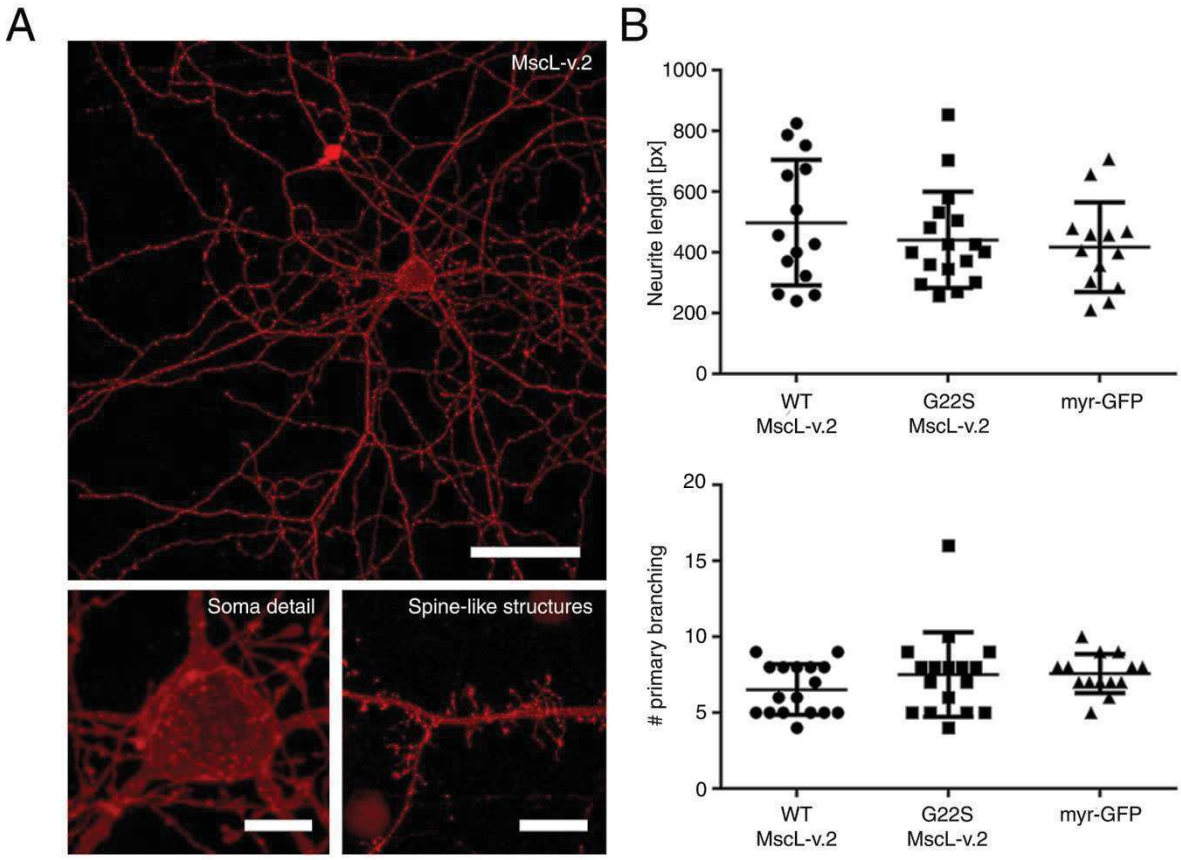


**Figure 17 | Morphological evaluation of neuron expressing MscL-v.2 construct**

A. Maximum projection of a confocal z-stack of a primary cortical neuron expressing MscL-v.2 fused to tdTomato fluorescent protein (scale bar= 50 μm). The bottom images show the MscL-v.2 fluorescence signal in the soma (left, scale bar= 10 μm) and spine-like structures (bottom right, scale bar= 10 μm).

B. In the upper panel, quantification of the neurite length of neurons expressing the WT MscL-v.2 (490.30±55.20, n= 14) or the G22S MscL-v.2 (441.50±38.33, n= 17) or the myr-GFP (417.10±41.00, n= 13). The data are presented in terms of number of pixels and no statistically significant difference was measured. In the lower panel, quantification of the number of primary neuronal branches calculated for each construct (WT MscL-v.2: 6.53±0.41, n= 17; G22S MscL-v.2: 7.53±0.68, n= 17; myr-GFP: 7.57±0.34, n= 14) is reported. Values are reported as mean ± SEM and no statistically significant difference was measured.

Staining of the synaptic boutons further confirmed the unaltered number of endpoints (see section: 5. Functional characterization of mechano-sensitized neuronal networks). Taking into account the above experimental findings, together with the fact that MscL directly responds only to membrane tension

without requiring any functional interaction with other cellular elements (Cox et al., 2016; Heureaux et al., 2014), we hypothesized that the heterologous expression of such bacterial MS ion channel in primary mammalian cells should not interfere with any intrinsic mechanotransduction pathways of the cells. Therefore, we exploited the opportunity of potentially designing a new mechanotransduction pathway in mammalian cells.

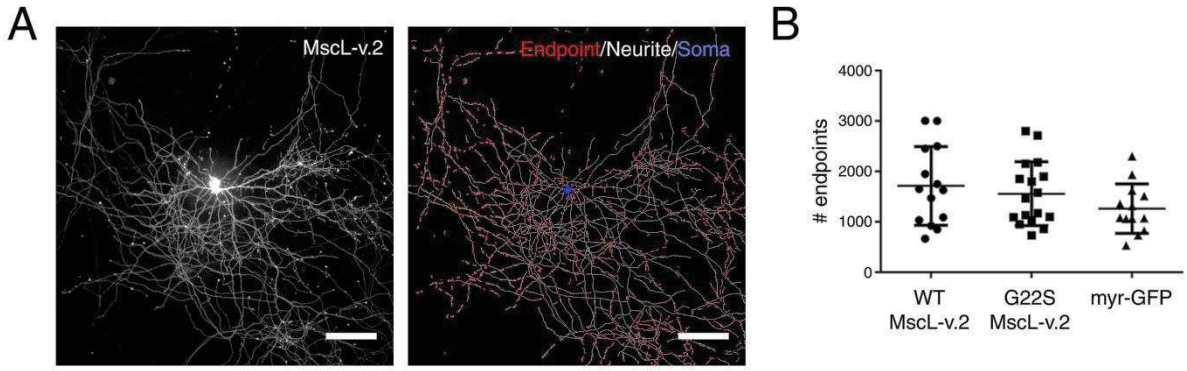


**Figure 18 | Structural analysis of the dendritic tree of single cortical neuron**
A. On the left, the fluorescence image of a cortical neuron expressing the WT MscL-v.2 construct and, on the right, the detected skeleton of the same neuron is shown. The automatically detected endpoints, neurites, and cell soma are reported in red, white and blue color respectively.
B. Quantification of the number of endpoints detected on neurons expressing the two MscL constructs, and the myr-GFP construct (WT MscL-v.2: 1714±209 endpoints on 14 cells, G22S MscL-v.2: 1559±154 endpoints on 17 cells, myr-GFP= 1262±136 endpoints on 13 cells). Values are reported as mean ± SEM and no statistically significant differences are measured.

## 3. Electrophysiological characterization of the engineered MscL channel functionality

After confirming the efficient and well-tolerated expression of the MscL-v.2 channel (hence forward indicated as eMscL), we verified its functionality and mechanosensitivity through pressure/voltage-clamp recordings in cell-attached configuration.

All recordings were performed by patching primary rat cortical neurons between 12-14 DIV (Figure 19A). A negative pressure ramp was manually applied and set to a maximum of 150 mmHg, through a custom pressure-clamp system (see materials and methods section: Patch-clamp recordings and pressure-clamp

system), in order to stretch the cell membrane into the patch pipette, and thus trigger the gating of the eMscL channel (Figure 19B). The defined maximum negative pressure is referred to be the activation pressure threshold of WT MscL (Cox et al., 2016), and a rupture of the membrane patch is likely occurring above this value. When mechanical stimulated, both WT and G22S eMscL showed different responses in terms of current amplitude, indicating the possible presence of distinct sub-conductance states of the channel, as described previously (Cox et al., 2016). Accordingly, we classified the responses into two groups: a partial response, characterized by bursts of small current events, and a full response, characterized by higher current amplitude with smaller noise and a sharp and steep closure when the pressure stimulus is removed. The partial response was often observed during the first cycles of stimulation, and was subsequently replaced by a full response. In Figure 19C and Figure 19E, we present representative traces of the induced ion currents upon stimulation of either WT or G22S eMscL channel (blue and green color traces, respectively). Control experiments (Figure 19D) were on neurons expressing only the tdTomato fluorescence protein, since a specific MscL inhibitor is not available yet. In contrast, in control neurons (n= 74 stimulation trials, on n= 15 cells) stretch-induced currents were absent. These data indicate that the currents recorded from eMscL expressing neurons were due to the specific activity of the engineered channel rather than endogenous expression of other mechanically-gated channels or Piezo family channels (Tay and Di Carlo, 2017).

Finally, we quantified the pressure activation threshold for both WT and G22S eMscL channels (Figure 19F).

Surprisingly, the partial response showed a similar activation threshold for both MscL variants (WT eMscL: 145±0.98 mmHg, n= 72 stimulation trials, on n= 19 cells; G22S eMscL: 142.50±0.91 mmHg, n= 111 stimulation trials, on n= 24 cells).

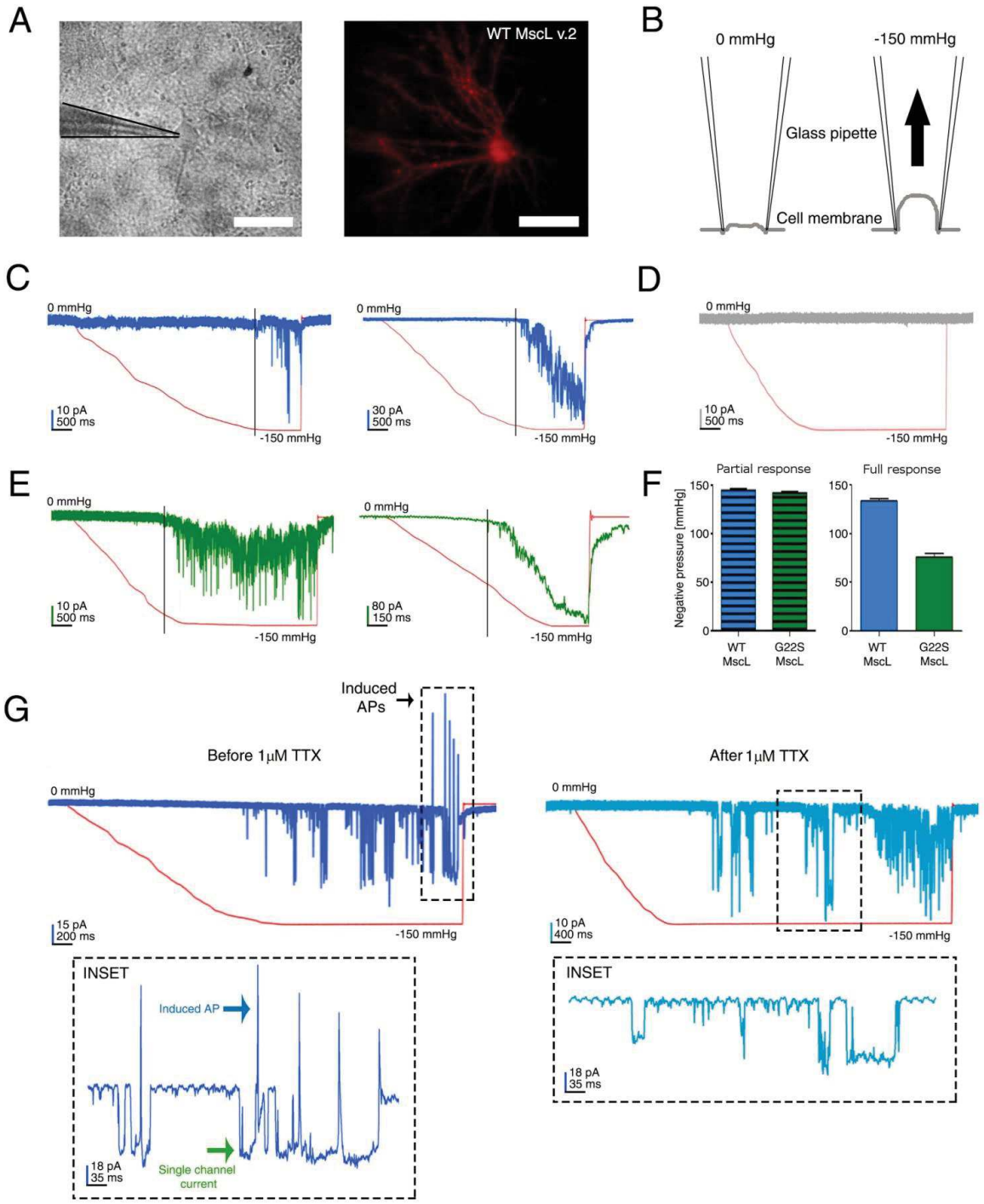


**Figure 19 | Electrophysiological characterization of the eMscL channel expressed in primary cortical neurons**

A. Bright field (left) and fluorescence image (right) of a patched cortical neuron (15 DIV) expressing the eMscL construct. The red fluorescence signal is due to the tdTomato fluorescent protein encoded by the eMscL construct. Scale bar= 50 μm.

B. Cartoon indicating the procedure to perform pressure/voltage-clamp recording in cell-attached configuration during pressure-clamp stimulation. Application of a negative pressure induces the cell membrane stretch, which activates the gating of the eMscL channel. During the stimulation, a

command potential of +30 mV was applied, and, assuming a resting potential of -70 mV, the estimated applied potential is -100 mV.
C. Traces of the recorded ion currents (blue trace) during pressure stimulation (red trace) of the membrane patch, in a neuron expressing the WT eMscL channel. On the left, the trace reports a typical example of recorded ionic currents during a partial response. On the right, the current trace of an example of recorded full response.
D. Example of recorded ion current (gray trace) during pressure/voltage-clamp recording of a control neuron expressing only the tdTomato fluorescent protein.
E. Recorded ion currents (green trace) during the pressure stimulation of a neuron expressing the G22S eMscL channel. On the left, the trace reports a typical example of recorded partial response. On the right, the trace is a representative recording of full response.
F. Bar plots reporting the quantification of the pressure activation threshold required to trigger the WT and G22S eMscL-induced currents. On the left, the quantification of the pressure threshold gating the partial response (145±0.98 mmHg, N= 72 stimulation trials, on n= 19 cells, and 142.50±0.91 mmHg, N= 111 stimulation trials, on n= 24 cells, for the WT and G22S channel respectively). On the right, the quantification of the pressure threshold histogram gating the full response (130±2.36, N= 48 stimulation trials, on n= 10 cells, and 75.78±3.60, N= 67 stimulation trials, on n= 17 cells, for the WT and G22S channel respectively). Values are reported as mean ± SEM.
G. Example of a recorded ion current trace on a cortical neuron (18 DIV) expressing the G22S channel. The traces correspond to the recorded ion currents on the same neuron before (left dark blue trace) and after (right light blue trace) incubation with 1μM TTX. The enlarged insets illustrate a detail of the recoded traces reported in the respective upper panels. The enlarged insets show the recorded single eMscL channel currents (indicated by a green arrow) and the associated generation of neuronal action potential (indicated by a blue arrow) before the incubation with TTX. After treatment of the neuron with 1μM TTX, the enlarged inset shows the sole presence of the eMscL single channel ion currents.

On the contrary, the full response showed a predictable lower activation threshold for the G22S mutant (75.78±3.60 mmHg, n= 67 stimulation trials, on n= 17 cells) when compared to the WT (130±2.36 mmHg, n= 48 stimulation trials, on n= 10 cells).

Indeed, the partial response may be due to the interaction of the cell cytoskeleton with the plasma membrane, which counteracts the membrane stretch and the complete MscL opening. Likewise, the similar activation threshold measured for the partial response in both WT and G22S expressing cells may reflect the membrane resistance to stretch (Martinac, 2014).

In this regard, for a better understanding of the strain applied on the plasma membrane, we also estimated the bilayer tension corresponding to the measured

activation pressure thresholds for the WT and G22S channels (see materials and methods section: Estimating the applied membrane tension).

Under our experimental conditions, taking in account two values of adhesion energies of the cell membrane to the glass pipette (i.e. 3.7 $mN \cdot m^{-1}$ in case of homogenous phospholipid membrane (Ursell et al., 2011), and 1.6 $mN \cdot m^{-1}$ in the case of brain cell membrane (Suchyna et al., 2009), we estimated a tension range of 11.6÷13.7 $mN \cdot m^{-1}$ at a negative pressure of about 150 mmHg; and a tension range of 6.2÷8.3 $mN \cdot m^{-1}$ at a negative pressure of 70 mmHg. Both ranges are in line with those previously described in literature for the WT and the G22S MscL channels (Rosholm et al., 2017).

Once the functional expression of the MscL channels in neuronal cells was confirmed, we developed an adeno-associated virus (AAV) expressing the G22S eMscL to allow higher expression rates, and we again carried out the patch-clamp experiments, in order to validate the MscL-induced mechano-sensitization of neurons, when the virally encoded G22S eMscL construct is used.

Also in this case, we measured in cell-attached configuration (Figure 20A) the activation pressure thresholds of the current for the partial and full responses (141±0.48 mmHg, N= 65 stimulation trials and 70±0.72 mmHg, N= 21 stimulation trials, respectively), and we confirmed the previously measured values for the not virally encoded G22S eMscL construct.

Moreover, we measured the activation threshold of the G22S eMscL-induced currents in excised membrane patch (Figure 20B), showing that the activation pressure (67±0.14 mmHg, N= 69 stimulation trials) was similar to the value found for the G22S full response in cell-attached configuration.

Taking in account these new set of data, we also confirmed our hypothesis that the partial response, recorded in cell-attached configuration, reflected the action of the cell cytoskeleton counteracting the cell membrane stretch. Indeed, it is important to take in account that even if MscL channels are gated directly by tension along the plasma membrane, the mechanical properties of the membrane

could be altered by cytoskeletal proteins and other scaffold proteins linking the cell to the extracellular matrix (Cox et al., 2016).

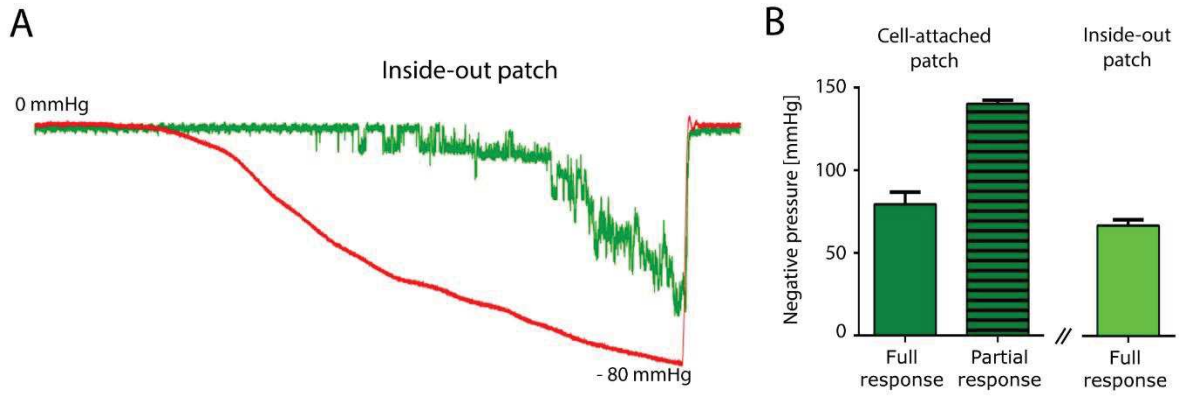


**Figure 20 | Characterization of the activation pressure threshold of the virally-encoded G22S eMscL construct**

A. Representative trace of the recorded full response (green trace) in excised patch-clamp experiment during the negative pressure stimulation (red trace).

B. Bar plots reporting the quantification of the pressure activation thresholds at which the partial (141±0.48 mmHg, N= 65 stimulation trials) and full (70±0.72 mmHg, N= 21 stimulation trials) current response in cell-attached configuration (green plots), and in excised patch (67±0.14 mmHg, N= 69 stimulation trials) configuration (light green) occur. Values are reported as mean ± SEM.

Next, we performed the same set of experiments on neurons expressing eMscL channels at later DIV (15-18 DIV), when the cultured neuronal networks is matured and neurons are able to generate spiking activity (Soloperto et al., 2016), in order to investigate a potential role of the eMscL channel in stimulating the generation of neuronal action potentials (APs). In Figure 19G, we illustrate a representative trace recorded by patching a neuron expressing G22S eMscL channel upon application of a negative pressure ramp. The mechanical stimulation was applied on the same cell patch, before and after application of 1 μM tetrodotoxin (TTX, indicated by dark and light blue traces respectively), which blocks the voltage-gated $Na^+$ channel and the generation of spontaneous APs. Induced-spike activity was present in neuron expressing both eMscL variants, and it was absent upon treatment with 1 μM TTX, while the currents induced by eMscL opening were preserved. Interestingly, only channel currents with amplitude below 50 pA were associated with the generation of action

potentials in both WT and G22S eMscL-expressing neurons (dashed black box in Figure 19G; WT eMscL: 5 out of 9 cells; G22S eMscL: 9 out of 17 cells). In contrast, eMscL-induced currents with higher amplitudes failed to trigger APs, presumably due to a massive membrane depolarization. Furthermore, we could occasionally detect an increase of the neuronal spiking activity upon mechanical stimulation (Figure 21Figure 21), thus indicating the possibility to modulate the neuronal firing rate.

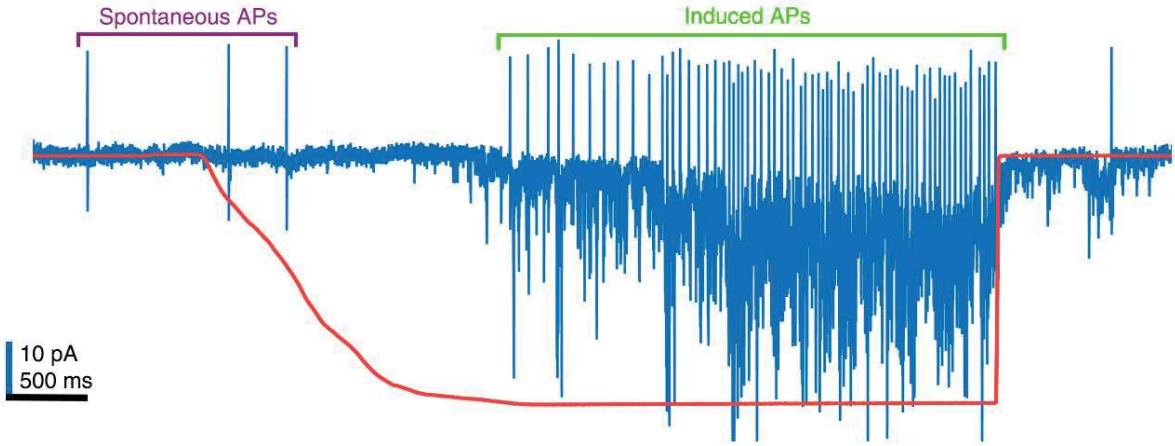


**Figure 21 | Mechanical stimulation of neuron expressing the G22S eMscL channel increases its firing rate**

Trace of the recorded ion currents (blue trace) during negative pressure stimulation (red trace) of the membrane patch, in a neuron (18 DIV) expressing the G22S eMscL channel. Violet and green lines respectively highlight the spontaneous and induced APs.

Importantly, control cells did not show any spiking activity associated with this level of mechanical stimulation (n= 15 cells), as would be expected given their lack of mechanical response. Thus, we were also able to exclude a direct cell-intrinsic dependence between the applied negative pressure and the increase in neuronal firing rate.

These experimental results illustrate the successful development of an *in-vitro* model efficiently expressing a functional bacterial MscL ion channel in mammalian neuronal networks.

## 4. Functional characterization of mechano-sensitized neuronal networks

Since a lower activation pressure of the channel could lead to its potential spontaneous gating during cell reshaping and migration, and considering that mechanical cues play an important roles in network maturation, we evaluated the effect of G22S mutant expression in network development and physiology (Figure 22). In order to obtain the high percentage of eMscL-expressing neurons within the culture which is necessary for a network-level study, we infected neuronal cultures with the previously developed adeno associated virus expressing the G22S eMscL channel fused to tdTomato fluorescent protein.

Firstly, we compared cell viability and the number of synaptic contacts in control cell cultures and in neuronal networks expressing the eMscL channel. Analyses were performed on distinct fields of view acquired on each culture (Figure 22B and Figure 22C). As illustrated in Figure 22B, cell viability was preserved in networks expressing G22S eMscL, thus indicating that eMscL membrane expression does not induce cell death (57%±3 and 63%±2 for the control and G22S neuronal networks, respectively). As a further control, we analyzed the viability of only the neurons expressing the G22S eMscL channel by staining of cell nuclei with propidium iodide dye. We again obtained cell viability of about 59%±2 (n= 9 fields of view), which is consistent with the previous results. Next, we quantified the number of glutamatergic and GABAergic synapses by immunostaining for the specific markers VGLUT1 (vesicular glutamate transporter 1) and VGAT (vesicular GABA transporter), respectively. Both the VGAT/VGLUT1 ratio (0.81±0.02, n= 6 for the control networks and 0.83±0.03, n= 8 fields of view for the eMscL expressing networks), and the number of excitatory and inhibitory synaptic puncta per cell (Figure 22C, left and right panel respectively) did not show any significant differences between the control and the eMscL expressing

networks. Therefore, we can conclude that expression of the eMscL channel does not alter the establishment of neuronal connections.

After having verified efficient development of our neuronal networks *in-vitro*, we monitored the spontaneous calcium activity after 20 DIV (Figure 22D) using Fluo4 calcium dye. In Figure 22E, we report a representative trace of the normalized fluorescence calcium signal of a single neuron, indicated as $\Delta F/F_0$. The grey line is the raw calcium trace, and the superimposed black line is the result of the denoising algorithm (see materials and methods section: Calcium imaging and data analysis). The red dots indicate the onset times of the automatically detected calcium events. After extracting and detecting the events of all cells identified within the field of view, we constructed a raster plot of the spontaneous neuronal network activity with single-cell resolution (Figure 22F).

We quantified the mean firing rate (MFR) of neuronal networks expressing the G22S eMscL channel and compared it to the MFR of control neuronal networks (n= 12 and 10 cell cultures, respectively). No significant change was detected between the two types of network (Figure 22G, left panel). As a further control test, we also compared the MFRs of single neurons expressing the virally-encoded eMscL construct (n= 917 cells) and control cells (n= 1380 cells), taken from the same network, confirming that the single cell MFR was unchanged upon eMscL expression (Figure 22G, right panel). These results show that eMscL expression does not alter neuronal development and integration into a functional network.

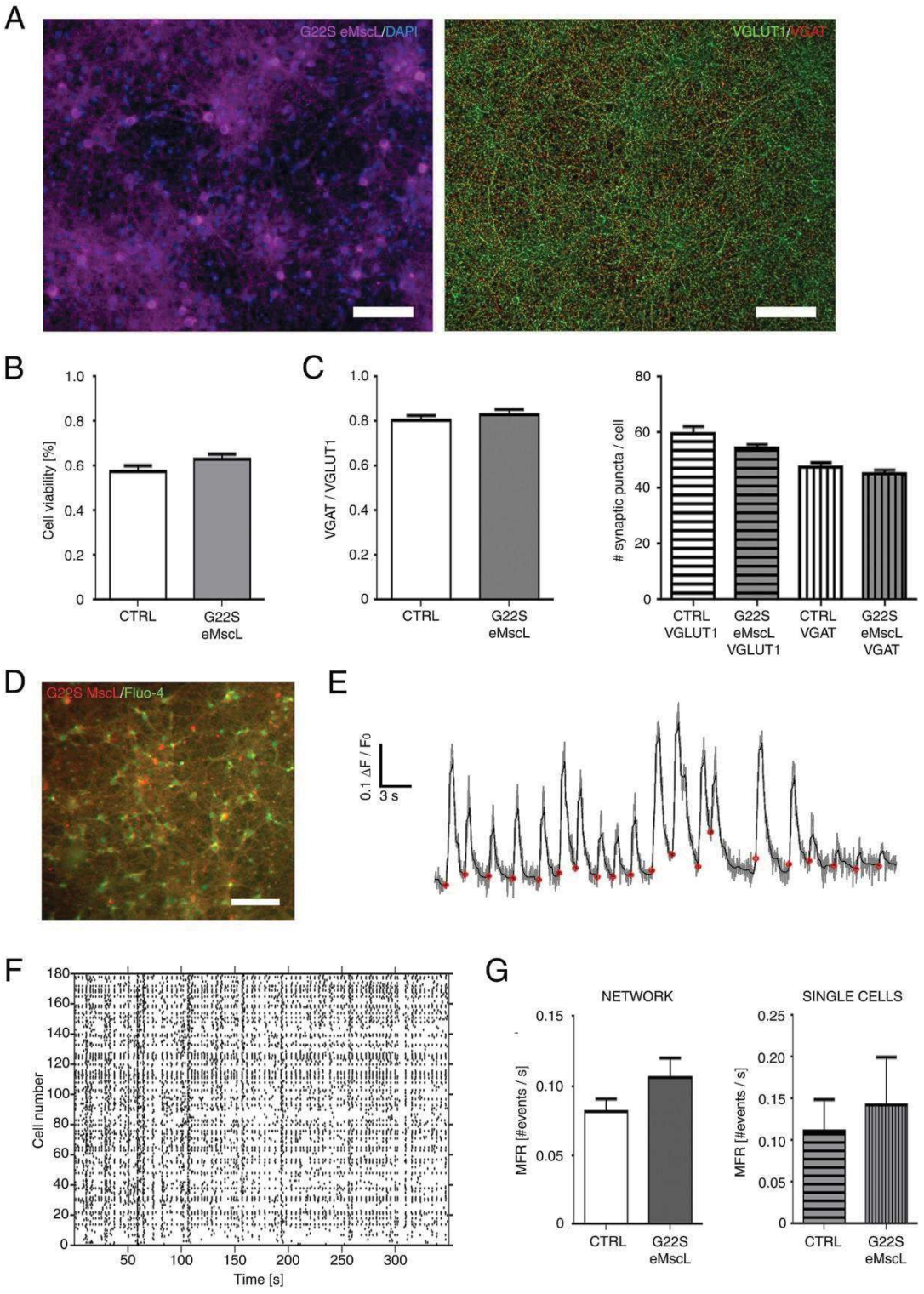


**Figure 22 | Functional characterization of cortical neuronal networks expressing the G22S eMscL channel**

A. Fluorescence images of a cortical neuronal network (20 DIV) infected with the adeno-associated virus expressing G22S eMscL channel. On the left, the magenta color indicates the fluorescence signal of the tdTomato tagged to the eMscL channel and in blue the fluorescence of the DAPI nuclear staining. On the right, the fluorescence image of the excitatory and inhibitory

synaptic puncta immuno-labeled with the VGLUT1 and VGAT markers (respectively in green and red color). Bars are 100 μm.

B. Bar plot of the percentage of viable cells of control cultures and cortical neuronal networks expressing the G22S channels (57%±3 and 63%±2 for the control and G22S neuronal networks respectively). Values are reported as mean ± SEM.

C. Bar plots reporting on the left, the ratio of VGAT/VGLUT1 synaptic puncta (0.81±0.02 and 0.83±0.03 for control and the eMscL expressing networks, respectively), and on the right, the number of VGAT and VGLUT1 synaptic puncta per cells. The average of synaptic puncta per cells were measured and normalized with respect to the average number of cells per field of view (for control network: VGAT= 47.60±1.70 and VGLUT1= 59.50±2.75 on 6 fields of view; for G22S expressing networks: VGAT= 64.32±19.25 and VGLUT1= 54.50±1.30 on 8 fields of view). Values are reported as mean ± SEM.

D. Fluorescence image showing the field of view of a neuronal network expressing the G22S eMscL channel (in red), and the Fluo4-AM calcium indicator (in green). Scale bar= 100 μm.

E. Example of a single neuronal $\Delta F/F_0$ trace of a cortical network (20 DIV). The denoised trace is shown in black and superimposed on the raw trace (reported in gray color). The red dots indicate the automatically detected onset time of calcium fluctuation events (see materials and methods section: Calcium imaging and data analysis).

F. Raster plot of the spontaneous calcium activity of single cells identified in the field of view of the neuronal network.

G. On the left, bar plots of the mean firing rate (MFR), expressed as number of events per second, of control and G22S eMscL expressing neuronal networks (n= 10 and 11, respectively). On the right, MFR plot of single cells expressing or not the G22S eMscL channel within the same neuronal networks (n= 917 and 1380, respectively). Values are reported as mean ± SEM.

## 5. Ultrasound and optical system integration layout

Since the long-term vision of the project is to also establish the potential of ultrasound as a stimulation technology, and in order to test and calibrate the capability of US waves to modulate the activity of neuronal networks, we integrated the previously used wide-field fluorescence microscope with an *in-vitro* US delivery system (Figure 23), and the microscope stage was equipped with a sample holder which contains housings for the culture dish and the US probe aligner.

The time lapse calcium imaging was synchronized with the US delivery system through triggering signals, in order to evaluate the effect of distinct US stimulation protocols on the neuronal network activity at both single cell and

network level. The microscope was designed to include two excitation light sources and two dedicated filter sets (indicated in Figure 23 as $\lambda_1$ and $\lambda_2$), allowing imaging with different fluorescent markers, i.e. red or green emission calcium sensors combined with complementary fluorescent dyes used to label different cell-types or genetically modified cells.

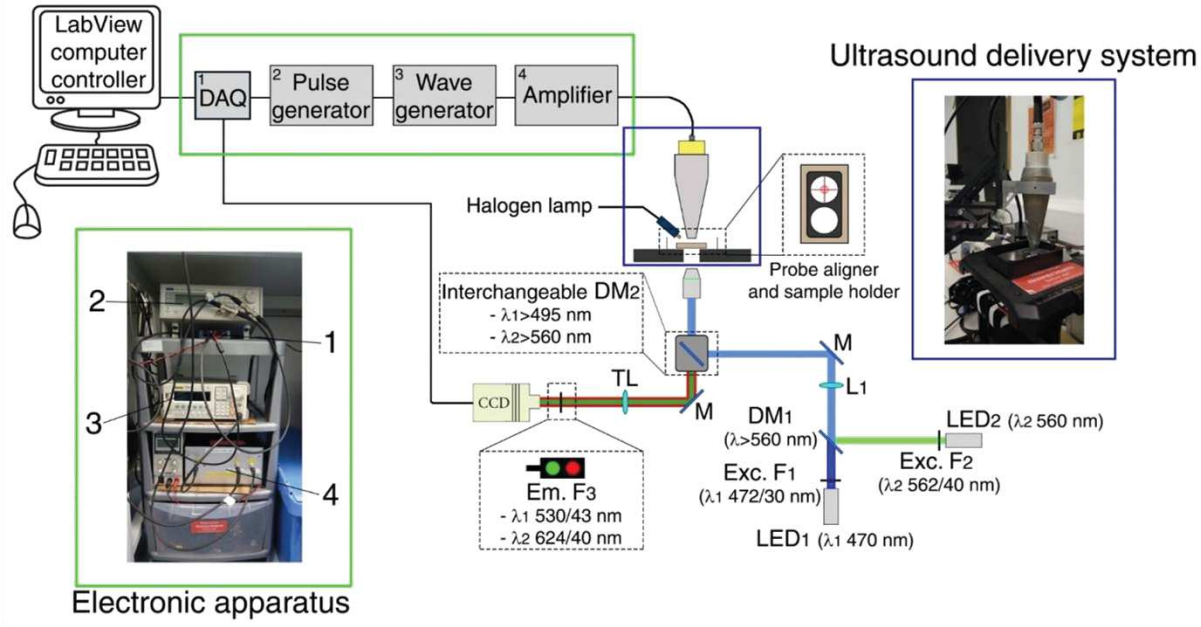


**Figure 23 | Schematic layout of the ultrasound stimulation system integrated in the custom fluorescence microscope**

In the green box the electronic apparatus employed for the generation of the ultrasound stimulation protocol are shown. A custom LabView software is used to trigger the US stimulus, at a fixed frequency, through a data acquisition device (1) to the tone burst wave generator (2). In response to the trigger, the wave generator provides a US tone burst at a defined frequency and number of pulses in a single US stimulus. Then, a second wave generator (3) is used to trigger, within every single tone burst, the sinusoidal US waveform at an experimentally defined frequency and with a variable number of cycles. Finally, the US wave generator is connected to a custom built amplifier, which receives the input voltage from the wave generator and provides the output power to an US transducer.

In the blue box, the ultrasound delivery system consisting of ultrasound transducer, US condenser and sample holder is shown.

In the red box, two excitation light sources and dedicated filter sets, indicated as $\lambda 1$ and $\lambda 2$, are shown. CCD: charged coupled device camera; DM: dichroic mirror; M: mirror; F: filter; L: lens; TL: tunable lens.

The US source was a piezo transducer, having a nominal resonant frequency of 340 kHz, coupled with a custom built US condenser, which allows transmission

and focusing of the US field away from the transducer. This configuration facilitated integration with the fluorescence microscope, and prevented contamination of the optical imaging by auto fluorescence generated from the coating layer of the piezo-transducer when placed in closer proximity to the optical focal plane. Moreover, the US condenser also reduced the active area of the US field from approximately 22 mm diameter (the diameter of the US transducer element) to about 8 mm, which makes the system suitable for integration with patch-clamp measurements. The US delivery system is aligned with respect to the field of view of the microscope through the probe aligner. Upon alignment, the US delivery system is maintained fixed and the microscope stage is moved in order to position the cell chamber below the output window of the US condenser.

In Figure 24A-C, we report the cross-section view and the related technical drawings of the US delivery system including the stainless steel propagation cone acting as US condenser, and US compatible cell chamber.

The walls of the cone are thick about 6 mm because the US waves should not induce strong vibrations of the condenser wall, and avoid multiple reflection of the US waves at the air interface. In such a way, we avoided the generation of multiple US wavelengths which could create uncontrolled interferences within the condenser.

At the tip of the cone, as the US waves were already well focused, the wall thickness was decreased in order to reduce its steric hindrance at the sample chamber. Considering that low-frequency ultrasound has a beam profile with significant lateral spread, the focusing of the US waves avoid the interaction of US with the wall of the cell culture which could generate unwanted standing waves. Therefore, in such a way the only surface of US reflection is the bottom layer of the sample dish. In this regards, the use of a long working distance (about 1 cm) and low magnification objective avoid the back reflection of US waves from the microscope objective.

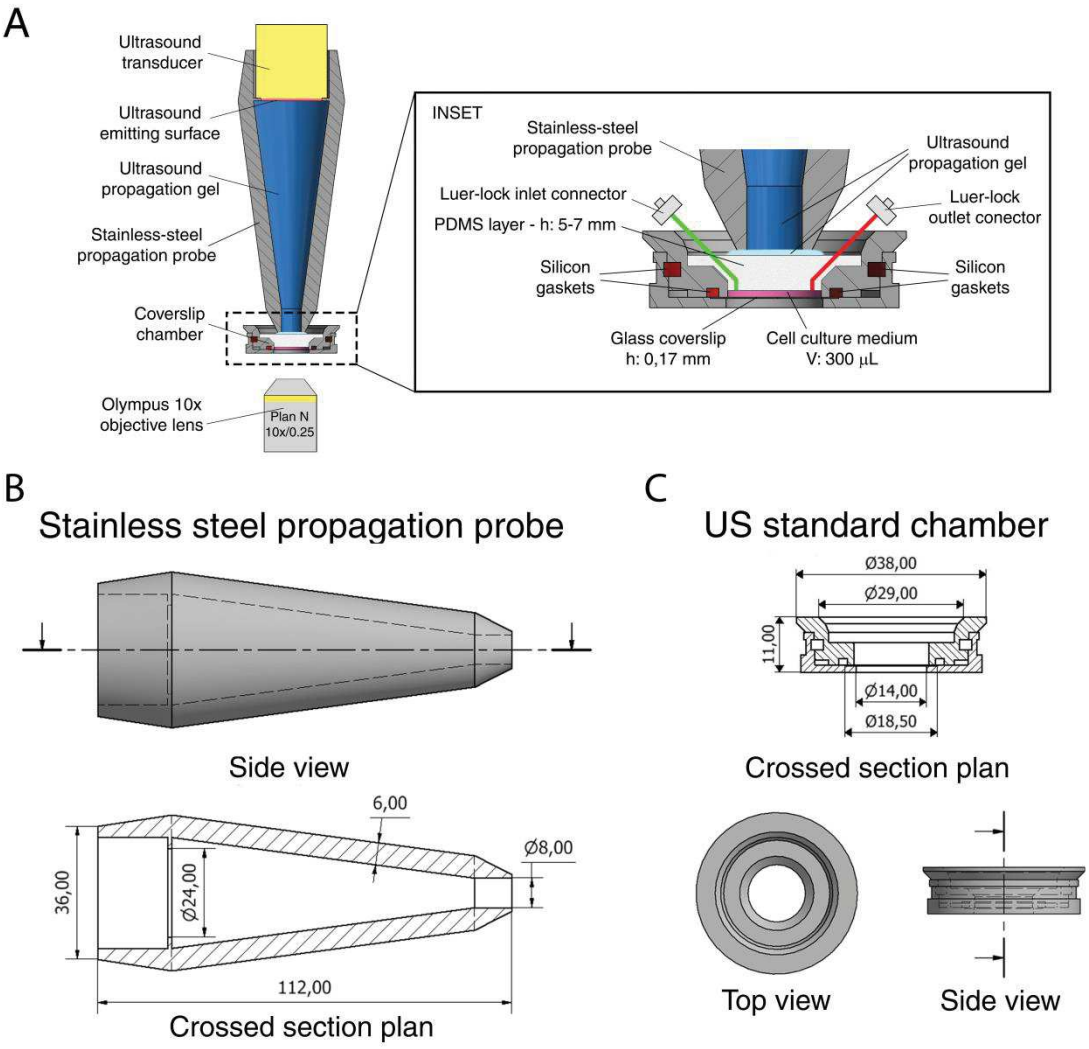


**Figure 24 | Ultrasound delivery system**

A) 3D printed components of the ultrasound delivery system. The inset displays a medial cross-sectional view of the US compatible coverslip chamber with all its components.

B) Technical drawing of the stainless steel ultrasound condenser is shown.

C) Technical drawing of the ultrasound compatible cell chamber is shown.

Once the integration of the US and imaging devices was achieved, US could be efficiently delivered into the cell chamber.

The latter was designed to maximize US transmission towards the biological sample, and avoid reflections at the interface between the output section of the US condenser and the cell chamber. In this regard, PDMS was selected as a constitutive material for the cell chamber lid, given that its acoustic impedance is comparable to the one of the transmission medium.

For the US stimulation experiments, the cell coverslip was inserted between the circular base and cap disk and then the chamber was assembled through application of a gentle pressure. A silicon gasket was inserted at the bottom of the cap disk in order to prevent fluid leaks when coupled with the circular base (Figure 25).

The acoustic coupling between the output window of the US condenser and the PDMS lid was achieved using a thin layer ultrasound gel. This layer of gel also reduces friction between the US condenser and the PDMS lid of the chamber, making it possible to move the microscope stage and identify the desired optical field of view within the neuronal culture sample, without perturbing the alignment of the fixed US probe.

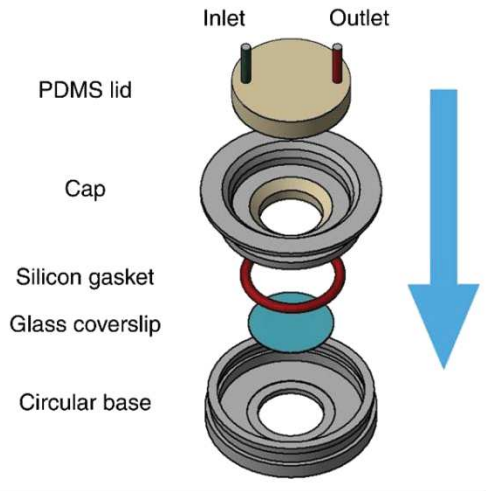


**Figure 25 | Assembly of the ultrasound compatible cell chamber**
The circular base is coupled with the cap disk and silicon gasket, and a PDMS lid is baked on the top surface of the cap disk. The blue arrow indicates the direction of assembly.

In the inset of Figure 24A, we show the detailed design of the US compatible cell chamber. The PDMS lid of the chamber has a thickness of about 5-7 mm, and it is equipped with an inlet and an outlet tubing which allows the easy exchange and fulfilling of the medium solution within the small volume of the chamber of about 300 μL. Importantly, given that the acoustic impedances of PDMS and water are very similar (Carugo et al., 2015), there is negligible sound reflection at

the water–PDMS interface, and the attenuation of the incident sound field is marginal.

Moreover, numerical simulations were performed to determine the flow field within the cell chamber and the sealing (Figure 26). For the numerical simulation, the reference nominal flow rate at the inlet ($Q_{IN}$) was set at of 1 mL·min$^{-1}$, however other flow rates were also taken in account during the simulation in order to define the flow rate range at which any cell damage or activation was not elicited (Figure 26B). In particular, the Figure 26A illustrates the fluid shear stress distribution (in Pa) over the bottom surface of the coverslip chamber, which corresponds to the area where cells were seeded. The maximum shear stress was exerted around the inlet region, with a peak value of about 0.15 Pa, which is lower than values reported to alter cell viability and cell adhesion (Douville et al., 2011) or to elicit a biological response (Hua et al., 1993), which are on the order of about 1 Pa. Moreover, the panel A shows the flow streamlines and velocity simulation set at $Q_{IN}$= 1 mL·min$^{-1}$, during the filling-in of the chamber or exchange of medium solution, at which we refer as priming process. The absence of vortices during the priming, it is a notable feature since unwanted and uncontrolled mechanical stimulations of the neuronal networks are avoided.

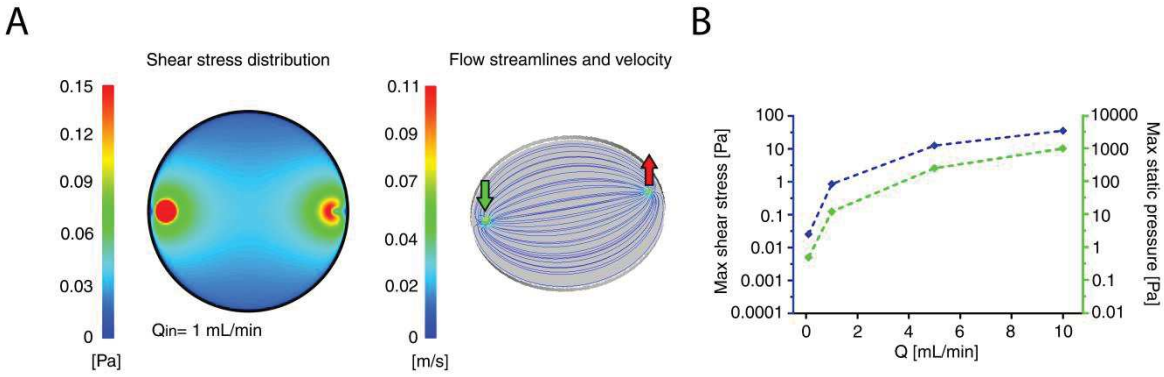


**Figure 26 | Computational fluid dynamics study**

A) The left panel shows the shear stress distribution (in Pa) over the bottom surface of the coverslip chamber. The black circle corresponds to the region where cells are seeded. The right panel shows the flow streamlines and velocity (in m·s$^{-1}$) within the chamber. The green and red arrows correspond to inlet and outlet boundaries, respectively. The shear color map and streamlines color are calculated at the nominal flow rate ($Q_{IN}$) of 1 mL·min$^{-1}$.

B) Maximum shear stress (in Pa) and maximum static pressure (in Pa) measured at six different flow rates is indicated.

## 6. Calibration of the ultrasound delivery system

In order to provide an accurate testing and calibration of the mechanical stimulation paradigm of neuronal cells, we calibrated the pressure field generated by the US waves at the sample plane. First of all, we characterized the output pressure of the US transducer connected with the US condenser through a water tank calibration system (Figure 27A), and thus defined its maximum resonant frequency, which resulted slightly shifted from the nominal resonant frequency of the sole piezo transducer to about 380 kHz (Figure 27B). After setting the driving resonant frequency of the system, we calibrated its output peak pressure with respect to the peak to peak voltage amplitude ($V_{PP}$) of the driving signal (Figure 27C). Therefore, we quantified a maximum output peak pressure of our US system of about 105 kPa, which well matched the range of values reported in literature to accomplish nonthermal US cell stimulation (Kubanek et al., 2016). Moreover, we characterized the pressure loss in the axial direction propagation from the output of the US condenser toward to the neuronal culture plane, estimating a maximum pressure peak of about 90 kPa (Figure 27D).

Finally, we measured the US pressure field generated at the sample plane (Figure 27E and Figure 27F) of the microscope chamber, in order to verify the proper far field focusing of the US waves. In Figure 27E, we report the normalized intensity pressure field generated by the transducer with US condenser and the US-lid of the microscope chamber. The pressure field showed a distribution of values higher at the US focus center, thus confirming a proper far-field focusing of the US waves. Moreover, by measuring the pressure intensity profile along the black sectional line in Figure 27E, it become evident that the pressure is maintained

almost flat over about 5 mm of the stimulation field. Therefore, we can conclude that the US transducer and condenser together with US compatible cell chamber creates a pressure field which could be considered constant among a large area of the sample, allowing an homogenous US stimulation of the neuronal network.

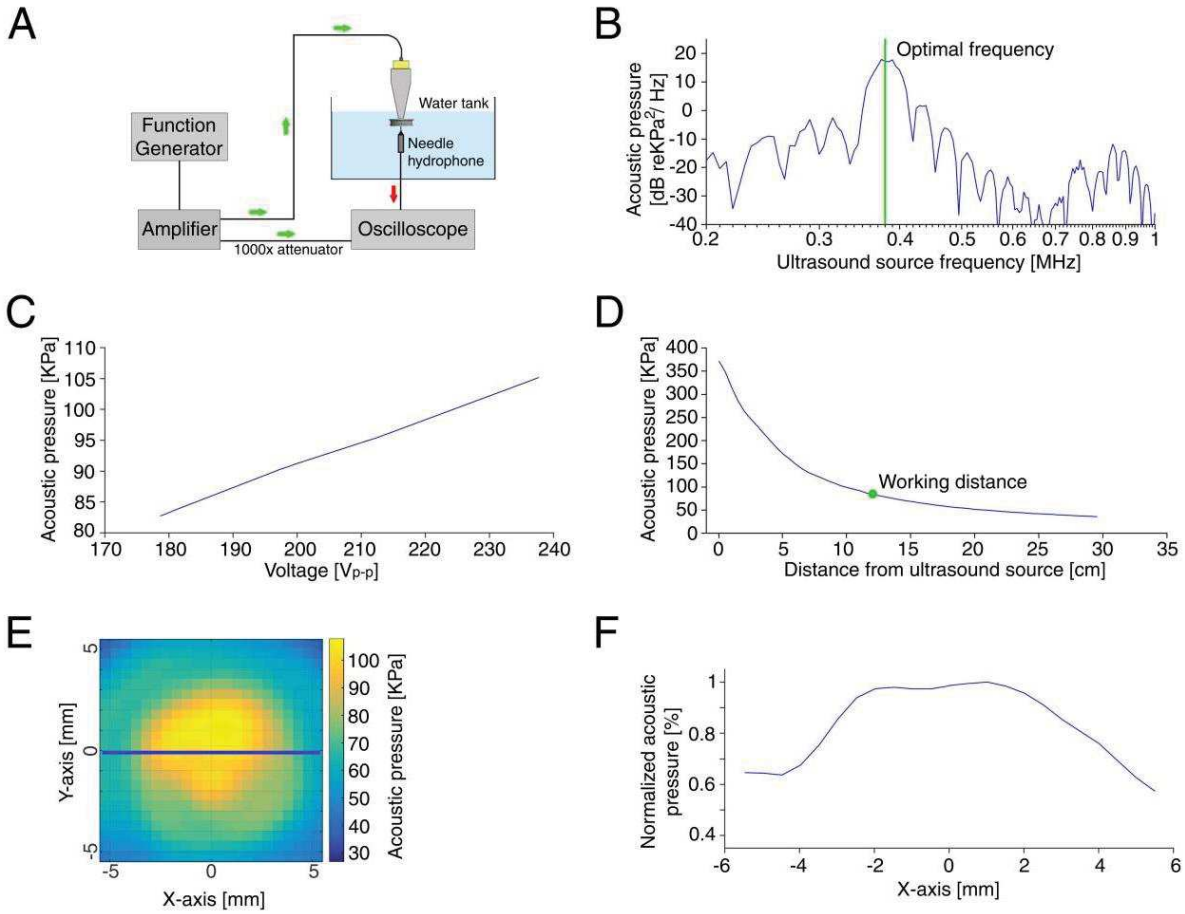


**Figure 27 | Acoustical calibration of US delivery system**

A) Calibration setup for characterizing the acoustic properties of the ultrasound delivery system.

B) Acoustic pressure measured at different ultrasound frequency in order to define the maximum resonant frequency. The green line shows the maximum resonant frequency.

C) Acoustic peak pressure (in kPa) as a function of the output voltage.

D) Pressure attenuation profile in the axial direction propagation from the output of the US condenser toward the neuronal culture plane.

E) A color intensity plot showing the acoustic pressure distribution (in kPa) on the cell culture surface upon the ultrasound stimulation measured at US frequency of 380 kHz and output voltage of 210 Volts.

F) Normalized acoustic pressure at the target plane along the sectional line shown in panel E.

## 7. Ultrasound stimulation of neuronal networks

The calibrated and almost constant pressure field on the neuronal culture plane is an extremely favorable condition to combine calibrated US stimulation with the subcellular resolution of a wide-field imaging system. Indeed, once the US pressure field is aligned on the center of the microscope field of view, it is possible to perform high-throughput analysis of the effect of US mechanical stimulation on single neurons.

In this regard, we investigated the influence of calibrated US pressure waves on mature primary rat cortical neuronal cultures (15 - 24 DIVs) by tracing the calcium fluctuations with the fluorescent calcium indicator Fluo4-AM (Figure 28A, left panel). Since the thin cell culture monolayer behaves as acoustically transparent, we targeted the negative charged plasma membrane with positive charged air-filled lipid microbubbles, in order to locally amplify the mechanical stimulation provided by US pressure waves over the cell layer. Indeed, given the close adherence of the positive-charged microbubbles to the cell membranes, their relative small oscillation amplitude upon the application of low-intensity ultrasounds can create a higher mechanical effect on the cell membrane, and thus represents a potential biocompatible solution for providing the local amplification of the membrane strain produced by the US pressure waves (Heureaux et al., 2014; Ibsen et al., 2015). We added the microbubbles to the culturing medium solution within the cell chamber, and by flipping upside-down the chamber we favored the non-specific adhesion of the microbubbles to the neuronal plasma membrane, obtaining an almost uniform distribution of microbubbles on the neuronal culture (Figure 28A, right panel). After that, we exchanged the culture solution to remove the unbound microbubbles, which could generate local fluidic streaming and uncalibrated shear stresses to neuronal cultures. The image of microbubble distribution on the neuronal culture plane was obtained by collecting the light scattered from the air filled contrast agents

through the oblique illumination of the sample performed with a fiber of a halogen lamp. The dimensions of the microbubbles has been measured by optical imaging (Figure 28B), reporting an average diameter of about 4 - 5 μm, which is below the approved threshold set by the FDA for clinical application.

The single US stimulus was constituted of a US pulsed wave, in order to reduce unwanted thermal effects and generation of uncalibrated US standing waves within the chamber (Figure 28C). The single US stimulus was composed by several tone bursts with distinct pulse repetition frequencies.

We performed cyclic US stimulation, lasting 1 second, with a pulse repetition frequency (PRF) of 0.2 Hz, simultaneously performing calcium imaging in order to detect and quantify the response of the cells to the US pressure waves. The US stimulation protocols were performed both in presence and absence of membrane targeted microbubbles. However, all the neuronal cultures did not present any significant response to the US stimulation in absence of the microbubble. Each experimental session lasted about 3 minutes, to which corresponded about 36 trials of US stimulation. As reported in the Table 2 in the materials and methods section "Ultrasound delivery system", different ultrasound stimulation protocols were tested. In the specific case of the example reported in Figure 28, we used US protocols having a PRF of 0.2 Hz and a tone burst frequency (tbf) of 20 Hz with 150 cycles per tone burst (c/tb), exerting an acoustic pressure of about 90 kPa per stimulation.

In Figure 28D, top panel, we reported the normalized calcium traces (reported as $\Delta F/F_0$) of some single cells detected within the field of view. The superimposed violet shadow lines represent the window time in which US stimulation is applied. The gray trace reports an example of a non-responding cell. The red trace shows the response of a cell with a slow growing fluorescence intensity associated to the intracellular calcium increase. Usually slow dynamic calcium fluctuations are associated to neuronal glial cells.

Finally the blue trace reports an example of typical calcium fluctuations of neuronal cell, presenting calcium events with a fast grow of the fluorescence intensity, synchronized with the onset of US stimuli, followed by a slow decaying phase.

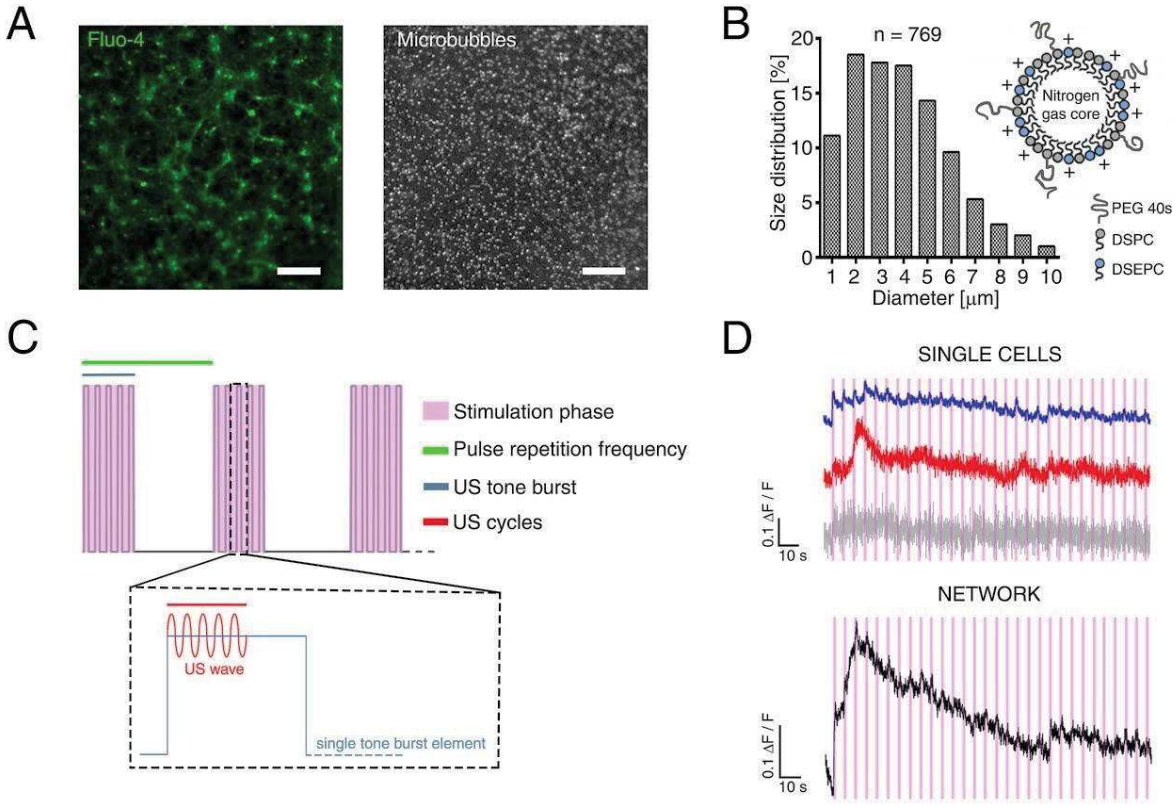


**Figure 28 | Ultrasound stimulation of neuronal network**

A) Fluorescence image of neurons loading Fluo-4 green calcium dye (left panel) and bright field image of lipid-shell microbubble layer (right panel) targeted over the cell culture. Images are acquired through a 10X air objective. Scale bar= 100 μm.

B) Histogram showing microbubble size in terms of percentage distribution and a schematic representation of the microbubble's structure. DSPC: 1,2-distearoyl-sn-glycero-3-phosphocholine; DSEPC: 1,2-distearoyl-sn-glycero-3-ethylphosphocholine; PEG 40s: Polyoxyethylene (40) stearate.

C) The panel shows a detailed view of the ultrasound stimulation protocol. The DAQ device generates a 5 $V_{pp}$ trace with a duration of 1 second at the frequency of 0.2 Hz and drives the emission of a single US pulse (pink box). Then, the pulse step triggers the US tone burst, a 5 $V_{pp}$ square wave (blue) generated by the function generator. In response to the tone burst, the wave generator produced a 5 $V_{pp}$ sinusoidal wave (red) at a frequency of 380 kHz within each single tone burst element.

D) The upper panel shows the normalized calcium traces of single cells detected within the field of view showing a calcium response with a fast decay (blue), a calcium response with a slow decay (red) and a non-response (gray). The lower panel shows the normalized calcium trace of

the whole neuronal network within the field of view. The stimulation protocol is set with the following properties: PRF= 0.2 Hz, tb= 20 Hz, c/tb= 150.

In the bottom panel of Figure 28D, we report the average calcium trace of the whole neuronal network, calculated as average of all the single calcium traces detected within the field of view. A fast and stepwise increase of the average calcium intensity of the cells was achieved at about the 4th US stimulus. After that, a slow compensation dynamic of the intracellular calcium produced a recovery of the initial fluorescence intensity. However, also during the compensation phase of the networks, some fluctuation peaks associated with the time of US stimuli were still present. Therefore, we may conclude that US stimulation produces an overall increase of the intracellular calcium in the majority of stimulated cells, thus generating a response of the overall network.

# CONCLUSION AND PERSPECTIVE

Currently electrical or optical stimulation techniques are most explored strategies to dissect neuronal circuits, although they present relevant limitations for their immediate and wide clinical application.

In this regard, the opportunity to provide cell-type or tissue-specific sensitization to externally controlled type of stimuli, it is inspiring the development and assessment of novel stimulation methods either exploiting nanotechnology and/or genetic engineering of cellular sensing elements. Indeed, the development of novel approaches to modulate the activity of neurons and deep brain circuits is pivotal for (i) the fundamental understanding of brain (dys)functions as well as (ii) the design of effective therapeutic strategies to treat neurological disorders.

Under these perspectives, considering the growing evidences of the role of mechanical cues in defining cell differentiation, tissue development and physiology, together with the peculiar characteristic of mechanical signals which could be easily transmitted through dense tissues, the choice of using ultrasounds as type of externally controlled stimuli, for generating localized pressure fields is attracting a lot of attention in research community.

However, although ultrasounds offer the potential for a non-invasive remote modulation of the brain activity upon low-intensity mechanical stimulation (Tufail et al., 2010; Tufail et al., 2011), the lack of a tunable and specifically responsive mechanosensitive element, such as a membrane ion channel, it is not

fostering the development of new cell-type specific ultrasound-based neuromodulation approaches.

In fact, it is important to take into account that while neuronal cells are inherently equipped with several ion channels, these are simultaneously sensitive to a wide number of stimuli including the mechanical ones, and upon ultrasound stimulation, all cells could be unspecifically stimulated.

Thus, in order to provide cell-type specificity to US stimulation, the mechano-sensitization of a well-defined cell populations through the overexpression of mechanosensitive ion channels has been proposed, in analogy to the cell-type specific light sensitization occurring in optogenetics (Ibsen et al., 2015; Zhou et al., 2017).

For all the above reasons, during my PhD study, I focused my research activity on the development of an *ad hoc* mechano-sensitized neuronal *in-vitro* model, to ultimately pave the way for the selective mechano-activation of targeted neuronal cells through the use of low-intensity ultrasound, as postulated in the sonogenetic paradigm (Ibsen et al., 2015).

In nature, only few ion channels are known to be exclusively-mechanosensitive, and for this purpose, we propose the bacterial MscL as the ideal candidate to obtain a cellular mechano-sensitization. Indeed, MscL bacterial ion channel is the only exclusively-mechanosensitive channel with a detailed structural and functional characterization, which has already been exploited in biotechnological applications (Doerner et al., 2012; Iscla and Blount, 2012; Kocer et al., 2005). Moreover, taking into account that MscL directly responds only to membrane tension without requiring any functional interaction with other cellular elements (Cox et al., 2016; Heureaux et al., 2014), we hypothesize that the heterologous expression of such bacterial MS ion channel in primary mammalian cells should not interfere with any intrinsic mechanotransduction pathway of the cell, and thus we envisage the opportunity of potentially designing new mechano-dependent pathways.

In our experimental results, we report an engineered MscL construct enclosed into a neuronal specific adeno associated viral vector, specifically designed for achieving an efficient neuronal mechano-sensitization. Indeed, the use of AAV vector allowed the long-term and well-tolerated functional expression of the eMscL channel in primary neuronal cultures without affecting the physiological development of neuronal networks. Although the degree of invasiveness associated to this approach is lowered in respect to currently in use neuromodulation approaches, it is important to take into account that the use of viral vector for genetically engineering the neuronal population is still required.

Moreover, since the long-term vision of the project is to pave and foster the establishment of a potentially new generation of neuro-stimulation technology, we report the development of an *in-vitro* setup that combines the fluorescence calcium imaging of neuronal networks with a custom designed US delivery system, in order to perform high throughput studies of the ultrasound stimulation at single cell resolution. We also provide an accurate and rigorous calibration of the US pressure fields at the sample plane which confirms the proper design and the efficient far-field focusing of US waves on a large area of the cell culture. In fact, the US system generates an almost constant acoustic pressure field, thus allowing to test and evaluate the effect of distinct stimulation protocols on a wide number of cells within a single field of view of the microscope.

Given the above, the reported model of mechano-sensitized neuronal networks, together with the US delivery system, could be exploited to gain new insights into the mechanobiology of the nervous system, and it could pave the way for the development of implant-free stimulation approaches. Moreover, it is worth to note that further manipulations of the MscL gene sequence can be defined in order to control gating, mechanical sensitivity and conductance of the MscL protein (Kocer, 2015) (Kocer, 2015; Yoshimura et al., 1999), and thus making only the cells expressing the eMscL responsive to the generated US fields. Indeed,

considering that all cells show some intrinsic mechanism of mechanosensation (Wu et al., 2017), the possibility to tune the mechanosensitive properties of the eMscL channel, with respect to other cells and cellular sensing elements, becomes a crucial feature to accomplish cell-type specific mechanical stimulation, and overcome the limit of the intrinsic cellular mechanosensitivity. In this regard, two recent studies exploiting the pressure field generated by propagating US waves showed the possibility to achieve spatially resolved neuronal stimulation either by the genetic expression of MS channels (Ibsen et al., 2015), or the accurate design of the US propagating wavefront (Zhou et al., 2017). Therefore, the development of a cell-type specific stimulation approach would require both the expression of MS channels with a well-tuned mechanosensitivity, and the accurate shaping and calibration of the locally generated US pressure fields.

Another distinctive property of the MscL channel is its nominal conductance (3 nS, (Kung et al., 2010)), which could be too high for neuronal cells. Nevertheless, the large conductance of the channel could represent a beneficial feature to accomplish shorter and gentler stimulation of cellular activity and, it could be modified accordingly through site-directed mutagenesis assay (Yang et al., 2012). Another characteristic of the MscL, which is critical for its successful usage in *in-vivo* models, is that it is not ion selective and is not straightforward to change the selectivity of such a large pore. Indeed, the channel opening could produce a calcium influx which would elicit cellular apoptotic pathways. However, the use of MscL channel in mammalian cell cultures as a tool for the controlled delivery of bioactive molecules (Doerner et al., 2012) has been previously reported without any significant drawback. The authors of this study showed that cell viability was preserved also for long temporal opening of the channel (in the order of few minutes) in presence of $Ca^{2+}$ ions in the bath solution.

Nevertheless, our results and observations confirm that the heterologous expression of a functional bacterial MscL channel in primary neuronal cultures does not affect the cell survival, the neuronal network architecture, and the

spontaneous network activity. Moreover, the generation of action potentials associated with the channel opening, upon application of a calibrated suction pressure, indicates successful mechano-sensitization of the neuronal cells, which could be used to induce and modulate neuronal activity upon mechanical stimulation. In this regard, it is important to highlight that the generation of action potentials was only associated with the partial current response elicited by eMscL upon the mechanical stimulation.

The required suction pressure to induce a partial response was about 145 mmHg, which correspond to about 0.02 MPa. Considering that the range of acoustic pressures which have previously demonstrated ability to elicit the activity of wild-type neuronal circuits is on the order of about 0.01 ÷ 0.1 MPa (Tufail et al., 2010; Tyler et al., 2008), i.e. well below the typical acoustic pressures inducing thermal or cavitation effects (Dalecki, 2004; Kubanek et al., 2016), we could deduce that the activation threshold of the eMscL channel is appropriate to accomplish its gating through the use of low-intensity US waves. However, the main challenge in achieving gating of a MS channel by US pressure waves originates from a limited understanding of the underlying mechanisms of action, and in this context particularly concerning it is the interaction between low-intensity US waves and the biological matter (Plaksin et al., 2016), and the corresponding US field required to induce effective membrane strain. These concerns have limited the identification of an optimal delivery of the US wavefront.

Additionally, the system has been developed taking into account the possibility to test the mechano-sensitized neuronal network model in a 3D cell cultures configuration, as already developed and optimized in our group (Palazzolo et al., 2017). In such a way, we could scale up the complexity of the *in-vitro* system toward a more similar *in-vivo* scenario, and thus study the effect of extracellular matrix-like mechanical (the tunable elasticity of the hydrogel scaffold used) and

structural (three dimensional growth of the network) environment on both the functionality of the MscL channel, and the mechanobiology of sensitized cells.

Indeed, moving to *ex-vivo* or *in-vivo* models will require a further optimization of the *in-vitro* established ultrasound stimulation protocols. Therefore, the employment of 3D cell culture technology could also be critical to high throughput test and adjust the US stimulation settings for *in-vivo* applications.

However, ultrasound pressure fields have been already shown to efficiently propagate through the intact rodent skull (Kubanek et al., 2016; Ye et al., 2016b; Yoo et al., 2011), so that also a direct *in-vivo* assessment of the eMscL-based sonogenetic paradigm may be pursued, and combined with behavioral tests to directly investigate and exploit the great potentiality of this novel neuromodulation approach.

Finally, the provided experimental model will allow i) to study the tissue development and physiology in term of mechanosensing and mechanotransduction, and ii) to investigate how the tissue architecture and physiology may be influenced by the simultaneous expression of the eMscL and other endogenous MS channels, thus getting further insight in the mechanobiology of neuronal circuits and in the biophysical principles of the US interaction with the biological matter.

Given the above, we believe that the mammalian-engineered eMscL construct represents an important step forward for future applications in complex animal models, in order to gain new insights into the mechanobiology of the nervous system (Koser et al., 2016b), and to pave the way to the use of low-intensity US to accomplish remote, non-invasive, local modulation of network activity within the intact brain tissue. In particular, this possible achievement would open the unprecedented opportunity for neuro-engineering applications and/or implant-free treatments of various pathological disorders.

# MATERIALS AND METHODS

## Ethical approval

All procedures involving experimental animals were approved by the institutional IIT Ethic Committee and by the Italian Ministry of Health and Animal Care (Authorization number 110/2014-PR, December 19, 2014). When performing the experiments, we minimized the number of sacrificed animals and the potential for nociceptor activation and pain-like sensation, and respected the three Rs (replacement, reduction and refinement) principles, in accordance with the guidelines established by the European Community Council (Directive 2010/63/EU of 22 September 2010).

## Primary neuronal cultures and transfection

Primary neurons were isolated from cortex tissues of Sprague Dawley rats at the embryonic age of 18 days. The female pregnant rats and mice were sacrificed through $CO_2$ suffocation and cervical dislocation, before the embryos extraction. Dissected tissues were dissociated by enzymatic digestion, incubating them in 0.25% Trypsin (Gibco) supplemented with 5 $\mu L \cdot mL^{-1}$ of 0.25 $mg \cdot mL^{-1}$ bovine pancreatic deoxyribonuclease I – 15KU (Sigma-Aldrich) for 7 min at 37 °C. Before triturating the tissues with a P1000 pipette tip, an equal volume of Dulbecco's Modified Eagle Medium (DMEM, Gibco) supplemented with 10% Fetal Bovine Serum (FBS, Gibco) was added to the suspension for blocking the

trypsin activity. Isolated cortical neurons were counted and plated at a final density of 300 cells·mm$^{-2}$ or 600 cells·mm$^{-2}$ onto 18 mm glass coverslips.

The day before the cell seeding, glass coverslips were cleaned and overnight pre-coated with 0.1 mg·mL$^{-1}$ Poly-D-lysine (PDL 70-150k, Sigma) in order to enhance cell adhesion.

Neurons were grown in neuronal medium containing Neurobasal medium (Gibco) supplemented with 2% B27 supplement (Gibco) and 1% GlutaMAX (Gibco) at 37°C/5% $CO_2$ humidified atmosphere. Cultures were maintained up to 25 DIV and fresh medium was added weekly (about 300 μL) to avoid changing in osmolarity due to the medium evaporation.

Primary neuronal cells were transfected at 2 DIV with 0.4 μg of MscL plasmid and/or 0.7 μg of myr-GFP plasmid with Lipofectamine 2000 transfection reagent (Invitrogen). A DNA to Lipofectamine ratio of 1 to 1 was mixed in 300 μL of OptiMem medium (Gibco), and added to each well reaching the final volume of 1 mL. Cells were incubated for 40 minutes at 37°C/5% $CO_2$ with DNA/Lipofectamine complexes, and after that the culture medium was completely removed and replaced with a pre-warmed neuronal medium.

## MscL-v.1 and MscL-v.2 constructs

*pAAV-hSyn1-MscL-eGFP-v.1 construct*. The MscL cDNAs, kindly provided by Prof. Boris Martinac (Victor Chang Cardiac Research Institute, Darlinghurst, Australia). The MscL cDNAs were excised from pTRE-Tight (Clontech) source plasmid and sub-cloned in-frame into pAAV3_hSyn1_eGFP construct through the SalI and BamHI restriction sites, between the promoter sequence (synapsin 1) and the fluorescence tag (eGFP). The digested vector plasmid and the MscL insert were ligated overnight at 16°C with the T4 ligase enzyme, using a vector to insert molar ratio of 1 to 3. *pAAV-hSyn1-MscL-tdTomato-v.2 construct*. In order to get a more specific membrane targeting of MscL channel, a second generation of the construct was built by adding at the C-terminal of our construct sequence the

Kir2.1 endoplasmic reticulum export signal (ERexp) as previously described (Gradinaru et al., 2010). To achieve this, the ERexp single strand oligoes were synthetized with an additional BsrGI restriction site at 5' and a HindIII restriction site at 3', annealed together, amplified by PCR and then cut by enzymatic digestion. After having also digested the pAAV3_hSyn1_MscL_eGFP v.1 vector with the same restriction enzymes, the two sequences were ligated together for 1 hour at room temperature (RT). Then, the eGFP protein was replaced with a tdTomato protein, known for having a brighter fluorescence signal. We amplified by PCR the tdTomato sequence from a pCAGGS_IRES_tdTomato vector through a forward primer carrying a BamHI restriction site and a reverse primer carrying a BsrGI site. The amplified DNA and the pAAV3_hSyn1_MscL_eGFP v.2 vector were digested with BamHI and BsrGI and ligated together overnight at 16°C. Starting from the section "4. Electrophysiological characterization of the engineered MscL channel", we refer to the pAAV-hSyn1-MscL-tdTomato-v.2 as engineered-MscL (eMscL).

*Bacteria transformation.* For each construct, Stbl3 competent cells were transformed with 5 µL of ligation reaction through a standard heating shock protocol (30 minutes on ice and then heat shock at 42°C) and plated onto LB agar plate containing the ampicillin antibiotic for clone selection. After an overnight incubation at 37°C, isolated colonies were analyzed by restriction analysis and then sequencing.

All the enzymes used for this project belonged to Promega and New England Biolabs (NEB).

## Patch-clamp recordings and pressure-clamp system

Primary cortical neurons were plated at a density of 400 cells·mm$^{-2}$ onto 18 mm glass coverslip and the voltage-clamp recordings were performed in the patch clamp cell-attached configuration between 14 and 20 DIV.

Borosilicate glass capillary (OD/ID 1.50 mm/0.86 mm, KF Technology) were pulled using an horizontal puller (P1000, Sutter Instruments) with a resistance in the range of 8 and 10 MOhms, to generate a glass pipette.

The cell-attached experiments were performed applying a command potential of +30 mV and, assuming a resting potential of -70 mV, the estimated applied potential would be -100 mV. Current traces were inverted according to common convention for cell-attached recordings. The bath solution contained 140 mM NaCl, 3 mM KCl, 1 mM $MgCl_2$, 1 mM $CaCl_2$ and 10 mM HEPES (pH 7.2); the pipette solution contained 140 mM NaCl, 0.5 $CaCl_2$, 2 mM EGTA and 10 mM HEPES (pH 7.2). EGTA was added for buffering free $Ca^{2+}$. The eMscL-induced currents were amplified through the Multiclamp 700B amplifier (Axon Instruments), and then digitized and recorded with the Digidata 1200A (Axon Instruments) acquisition board. The output current signals were sampled at 25 kHz and filtered using a low-pass filter frequency of 10 kHz.

In order to apply a calibrated negative pressure during the voltage-clamp recording, the setup was equipped with a custom-made pressure sensor system. It comprised a silicon piezo resistive pressure sensor (model MPDX2200DP, Freescale), which generated a linear voltage output directly proportional to the pressure applied in the tubing connected to the patch pipette. The pressure sensor system was connected to a custom-made conditioning circuit and acquired through the Multiclamp 700B amplifier (Molecular Devices). The active conditioning circuit performed amplification, balancing, level shifting and offset compensation of the differential output (temperature and drift compensation) of the pressure sensor, and it was based on a double stage operational amplifier circuitry with onboard offset and gain controls. The output voltage to pressure conversion factor of the overall pressure sensor system was calibrated with a pipette perfusion instrument (2PK+, ALA Scientific Instruments), which was used to apply well-defined negative pressures (in mmHg) to the tubing connected to the patch pipette. During the experiments, the pressure in the

tubing was manually applied through a 5 mL luer-lock syringe, and monitored in real time through the pCLAMP 10 software (Molecular Devices).

Data acquisition and analysis were all controlled using the pCLAMP 10 software package. The pressure activation threshold was determined by observing at which pressure the first evoked-current or a relevant change in the trace slope occurred. Data were filtered with low-pass Bessel filter before the analysis.

To verify that the recorded spikes were indeed action potentials, we added 1 μM TTX (Tocris Bioscience) to the bath solution and incubated for 5 minutes to block $Na^+$ channels, before applying the negative pressure through the patch pipette.

## Estimating the applied membrane tension

Since the lack of a highly resolved image of the membrane dome into the pipette patch, we estimated the tension elicited along the plasma membrane upon the mechanical stimulation by applying an equation based on the Laplace's law previously reported in literature (Ursell et al., 2011).

The membrane tension ($\tau$) was estimated using the equation $\tau = \gamma + (r \cdot P)/2$, where r is the radius of pipette tip (approximately 1 μm) and P is the applied negative pressures in terms of $mN \cdot m^{-2}$.

## Immunostaining and image analysis

For co-localization and morphological analyses, neuronal cells were fixed at 15 DIV, and for immunostaining with synaptic markers, cells were fixed at 18-20 DIV.

Neurons were fixed in 4% cold paraformaldehyde (PFA, Sigma-Aldrich) in standard phosphate-buffered saline (PBS, Sigma-Aldrich) for 15 minutes at RT, washed twice in 1X tris-buffered saline (TBS) and mounted with ProLong Diamond Antifade mountant (Invitrogen).

For immunostaining, after the fixation protocols was completed cells were permeabilized with 0.1% Triton X-100 (Sigma-Aldrich) in 1X TBS for 5 minutes at

RT, and then blocked with 3% bovine serum albumin (BSA, Sigma-Aldrich) in 1X TBS for 1 hour at RT.

Immunostaining was performed by incubating the primary antibody overnight at 4°C and, after few washing steps in 1X TBS, incubating the secondary antibody for 1 hour at RT. During the labelling with secondary antibodies, cells were covered with a silver foil to preserve the sample from light. Primary antibodies were: guinea pig anti-VGLUT1 (135304, SYSY), rabbit anti-VGAT (131013, SYSY), and neuronal class III beta-tubulin antibody (MMS-435P, Covance) diluted respectively 1:500, 1:1000 and 1:250. Secondary antibodies were: Alexa Fluor 488 goat anti-guinea pig IgG (A11073, Life Technologies), and Alexa Fluor 568 goat anti-rabbit IgG (A11036, Life Technologies). All secondary antibodies were diluted 1:1000. Primary and secondary antibodies were diluted in 3% BSA in 1X TBS.

Images were acquired on a Leica SP8 confocal microscope (Leica Microsystems) and analyzed with ImageJ software (Schindelin et al., 2015), except where otherwise specified.

For neuronal morphology analysis, images were acquired on the DeltaVision Elite microscope (GE Healthcare Life Sciences) using a 20X air objective (PLN 20X/0.4, Olympus). The analysis was performed by running the morphology quantification software NeurphologyJ, an ImageJ plugin, as described in Ho et al., 2011 (Ho et al., 2011).

Co-localization analysis was performed by using the Coloc2 Image plugin, by following the described procedure (Costes et al., 2004).

Viability plot was calculated as mean of the percentage of live cells divided by the total number of cells for field of view, as described in Palazzolo et al., 2017 (Palazzolo et al., 2017). The apoptotic cells, which are characterized by pyknotic nuclei, were identified by their morphology and counted.

## Adeno associated virus production

AAV-eMscL particles production was performed in 15-cm culture dishes by using a total amount of $25x10^6$ HEK293T cells ($5x10^6$ per dish). The transfections were carried out at 70% confluence by using a standard calcium phosphate-based protocol. The transfected DNAs consisted of a 1:1:1 ratio mixture of AAV vector plasmid, AAV serotype 1 and 2 packaging proteins (pRV1 and pH21), and adenoviral helper (pFdelta6). Seventy-two hours after transfection cells were harvested and AAV particles were extracted by subjecting the cell pellet to three consecutive freeze-thaw cycles and purified through a heparin column (Hitrap Heparin, GE Healthcare).

## Calcium imaging and data analysis

The primary neuronal cultures were infected with a recombinant adeno associated virus (hybrid serotype 1 and 2) encoding the G22S eMscL ion channel. Primary cultures were infected at 15 DIV by incubating overnight 1:1000 dilution of the virus stock solution. After incubation, the culture medium was half replaced with a fresh one.

The infected cell cultures showed a good level of protein expression together with a significant calcium activity starting from 5 days post infection. Calcium imaging experiments were assayed between 20 and 25 DIV, after loading the cell cultures with Fluo-4 AM calcium dye (Invitrogen) for 20 minutes.

Calcium imaging was performed by using a custom inverted fluorescence microscope which has been integrated with a miniaturized cell incubator. The time-lapse calcium imaging was performed at a frame rate of 65 Hz through a 10X air objective (NA 0.25, Olympus), 2x2 binning, and EM gain of 120. The acquired time lapse imaging series (t-stack series) were analyzed with a custom written algorithm in Matlab, which have been previously described (Palazzolo et al., 2017).

Briefly, the algorithm computed the standard deviation projection of the t-stack and the non-homogeneous background in the projection image was estimated through a morphological opening operation with a disk of arbitrary size (smaller than the typical dimension of the cell soma), and then subtracted. Successively, the projection image was binarized, and the ROIs were detected. The fluorescence calcium traces of the neurons were then extracted from the t-stack by computing the mean fluorescence intensity value within the ROIs previously identified. Subsequently, the raw traces of the neurons were baseline corrected and normalized, to calculate the normalized fluorescent calcium signals indicated as $\Delta F/F_0$ (F fluorescence intensity in arbitrary units). The baseline $F_0$ of the traces was automatically estimated with a linear diffusion filter, which evaluates only the slow varying component of the trace by setting a large time window (time window length= 30 s). The normalized traces were then smoothed with the modified Perona-Malik filter (Palazzolo et al., 2017).

On the smoothed traces, calcium events were automatically detected by imposing the following conditions: (i) the first derivative in a right interval of the onset overcomes a fixed positive threshold ($10^{-3}$ in case of asynchronous activity, $10^{-2}$ in case of synchronous activity); (ii) the $\Delta F$ between the onset and the offset of an event overcomes a threshold defined as the standard deviation of the difference between the original and the smoothed trace; (iii) the first derivative in a right interval of the event offset is lower than a fixed negative threshold ($-10^{-4}$); and (iv) the time interval between the last time point after the onset with first derivative higher than a fixed threshold and the offset did not reach a fixed width (300 time points).

## Wide-field fluorescence microscope

The light sources of the optical setup were two LEDs (M470L3 and M565L3 equipped with two LEDD1B controllers, Thorlabs). One LED emitted at a wavelength of 488 nm to excite the fluorescent calcium sensor used to perform

calcium imaging, and the other emitted at 565 nm to excite red emitting fluorescent tags used to discriminate chemically treated or genetically modified cells within the field of view. The light beams from the two LEDs were combined through a dichroic mirror DM1 (LM01-480 - Semrock, Optoprim), and then collimated with a lens L1 (30 mm focal length VIS doublets, Thorlabs). The interchangeable dichroic mirror reflected the light towards the pupil of the microscope objective (10X air objective Olympus, Thorlabs). Two distinct dichroic mirrors were used to either perform calcium imaging (FF495-DI02 – Semrock, Optoprim) or to detect the cells (FF560-DI02 – Semrock, Optoprim). The fluorescence emission light from the sample was collected through the microscope objective, conveyed through the dichroic mirror, and focused on the CCD camera by the tube lens TL (150 mm focal length VIS doublets, Thorlabs). An interchangeable emission filter F3 (F530/43 and F624/40 – Semrock, Optoprim) was positioned in front of the CCD camera (EM-CCD Andor Camera Ixon DU897 - Andor Technology). Time-lapse calcium imaging was performed with the following settings: 2x2 binning (pixel size equal to 3.75 μm), EM gain of 120, and frame rate of 20 Hz. The CCD generated a TTL synchronization signal indicating the time exposure of each consecutive, acquired image frame.

## Ultrasound delivery system

The US delivery system was designed in order to avoid or minimize unwanted and uncalibrated mechanical stress on the cells, and thus allow performing experiments in a water tank-free setup. The water tank-free configuration allow to deliver a relatively uniform pressure field wide area on the cell culture (i.e. with a radius of ~2.5 mm) at a fixed distance from the ultrasound source, thus facilitating the integration of the fluorescence imaging system with the US devices. The propagation probe was designed using CAD 3D Autodesk Inventor (Autodesk Inc.) and fabricated in stainless steel using a metal 3D printer.

The ultrasound compatible cell chamber was designed using CAD 3D Autodesk Inventor (Autodesk Inc.) and fabricated in Tango polymer via 3D printing process. The chamber was designed consisting of three main components: a circular base plate (36 mm diameter, 9 mm thick) with a cell coverslip lodging at the center (18 mm diameter); a cap disk (OD 38 mm, ID mm, 10 mm thick); a polydimethylsiloxane (PDMS Sylgard 184, Corning) lid. Degassed PDMS was directly poured into the cap disk and a plastic pillar base was placed at its bottom face in order to obtain the desired lid thickness (Figure 29). The PDMS lid was made by mixing the curing agent and the silicon monomer at ratio of 1:10 w/w, and then baking the degassed mixture overnight at 40°C. Lids of different thicknesses were tested. The choice to use the PDMS for fabricating the chamber lid is due to its intrinsically properties such as optical transparency (Whitesides, 2006), low ultrasound attenuation at our final US frequency (Carugo et al., 2015), permeability to gases (Zanzotto et al., 2004), and ease of molding (Kim et al., 1995).

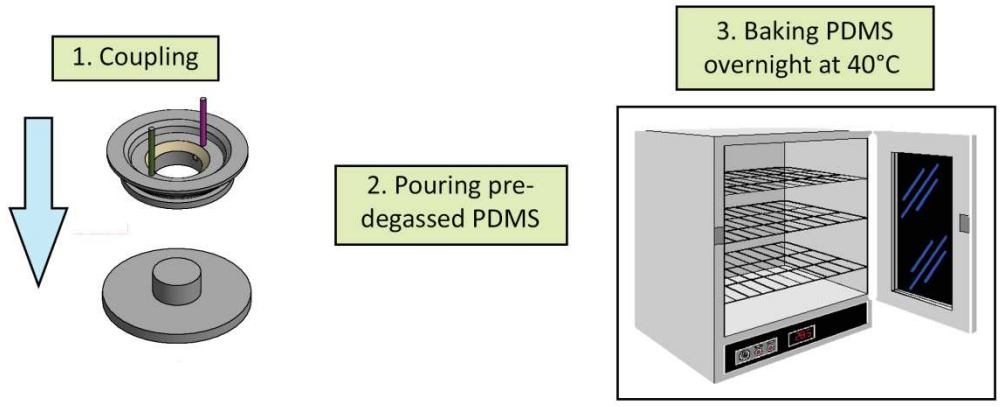


**Figure 29 | PDMS lid fabrication**
After coupling the cap disk on the pillar base, the PDMS mixture was poured in, and then baked overnight at 40°C.

The US delivery system is based on an immersion-type ultrasonic transducer (GS350-D19 model, The Ultran Group). The driving electronics of the US transducer were configured so as to define the acoustic stimulation parameters, which included US pulse repetition frequency, tone burst frequency, number of

tone bursts per stimulus, and number of acoustic cycles per tone burst. These parameters can be varied in order to apply distinct US stimulation protocols. As illustrated in Figure 23, a D/A USB-board (element 1 in the green box - PCI-6529, National Instruments) monitored and recorded a TTL trigger signal coming from the CCD camera, which increased during the frames acquisition of the time-lapse calcium imaging, and then reduced to a lower level when the frames acquisition stopped. This signal triggered the US stimulation protocol defined in a LabVIEW software interface, developed in-house. The user interface was employed to input the duration of a single US stimulus, which also defined the number of tone bursts per stimulus, and the time interval between consecutive stimuli. In order to synchronize the calcium imaging with the US stimulation, the software generated and recorded an output trigger signal. We set an US stimulus of 1 second (US on) followed by 4 seconds intervals in which the US was deactivated, corresponding to a stimulus repetition frequency of 0.2 Hz. This mode of stimulation was repeated for the overall duration of the time-lapse calcium imaging, and acted as enabling signal of the tone burst wave generator (AFG3021B, Tektronix).

Indeed, this first wave generator (element 2 in the green box of Figure 23) allowed defining the repetition frequency of the tone bursts, within a single US stimulation, and at the same time it represented the triggering signal for a second wave generator (DG1022A, Rigol Technology Inc.). The output signal of the tone burst wave generator was configured to a square wave with amplitude of 0-5 V and duty cycle of 50%. The output signal of the second wave generator (element 3 in the green box of Figure 23) was set to a sinusoidal wave with peak-to-peak voltage ($V_{PP}$) of 5.8 V and frequency of 380 kHz. The number of cycles of each triggered sinusoidal output was also set, which defined the duration of each US tone burst within the US stimulus. Each tone burst was triggered by a positive edge detected in the square wave output of the first wave generator. The output of the second generator was then conveyed to a custom built amplifier (element 4

in the green box of Figure 23). In the Table 2, the US settings tested during the stimulation of the neuronal networks are reported.

| PRF | tbf | c/tb | output voltages |
|---|---|---|---|
| **0.2 Hz** | 10 Hz | 10 – 200 cyc | 200 – 250 $V_{pp}$ |
| **0.2 Hz** | 20 Hz | 10 – 200 cyc | 200 – 250 $V_{pp}$ |
| **0.2 Hz** | 50 Hz | 10 – 200 cyc | 200 – 250 $V_{pp}$ |
| **0.2 Hz** | 100 Hz | 10 – 200 cyc | 200 – 250 $V_{pp}$ |

**Table 2 | Ultrasound stimulation protocols tested**

We opted to develop a custom built amplifier due to the loss capacitive nature of the piezoelectric transducer and the fixed working frequency of the US wave. Notably, the reactive electrical load of the transducer doesn't require a large amount of power but rather a system able to supply large voltages (>200 $V_{pp}$) into reactive loads. For the specific case of a system working at a fixed US frequency, the amplifier can be conceived as a high efficiency class-B power stage tuned to the US frequency. An IC driver (International Rectifier IR2112 – RS components) ensured optimum driving of the two Mosfet power devices, which generated output voltages of 200-250 $V_{pp}$ through a step-up wound toroidal transformer. Careful design of the output transformer and its inductance, together with the self-capacitance of the output cable and the US transducer, resulted in a system's efficiency >75%. The output power of the amplifier could be tuned through the voltage of the external power supply in the range 12.6 to 17.0 $V_{DC}$.

Finally, the amplified signal was sent to the US transducer producing the pulsed US wave. All the trigger signals described in this section, together with the TTL signal coming from the CCD, were simultaneously recorded through the D/A USB-board, in order to align the US stimulation protocol with the frames of the time-lapse calcium imaging during post-processing.

## Calibration of the acoustic field

The acoustic pressure field was characterized using a needle hydrophone (200 μm diameter needle, Precision Acoustics), with the ultrasound delivery system (US condenser and cell chamber) submerged in a tank filled with filtered and degassed water. During the calibration experiments, the water temperature was monitored with a glass thermometer, in order to calculate sound speed for use in estimating hydrophone position. The needle hydrophone was positioned at the desired distance through an automated position-control software (UMS2, Precision Acoustics) and the drive voltage (PP007-WR, LeCroy) and current (4100, Pearson Electronics) probes were monitored to ensure proper system operation, and allow subsequent calculation of electrical impedance. Calibration data were processed in MATLAB using the following steps: (i) application of a high pass filter to remove any DC offset in the data traces, (ii) calculation of hydrophone $A_{(f,x,y,z)}$ and drive voltage $V_{(f)}$ Fourier transforms, and (iii) calculation of the transmitting voltage response at each frequency and scan grid point (x,y,z): $TVR_{(f,x,y,z)} = A_{(f,x,y,z)}/(V_{(f)}S_{(f)})$ where $S_{(f)}$ is the hydrophone sensitivity. Four types of calibration tests were performed in this study: (1) frequency-dependence of the acoustic peak pressure in the target plane, to select an optimal frequency for operation of the ultrasound stimulation system; (2) voltage-dependence of the acoustic peak pressure in the target plane at the optimal frequency, to identify a range of acoustic pressure amplitudes suitable for neuronal stimulation; (3) axial scan of the peak pressure at the optimal US frequency and the maximum driving voltage, to evaluate the sensitivity of the system to variations in the distance between the US source and the target plane; and (4) planar scan of the acoustic pressure in the target plane at the optimal US frequency, to spatially characterize the properties of the ultrasound field to which cells and microbubbles are exposed.

## Fluid dynamic characterization of the cell culture chamber

A three-dimensional numerical model was developed to evaluate the fluid dynamics within the cell chamber as already reported in literature (Carugo et al., 2015). We employed this approach to verify that: (i) the wall shear stress at the bottom surface of the chamber was not large enough to impart cell damage, and (ii) regions of potential entrapment for air filled microbubbles (i.e. vortices) were not present. ICEM CFD 14.0 (Ansys) was employed for construction and meshing of the model geometry. The geometry was meshed using tetrahedral cells. The maximum mesh element size was set at 0.05 mm at the inlet and outlet boundaries, and 0.5 mm at the wall boundaries.

Mass flow rate and zero-pressure boundary conditions were imposed at the inlet and outlet surfaces, respectively. A no-slip flow boundary condition was imposed on the other surfaces. The volumetric flow rate at the inlet was varied in the range 1 to 10 $mL \cdot min^{-1}$ to simulate practical injection procedures.

## Production of positive charged lipid-coated microbubbles

Air-filled lipid-coated microbubbles were used as an ultrasound-responsive agent to amplify the mechanical effects of ultrasound alone. Microbubbles were designed to have a net positive charge, thus ensure binding, and spatial proximity to the target cells.

The microbubble were made of 1,2-distearoyl-sn-glycero-3-phosphocholine (DSPC) and 1,2-distearoyl-sn-glycero-3-ethyl phosphocholine (DSEPC, Avanti Polar Lipids) and Polyoxyethylene (40) stearate (PEG40s, Sigma–Aldrich). The compounds were dissolved in chloroform at a concentration of 25 $mg \cdot mL^{-1}$ for DSPC and 10 $mg \cdot mL^{-1}$ for DSEPC and PEG40s, and then mixed in a 10 mL glass vial at a molar ratio of 100:15:10. This mixture was left overnight in a fume hood at RT, to let chloroform evaporate. The resulting dry lipid film was suspended in 3 mL filtered PBS, and placed on a hotplate set at 95°C for 30 min, under constant stirring. Then the air within the vial was substituted with nitrogen gas and the

solution sonicated for 180 seconds at 10W to disperse the lipids using an 20 kHz ultrasonic cell disruptor (Ultrasonic Sonifier 150, Branson Ultrasonics), with the tip of the sonicator fully immersed in the liquid. The suspension was subsequently sonicated at the gas–water interface for 30 seconds at 35W to produce gas-encapsulating microbubbles. Lipid-coated microbubbles were examined via bright field microscopy (Nikon Eclipse E100) to determine their size distribution and stability over time. Microbubbles sizing was performed using the Analyse Particles plugin in ImageJ (NIH). Images of microbubbles were also acquired using the optics integrated with the US delivery system, in order to assess microbubble binding to the cell surface and the cell chamber's substrate.

## Data analysis and statistics

Statistical analysis, graphs and plots were generated using GraphPad Prism 6 (GraphPad Software) and MATLAB 2016b (MathWorks). To verify if our data sets were reflecting a normal distribution, the Shapiro-Wilk normality test was carried out. Since the normality distribution was not fulfilled, the statistical significance analysis was performed using the nonparametric two-sided Mann-Whitney test ($p= 0.05$) and data set given as mean ± SEM.

# 9. PUBLICATION LIST

Journal of Cell Science pii: jcs.210393 (2018) - doi: 10.1242/jcs.210393

**Mechano-sensitization of mammalian neuronal networks through expression of the bacterial exclusively-mechanosensitive MscL channel**

Soloperto A.*, Boccaccio A., Contestabile A., Moroni M., Hallinan G., Palazzolo G., Chad J., Deinhardt K., Carugo D. & Difato F.

* First author

## Abstract

Development of remote stimulation techniques for neuronal tissues represents a challenging goal. Among the potential methods, mechanical stimuli are the most promising vector to convey information non-invasively into intact brain tissue. In this context, selective mechano-sensitization of neuronal circuits would pave the way to develop a new cell-type specific stimulation approach. We report here for the first time the development and characterization of mechano-sensitized neuronal networks through the heterologous expression of an engineered bacterial large conductance mechanosensitive ion channel (MscL). The neuronal functional expression of the MscL channel was validated through patch-clamp recordings upon application of calibrated suction pressures. Moreover, we verified the effective development of *in-vitro* neuronal networks expressing the engineered MscL channel in terms of cell survival, number of synaptic puncta, and spontaneous network activity. The exclusively mechanosensitivity of the engineered MscL channel, with its wide genetic modification library, may represent a versatile tool to further develop a mechano-genetic approach.

Scientific Reports 7, Article number: 8499 (2017) - doi: 10.1038/s41598-017-08979-8

**Fast wide-volume functional imaging of engineered *in-vitro* brain tissues**

Palazzolo G.*, Moroni M.*, Soloperto A., Aletti G., Naldi G., Vassalli M., Nieus T. & Difato F.

* First author

## Abstract

The need for *in-vitro* models that mimic the human brain to replace animal testing and allow high-throughput screening has driven scientists to develop new tools that reproduce tissue-like features on a chip. Three-dimensional (3D) *in-vitro* cultures are emerging as an unmatched platform that preserves the complexity of cell-to-cell connections within a tissue, improves cell survival, and boosts neuronal differentiation. In this context, new and flexible imaging approaches are required to monitor the functional states of 3D networks. Herein, we propose an experimental model based on 3D neuronal networks in an alginate hydrogel, a tunable wide-volume imaging approach, and an efficient denoising algorithm to resolve, down to single cell resolution, the 3D activity of hundreds of neurons expressing the calcium sensor GCaMP6s. Furthermore, we implemented a 3D co-culture system mimicking the contiguous interfaces of distinct brain tissues such as the cortical-hippocampal interface. The analysis of the network activity of single and layered neuronal co-cultures revealed cell-type-specific activities and an organization of neuronal subpopulations that changed in the two culture configurations. Overall, our experimental platform represents a simple, powerful and cost-effective platform for developing and monitoring living 3D layered brain tissue on chip structures with high resolution and high-throughput.

Molecules 21(8), 1018 (2016) - doi: 10.3390/molecules21081018

**Modulation of Neural Network Activity through Single Cell Ablation: An in-Vitro Model of Minimally Invasive Neurosurgery**

Soloperto A.*, Bisio M.*, Palazzolo G., Chiappalone M., Bonifazi P. & Difato F.

* First author

## Abstract

The technological advancement of optical approaches, and the growth of their applications in neuroscience, has allowed investigations of the physio-pathology of neural networks at a single cell level. Therefore, better understanding the role of single neurons in the onset and progression of neurodegenerative conditions has resulted in a strong demand for surgical tools operating with single cell resolution. Optical systems already provide subcellular resolution to monitor and manipulate living tissues, and thus allow understanding the potentiality of surgery actuated at single cell level. In the present work, we report an *in-vitro* experimental model of minimally invasive surgery applied on neuronal cultures expressing a genetically encoded calcium sensor. The experimental protocol entails the continuous monitoring of the network activity before and after the ablation of a single neuron, to provide a robust evaluation of the induced changes in the network activity. We report that in subpopulations of about 1000 neurons, even the ablation of a single unit produces a reduction of the overall network activity. The reported protocol represents a simple and cost effective model to study the efficacy of single-cell surgery, and it could represent a test-bed to study surgical procedures circumventing the abrupt and complete tissue removal in pathological conditions.

Frontiers in Neuroscience 10: 101 (2016) - doi: 10.3389/fnins.2016.00101

**Laser Nano-Neurosurgery from Gentle Manipulation to Nano-Incision of Neuronal Cells and Scaffolds: An Advanced Neurotechnology Tool**

Soloperto A.*, Palazzolo G.*, Tsushima H., Chieregatti E., Vassalli M. & Difato F.
* First author

## Abstract

Current optical approaches are progressing far beyond the scope of monitoring the structure and function of living matter, and they are becoming widely recognized as extremely precise, minimally-invasive, contact-free handling tools. Laser manipulation of living tissues, single cells, or even single-molecules is becoming a well-established methodology, thus founding the onset of new experimental paradigms and research fields. Indeed, a tightly focused pulsed laser source permits complex tasks such as developing engineered bioscaffolds, applying calibrated forces, transfecting, stimulating, or even ablating single cells with subcellular precision, and operating intracellular surgical protocols at the level of single organelles. In the present review, we report the state of the art of laser manipulation in neuroscience, to inspire future applications of light-assisted tools in nano-neurosurgery.

# 10. PATENT LIST

Patent issued (2016) – Application number: IT 102016000097811

**Tunable Extended Depth Of Field Microscopy**

Inventors: Difato F., Moroni M., Palazzolo G., Soloperto A.

## Summary statement

We present a novel optical microscope architecture which provides an inertia-free axial scanning of the sample, which could be used to acquire a z-stack of the sample or to extend the depth of field of the microscope. The extension of the depth of field can be arbitrarily chosen by controlling the extension of the fast axial scanning of the sample.

Patent issued (2015) – Application number: IT 102015000088892

**Combined Laser ablation and Optical propulsion for efficient cell opto-injection and transfection**

Inventors: Difato F., Soloperto A., Palazzolo G.

## Summary statement

We present a method of cell injection and transfection that combines the laser ablation effect and the optical forces, through the axial shift of the laser focus spot. This innovative combination produces concomitant cell membrane poration and optically addressed fluid flow. The two laser-induced effects, generated by the same laser light source, are intrinsically synchronized and targeted with subcellular precision on the same target. The method comprises a first step of setting the x, y coordinates of the focus spot on the desired cell region to target; a second step consisting of the setting of the laser parameters for the following movement of the focus spot along the axial direction. Finally the laser spot is moved forward and backward, thus combining laser ablation and optical tweezing. This procedure can be automated and repeated a desired number of times to improve optoinjection efficiency.

## 11. ORAL CONTRIBUTION LIST

Invited Talk (2017) – Rome, Italy
**The genetically mechano-sensitized neuronal network as a model for developing the mechanogenetic approach**

5th Future investigators in Regenerative Medicine (2017) – Girona, Spain
**Engineering mechanobiology: the bacterial MscL channel as a future tool for neuronal stimulation technology**

Southampton Neuroscience Group Seminar (2016) – Southampton, United Kingdom
**Mammalian expression of the mechanosensitive channel MscL: a step forward in the sonogenetic paradigm**

## 12. POSTER PRESENTATION LIST

5th Future investigators in Regenerative Medicine (2017) – Girona, Spain
**Engineering mechanobiology: the bacterial purely mechanosensitive ion channel MscL as a future tool for neuronal stimulation technology**
Soloperto A.*, Moroni M., Palazzolo G., Boccaccio A., Contestabile A., Pruzzo G., Gray M., Hallinan G., Patel P., Chad J., Deinhardt K., Carugo D. & Difato F.
* Presenting author

60th Biophysical Society Annual Meeting (2016) - Los Angeles, CA, USA
**Expression and biophysical characterization of bacterial mechanosensitive ion channel of large conductance into mammalian cells**
Soloperto A.*, Bartolozzi A., Palazzolo, G., Basso M., Contestabile A., Vassalli M. & Difato F.
* Presenting author

10th European Biophysics Congress (2015) – Dresden, Germany
**Efficient single neuron opto-transfection with a sub-nanosecond UVA pulsed laser**
Soloperto A.*, Palazzolo G. & Difato F.
* Presenting author

# REFERENCES


**Akinlaja, J. and Sachs, F.** (1998). The Breakdown of Cell Membranes by Electrical and Mechanical Stress. *Biophys. J.* **75**, 247–254.

**Albuisson, J., Murthy, S. E., Bandell, M., Coste, B., Louis-dit-Picard, H., Mathur, J., Fénéant-Thibault, M., Tertian, G., de Jaureguiberry, J.-P., Syfuss, P.-Y., et al.** (2013). Dehydrated hereditary stomatocytosis linked to gain-of-function mutations in mechanically activated PIEZO1 ion channels. *Nat. Commun.* **4**,.

**Anava, S., Greenbaum, A., Jacob, E. Ben, Hanein, Y. and Ayali, A.** (2009). The regulative role of neurite mechanical tension in network development. *Biophys. J.* **96**, 1661–1670.

**Andersen, O. S. and Koeppe, R. E.** (2007). Bilayer Thickness and Membrane Protein Function: An Energetic Perspective. *Annu. Rev. Biophys. Biomol. Struct.* **36**, 107–130.

**Armbruster, B. N., Li, X., Pausch, M. H., Herlitze, S. and Roth, B. L.** (2007). Evolving the lock to fit the key to create a family of G protein-coupled receptors potently activated by an inert ligand. *Proc. Natl. Acad. Sci.* **104**, 5163–5168.

**Árnadóttir, J. and Chalfie, M.** (2010). Eukaryotic Mechanosensitive Channels. *Annu. Rev. Biophys.* **39**, 111–137.

**Bae, C., Gnanasambandam, R., Nicolai, C., Sachs, F. and Gottlieb, P. A.** (2013). Xerocytosis is caused by mutations that alter the kinetics of the mechanosensitive channel PIEZO1. *Proc. Natl. Acad. Sci.* **110**, E1162–E1168.

**Bae, C., Sachs, F. and Gottlieb, P. A.** (2015). Protonation of the human PIEZO1 ion channel stabilizes inactivation. *J. Biol. Chem.* **290**, 5167–5173.

**Bailey, M. R., Khokhlova, V. A., Sapozhnikov, O. A., Kargl, S. G. and Crum, L. a.** (2003). Physical mechanisms of the therapeutic effect of ultrasound (a review). *Acoust. Phys.* **49**, 369–388.

**Barnes, J. M., Przybyla, L. and Weaver, V. M.** (2017). Tissue mechanics regulate brain development, homeostasis and disease. *J. Cell Sci.* **130**, 71–82.

**Bavi, N., Cortes, D. M., Cox, C. D., Rohde, P. R., Liu, W., Deitmer, J. W., Bavi, O., Strop, P., Hill, A. P., Rees, D., et al.** (2016). The role of MscL amphipathic N terminus indicates a blueprint for bilayer-mediated gating of mechanosensitive channels. *Nat. Commun.* **7**, 11984.

**Beltramo, R., D'Urso, G., Maschio, M. D., Farisello, P., Bovetti, S., Clovis, Y., Lassi, G., Tucci, V., De Pietri Tonelli, D. and Fellin, T.** (2013). Layer-specific excitatory circuits differentially control recurrent network dynamics in the neocortex. *Nat. Med.* **16**, 1–10.

**Bernick, K. B., Prevost, T. P., Suresh, S. and Socrate, S.** (2011). Biomechanics of single cortical neurons. *Acta Biomater.* **7**, 1210–1219.

**Berrier, C., Park, K. H., Abes, S., Bibonne, A., Betton, J. M. and Ghazi, A.** (2004). Cell-free synthesis of a functional ion channel in the absence of a membrane and in the presence of detergent. *Biochemistry* **43**, 12585–12591.

**Betanzos, M., Chiang, C.-S., Guy, H. R. and Sukharev, S.** (2002). A large iris-like expansion of a mechanosensitive channel protein induced by membrane tension. *Nat. Struct. Biol.* **9**, 704–710.

**Betz, T., Koch, D., Lu, Y.-B., Franze, K. and Kas, J. A.** (2011). Growth cones as soft and weak force generators. *Proc. Natl. Acad. Sci.* **108**, 13420–13425.

**Bezanilla, F. and Perozo, E.** (2002). Force and Voltage Sensors in One Structure. *Science (80-. ).* **298**, 1562–1563.

**Bialecka-Fornal, M., Lee, H. J., DeBerg, H. A., Gandhi, C. S. and Phillips, R.** (2012).

Single-cell census of mechanosensitive channels in living bacteria. *PLoS One* **7**,.

**Bioeffects Committee, A. I. of U. in M.** (2008). *American Institute of Ultrasound in Medicine Consensus Report on Potential Bioeffects of Diagnostic Ultrasound*.

**Birkner, J. P., Poolman, B. and Kocer, A.** (2012). Hydrophobic gating of mechanosensitive channel of large conductance evidenced by single-subunit resolution. *Proc. Natl. Acad. Sci. U. S. A.* **109**, 12944–9.

**Blount, P., Sukharev, S. I., Moe, P. C., Nagle, S. K. and Kung, C.** (1996). Towards an understanding of the structural and functional properties of MscL, a mechanosensitive channel in bacteria. *Biol. Cell* **87**, 1–8.

**Boer, M., Anishkin, A. and Sukharev, S.** (2011). Adaptive MscS Gating in the Osmotic Permeability Response in E. coli: The Question of Time. *Biochemistry* **50**, 4087–4096.

**Booth, I. R.** (2014). Bacterial mechanosensitive channels: progress towards an understanding of their roles in cell physiology. *Curr. Opin. Microbiol.* **18**, 16–22.

**Booth, I. R. and Blount, P.** (2012). The MscS and MscL Families of Mechanosensitive Channels Act as Microbial Emergency Release Valves. *J. Bacteriol.* **194**, 4802–4809.

**Brangwynne, C. P., MacKintosh, F. C., Kumar, S., Geisse, N. A., Talbot, J., Mahadevan, L., Parker, K. K., Ingber, D. E. and Weitz, D. A.** (2006a). Microtubules can bear enhanced compressive loads in living cells because of lateral reinforcement. *J. Cell Biol.* **173**, 733–741.

**Brangwynne, C. P., MacKintosh, F. C., Kumar, S., Geisse, N. A., Talbot, J., Mahadevan, L., Parker, K. K., Ingber, D. E. and Weitz, D. A.** (2006b). Microtubules can bear enhanced compressive loads in living cells because of lateral reinforcement. *J. Cell Biol.* **173**, 733–741.

**Brohawn, S. G.** (2015). How ion channels sense mechanical force: insights from mechanosensitive K2P channels TRAAK, TREK1, and TREK2. *Ann. N. Y. Acad. Sci.* **1352**, 20–32.

**Carstensen, E. L., Gracewski, S. and Dalecki, D.** (2000). The search for cavitation in vivo. *Ultrasound Med. Biol.* **26**, 1377–1385.

**Carugo, D., Owen, J., Crake, C., Lee, J. Y. and Stride, E.** (2015). Biologicallyand acoustically compatible chamber for studying ultrasound-mediated delivery of therapeutic compounds. *Ultrasound Med. Biol.* **41**, 1927–1937.

**Carugo, D., Aron, M., Sezgin, E., Bernardino de la Serna, J., Kuimova, M. K., Eggeling, C. and Stride, E.** (2017a). Modulation of the molecular arrangement in artificial and biological membranes by phospholipid-shelled microbubbles. *Biomaterials* **113**, 105–117.

**Carugo, D., Aron, M., Sezgin, E., Bernardino de la Serna, J., Kuimova, M. K., Eggeling, C. and Stride, E.** (2017b). Modulation of the molecular arrangement in artificial and biological membranes by phospholipid-shelled microbubbles. *Biomaterials* **113**, 105–117.

**Cash, S. S. and Hochberg, L. R.** (2015). The Emergence of Single Neurons in Clinical Neurology. *Neuron* **86**, 79–91.

**Chalfie, M. and Au, M.** (1989). Genetic control of differentiation of the Caenorhabditis elegans touch receptor neurons. *Science* **243**, 1027–33.

**Chang, G., Spencer, R. H., Lee, A. T., Barclay, M. T. and Rees, D. C.** (1998). Structure of the MscL homolog from Mycobacterium tuberculosis: a gated mechanosensitive ion channel. *Science* **282**, 2220–6.

**Chiang, C.-S., Anishkin, A. and Sukharev, S.** (2004). Gating of the Large Mechanosensitive Channel In Situ: Estimation of the Spatial Scale of the Transition

from Channel Population Responses. *Biophys. J.* **86**, 2846–2861.

**Choi, J. B., Lim, S. H., Cho, K. W., Kim, D. H., Jang, D. P. and Kim, I. Y.** (2013). The effect of focused ultrasonic stimulation on the activity of hippocampal neurons in multi-channel electrode. *Int. IEEE/EMBS Conf. Neural Eng. NER* 731–734.

**Christ, A. F., Franze, K., Gautier, H., Moshayedi, P., Fawcett, J., Franklin, R. J. M., Karadottir, R. T. and Guck, J.** (2010). Mechanical difference between white and gray matter in the rat cerebellum measured by scanning force microscopy. *J. Biomech.* **43**, 2986–2992.

**Cingolani, L. A. and Goda, Y.** (2008). Actin in action: the interplay between the actin cytoskeleton and synaptic efficacy. *Nat. Rev. Neurosci.* **9**, 344–356.

**Clayton, D., Shapovalov, G., Maurer, J. a, Dougherty, D. a, Lester, H. a and Kochendoerfer, G. G.** (2004). Total chemical synthesis and electrophysiological characterization of mechanosensitive channels from Escherichia coli and Mycobacterium tuberculosis. *Proc. Natl. Acad. Sci. U. S. A.* **101**, 4764–4769.

**Cohen, M. and Newsome, W.** (2004). What electrical microstimulation has revealed about the neural basis of cognition. *Curr. Opin. Neurobiol.* **14**, 169–177.

**Corey, J. M. and Feldman, E. L.** (2003). Substrate patterning: An emerging technology for the study of neuronal behavior. *Exp. Neurol.* **184**, 89–96.

**Coste, B., Xiao, B., Santos, J. S., Syeda, R., Grandl, J., Spencer, K. S., Kim, S. E., Schmidt, M., Mathur, J., Dubin, A. E., et al.** (2012). Piezo proteins are pore-forming subunits of mechanically activated channels. *Nature* **483**, 176–181.

**Coste, B., Houge, G., Murray, M. F., Stitziel, N., Bandell, M., Giovanni, M. A., Philippakis, A., Hoischen, A., Riemer, G., Steen, U., et al.** (2013). Gain-of-function mutations in the mechanically activated ion channel PIEZO2 cause a subtype of Distal Arthrogryposis. *Proc. Natl. Acad. Sci.* **110**, 4667–4672.

**Costes, S. V, Daelemans, D., Cho, E. H., Dobbin, Z., Pavlakis, G. and Lockett, S.** (2004). Automatic and quantitative measurement of protein-protein colocalization in live cells. *Biophys. J.* **86**, 3993–4003.

**Cox, C. D., Bae, C., Ziegler, L., Hartley, S., Nikolova-Krstevski, V., Rohde, P. R., Ng, C.-A., Sachs, F., Gottlieb, P. A. and Martinac, B.** (2016). Removal of the mechanoprotective influence of the cytoskeleton reveals PIEZO1 is gated by bilayer tension. *Nat. Commun.* **7**, 10366.

**Cox, C. D., Bavi, N. and Martinac, B.** (2017). Origin of the Force. In *Current Topics in Membranes*, pp. 59–96. Elsevier Ltd.

**Cruickshank, C., Minchin, R. F., LeDain, A. C. and Martinac, B.** (1997). Estimate of the pore size of the large mechanosensitive ion channel (MscL) of Escherichia coli. *Biophys. J.* **72**, MPO63-MPO63 ST-Estimate of the pore size of the.

**Dalecki, D.** (2004). Mechanical Bioeffects of Ultrasound. *Annu. Rev. Biomed. Eng.* **6**, 229–248.

**Deffieux, T., Younan, Y., Wattiez, N., Tanter, M., Pouget, P. and Aubry, J.-F.** (2013). Low-Intensity Focused Ultrasound Modulates Monkey Visuomotor Behavior. *Curr. Biol.* **23**, 2430–2433.

**Doerner, J. F., Febvay, S. and Clapham, D. E.** (2012). Controlled delivery of bioactive molecules into live cells using the bacterial mechanosensitive channel MscL. *Nat. Commun.* **3**, 990.

**Dorwart, M. R., Wray, R., Brautigam, C. A., Jiang, Y. and Blount, P.** (2010). S. aureus MscL Is a Pentamer In Vivo but of Variable Stoichiometries In Vitro: Implications for Detergent-Solubilized Membrane Proteins. *PLoS Biol.* **8**, e1000555.

**Douville, N. J., Zamankhan, P., Tung, Y.-C., Li, R., Vaughan, B. L., Tai, C.-F., White, J., Christensen, P. J., Grotberg, J. B. and Takayama, S.** (2011).

Combination of fluid and solid mechanical stresses contribute to cell death and detachment in a microfluidic alveolar model. *Lab Chip* **11**, 609–619.

**Edwards, M. D., Black, S., Rasmussen, T., Rasmussen, A., Stokes, N. R., Stephen, T.-L., Miller, S. and Booth, I. R.** (2012). Characterization of three novel mechanosensitive channel activities in Escherichia coli. *Channels* **6**, 272–281.

**Elkin, B. S.** (2009). Age-Dependent Regional Mechanical Properties of the Rat Hippocampus and Cortex. *J. Biomech. Eng.* **132**, 11010.

**Elkin, B. S., Azeloglu, E. U., Costa, K. D. and Morrison III, B.** (2007). Mechanical Heterogeneity of the Rat Hippocampus Measured by Atomic Force Microscope Indentation. *J. Neurotrauma* **24**, 812–822.

**Engelman, D. M.** (2005). Membranes are more mosaic than fluid. *Nature* **438**, 578–580.

**Essen, D. C. Van** (1997). A tension-based theory of morphogenesis and compact wiring in the central nervous system. *Nature* **385**, 313–318.

**Eyckmans, J., Boudou, T., Yu, X. and Chen, C. S.** (2011). A Hitchhiker's Guide to Mechanobiology. *Dev. Cell* **21**, 35–47.

**Fan, Z., Sun, Y., Di Chen, D., Tay, D., Chen, W., Deng, C. X. and Fu, J.** (2013). Acoustic tweezing cytometry for live-cell subcellular modulation of intracellular cytoskeleton contractility. *Sci. Rep.* **3**, 2176.

**Ferrara, K., Pollard, R. and Borden, M.** (2007). Ultrasound Microbubble Contrast Agents: Fundamentals and Application to Gene and Drug Delivery. *Annu. Rev. Biomed. Eng.* **9**, 415–447.

**Fletcher, D. A. and Mullins, R. D.** (2010). Cell mechanics and the cytoskeleton. *Nature* **463**, 485–492.

**Franze, K., Gerdelmann, J., Weick, M., Betz, T., Pawlizak, S., Lakadamyali, M., Bayer, J., Rillich, K., Gögler, M., Lu, Y. B., et al.** (2009). Neurite branch retraction is caused by a threshold-dependent mechanical impact. *Biophys. J.* **97**, 1883–1890.

**Franze, K., Francke, M., Günter, K., Christ, A. F., Körber, N., Reichenbach, A. and Guck, J.** (2011). Spatial mapping of the mechanical properties of the living retina using scanning force microscopy. *Soft Matter* **7**, 3147.

**Franze, K., Janmey, P. A. and Guck, J.** (2013). Mechanics in Neuronal Development and Repair. *Annu. Rev. Biomed. Eng.* **15**, 227–251.

**Fregni, F. and Pascual-Leone, A.** (2007). Technology insight: noninvasive brain stimulation in neurology-perspectives on the therapeutic potential of rTMS and tDCS. *Nat. Clin. Pract. Neurol.* **3**, 383–393.

**Gefen, A., Gefen, N., Zhu, Q., Raghupathi, R. and Margulies, S. S.** (2003). Age-Dependent Changes in Material Properties of the Brain and Braincase of the Rat. *J. Neurotrauma* **20**, 1163–1177.

**Georges, P. C., Miller, W. J., Meaney, D. F., Sawyer, E. S. and Janmey, P. A.** (2006). Matrices with Compliance Comparable to that of Brain Tissue Select Neuronal over Glial Growth in Mixed Cortical Cultures. *Biophys. J.* **90**, 3012–3018.

**Gottlieb, P. A., Bae, C. and Sachs, F.** (2012). Gating the mechanical channel Piezo1: a comparison between whole-cell and patch recording. *Channels (Austin).* **6**, 282–289.

**Gradinaru, V., Thompson, K. R. and Deisseroth, K.** (2008). eNpHR: A Natronomonas halorhodopsin enhanced for optogenetic applications. *Brain Cell Biol.* **36**, 129–139.

**Grill, W. M., Norman, S. E. and Bellamkonda, R. V.** (2009). Implanted Neural Interfaces: Biochallenges and Engineered Solutions. *Annu. Rev. Biomed. Eng.* **11**, 1–24.

**Grossman, N., Bono, D., Dedic, N., Kodandaramaiah, S. B., Rudenko, A., Suk, H. J., Cassara, A. M., Neufeld, E., Kuster, N., Tsai, L. H., et al.** (2017). Noninvasive

Deep Brain Stimulation via Temporally Interfering Electric Fields. *Cell* **169**, 1029–1041.e16.

**Gu, Y. and Gu, C.** (2014). Physiological and Pathological Functions of Mechanosensitive Ion Channels. *Mol. Neurobiol.* **50**, 339–347.

**Hamill, O. P. and Martinac, B.** (2001). Molecular basis of mechanotransduction in living cells. *Physiol. Rev.* **81**, 685–740.

**Hanein, Y., Tadmor, O., Anava, S. and Ayali, A.** (2011). Neuronal soma migration is determined by neurite tension. *Neuroscience* **172**, 572–579.

**Harris, J. P., Capadona, J. R., Miller, R. H., Healy, B. C., Shanmuganathan, K., Rowan, S. J., Weder, C. and Tyler, D. J.** (2011). Mechanically adaptive intracortical implants improve the proximity of neuronal cell bodies. *J. Neural Eng.* **8**, 66011.

**Häse, C. C., Le Dain, A. C. and Martinac, B.** (1995). Purification and Functional Reconstitution of the Recombinant Large Mechanosensitive Ion Channel (MscL) of Escherichia coli. *J. Biol. Chem.* **270**, 18329–18334.

**Häse, C. C., Le Dain, A. C. and Martinac, B.** (1997). Molecular dissection of the large mechanosensitive ion channel (MscL) of E. coli: mutants with altered channel gating and pressure sensitivity. *J. Membr. Biol.* **157**, 17–25.

**Hertzberg, Y., Naor, O., Volovick, A. and Shoham, S.** (2010). Towards multifocal ultrasonic neural stimulation: pattern generation algorithms. *J. Neural Eng.* **7**, 56002.

**Heureaux, J., Chen, D., Murray, V. L., Deng, C. X. and Liu, A. P.** (2014). Activation of a Bacterial Mechanosensitive Channel in Mammalian Cells by Cytoskeletal Stress. *Cell. Mol. Bioeng.* **7**, 307–319.

**Ho, S.-Y., Chao, C.-Y., Huang, H.-L., Chiu, T.-W., Charoenkwan, P. and Hwang, E.** (2011). NeurphologyJ: an automatic neuronal morphology quantification method and its application in pharmacological discovery. *BMC Bioinformatics* **12**, 230.

**Hofherr, A., Fakler, B. and Klocker, N.** (2005). Selective Golgi export of Kir2.1 controls the stoichiometry of functional Kir2.x channel heteromers. *J Cell Sci* **118**, 1935–1943.

**Hong, K. and Driscoll, M.** (1994). A transmembrane domain of the putative channel subunit MEC-4 influences mechanotransduction and neurodegeneration in C. elegans. *Nature* **367**, 470–473.

**Honoré, E.** (2007). The neuronal background K2P channels: focus on TREK1. *Nat. Rev. Neurosci.* **8**, 251–261.

**Hua, J., Erickson, L. E., Yiin, T.-Y. and Glasgow, L. A.** (1993). A Review of the Effects of Shear and Interfacial Phenomena on Cell Viability. *Crit. Rev. Biotechnol.* **13**, 305–328.

**Hudspeth, A. J. and Jacobs, R.** (1979). Stereocilia mediate transduction in vertebrate hair cells (auditory system/cilium/vestibular system). *Proc. Natl. Acad. Sci. U. S. A.* **76**, 1506–9.

**Hughes, S., McBain, S., Dobson, J. and El Haj, A. J.** (2008). Selective activation of mechanosensitive ion channels using magnetic particles. *J. R. Soc. Interface* **5**, 855–63.

**Ibsen, S., Tong, A., Schutt, C., Esener, S. and Chalasani, S. H.** (2015). Sonogenetics is a non-invasive approach to activating neurons in Caenorhabditis elegans. *Nat. Commun.* **6**, 8264.

**Iscla, I. and Blount, P.** (2012). Sensing and responding to membrane tension: The bacterial MscL channel as a model system. *Biophys. J.*

**Iscla, I., Wray, R. and Blount, P.** (2008). On the Structure of the N-Terminal Domain of the MscL Channel: Helical Bundle or Membrane Interface. *Biophys. J.* **95**, 2283–

2291.
**Iscla, I., Eaton, C., Parker, J., Wray, R., Kovács, Z. and Blount, P.** (2013). Improving the design of a MscL-based triggered nanovalve. *Biosensors* **3**, 171–184.
**Iwashita, M., Kataoka, N., Toida, K. and Kosodo, Y.** (2014). Systematic profiling of spatiotemporal tissue and cellular stiffness in the developing brain. *Development* **141**, 3793–3798.
**Janmey, P. A. and McCulloch, C. A.** (2007). Cell Mechanics: Integrating Cell Responses to Mechanical Stimuli. *Annu. Rev. Biomed. Eng.* **9**, 1–34.
**Jiang, X., Yang, K., Yang, X., Liu, Y., Cheng, Y., Chen, X. and Tu, Y.** (2015). Elastic modulus affects the growth and differentiation of neural stem cells. *Neural Regen. Res.* **10**, 1523.
**Johns, L. D.** (2002). Nonthermal effects of therapeutic ultrasound: The frequency resonance hypothesis. *J. Athl. Train.* **37**, 293–299.
**Jorfi, M., Skousen, J. L., Weder, C. and Capadona, J. R.** (2015). Progress towards biocompatible intracortical microelectrodes for neural interfacing applications. *J. Neural Eng.* **12**, 11001.
**Kakuda, T., Koide, Y., Sakamoto, A. and Takai, S.** (2012). Characterization of two putative mechanosensitive channel proteins of Campylobacter jejuni involved in protection against osmotic downshock. *Vet. Microbiol.* **160**, 53–60.
**Kang, D., Choe, C. and Kim, D.** (2005). Thermosensitivity of the two-pore domain $K^+$ channels TREK-2 and TRAAK. *J. Physiol.* **564**, 103–116.
**Kaster, T., Sack, I. and Samani, A.** (2011). Measurement of the hyperelastic properties of ex vivo brain tissue slices. *J. Biomech.* **44**, 1158–1163.
**Kiessling, F., Fokong, S., Koczera, P., Lederle, W. and Lammers, T.** (2012). Ultrasound Microbubbles for Molecular Diagnosis, Therapy, and Theranostics. *J. Nucl. Med.* **53**, 345–348.
**Kim, E., Xia, Y. and Whitesides, G. M.** (1995). Polymer microstructures formed by moulding in capillaries. *Nature* **376**, 581–584.
**Kim, H., Chiu, A., Lee, S. D., Fischer, K. and Yoo, S.-S.** (2014). Focused Ultrasound-mediated Non-invasive Brain Stimulation: Examination of Sonication Parameters. *Brain Stimul.* **7**, 748–756.
**Kloda, A. and Martinac, B.** (2001). Molecular identification of a mechanosensitive channel in archaea. *Biophys. J.* **80**, 229–240.
**Kloda, A., Petrov, E., Meyer, G. R., Nguyen, T., Hurst, A. C., Hool, L. and Martinac, B.** (2008a). Mechanosensitive channel of large conductance. *Int. J. Biochem. Cell Biol.* **40**, 164–169.
**Kloda, A., Petrov, E., Meyer, G. R., Nguyen, T., Hurst, A. C., Hool, L. and Martinac, B.** (2008b). Mechanosensitive channel of large conductance. *Int. J. Biochem. Cell Biol.* **40**, 164–9.
**Kocer, A.** (2015). Mechanisms of mechanosensing — mechanosensitive channels, function and re-engineering. *Curr. Opin. Chem. Biol.* **29**, 120–127.
**Kocer, A., Walko, M., Meijberg, W. and Feringa, B. L.** (2005). A Light-Actuated Nanovalve Derived from a Channel Protein. *Science (80-. ).* **309**, 755–758.
**Köhler, R., Distler, A. and Hoyer, J.** (1999). Increased mechanosensitive currents in aortic endothelial cells from genetically hypertensive rats. *J. Hypertens.* **17**, 365–371.
**Koser, D. E., Thompson, A. J., Foster, S. K., Dwivedy, A., Pillai, E. K., Sheridan, G. K., Svoboda, H., Viana, M., Costa, L. da F., Guck, J., et al.** (2016a). Mechanosensing is critical for axon growth in the developing brain. *Nat. Neurosci.* **accepted**, 1–11.

**Koser, D. E., Thompson, A. J., Foster, S. K., Dwivedy, A., Pillai, E. K., Sheridan, G. K., Svoboda, H., Viana, M., Costa, L. da F., Guck, J., et al.** (2016b). Mechanosensing is critical for axon growth in the developing brain. *Nat. Neurosci.* **19**, 1592–1598.

**Kramer, I., Gomperts, B. and Tatham, P.** (2009). *Signal Transduction*. Second Ed. London: Press, Academic.

**Krasovitski, B., Frenkel, V., Shoham, S. and Kimmel, E.** (2011). Intramembrane cavitation as a unifying mechanism for ultrasound-induced bioeffects. *Proc. Natl. Acad. Sci. U. S. A.* **108**, 3258–63.

**Kubanek, J., Shi, J., Marsh, J., Chen, D., Deng, C. and Cui, J.** (2016). Ultrasound modulates ion channel currents. *Sci. Rep.* **6**, 24170.

**Kung, C., Martinac, B. and Sukharev, S.** (2010). Mechanosensitive Channels in Microbes. *Annu. Rev. Microbiol.* **64**, 313–329.

**Kuo, J.-C.** (2013). Mechanotransduction at focal adhesions: integrating cytoskeletal mechanics in migrating cells. *J. Cell. Mol. Med.* **17**, 704–12.

**Lamoureux, P., Ruthel, G., Buxbaum, R. E. and Heidemann, S. R.** (2002). Mechanical tension can specify axonal fate in hippocampal neurons. *J. Cell Biol.* **159**, 499–508.

**Lee, S. J., Sun, J., Flint, J. J., Guo, S., Xie, H. K., King, M. A. and Sarntinoranont, M.** (2011). Optically based-indentation technique for acute rat brain tissue slices and thin biomaterials. *J. Biomed. Mater. Res. - Part B Appl. Biomater.* **97 B**, 84–95.

**Lee, J. Y., Carugo, D., Crake, C., Owen, J., de Saint Victor, M., Seth, A., Coussios, C. and Stride, E.** (2015). Nanoparticle-Loaded Protein-Polymer Nanodroplets for Improved Stability and Conversion Efficiency in Ultrasound Imaging and Drug Delivery. *Adv. Mater.* **27**, 5484–5492.

**Legon, W., Sato, T. F., Opitz, A., Mueller, J., Barbour, A., Williams, A. and Tyler, W. J.** (2014). Transcranial focused ultrasound modulates the activity of primary somatosensory cortex in humans. *Nat. Neurosci.* **17**, 322–329.

**Lentacker, I., De Cock, I., Deckers, R., De Smedt, S. C. and Moonen, C. T. W.** (2014). Understanding ultrasound induced sonoporation: Definitions and underlying mechanisms. *Adv. Drug Deliv. Rev.* **72**, 49–64.

**Lesage, F., Terrenoire, C., Romey, G. and Lazdunski, M.** (2000). Human TREK2, a 2P Domain Mechano-sensitive K + Channel with Multiple Regulations by Polyunsaturated Fatty Acids, Lysophospholipids, and G s , G i , and G q Protein-coupled Receptors. *J. Biol. Chem.* **275**, 28398–28405.

**Levin, G. and Blount, P.** (2004). Cysteine Scanning of MscL Transmembrane Domains Reveals Residues Critical for Mechanosensitive Channel Gating. *Biophys. J.* **86**, 2862–2870.

**Levina, N., Totemeyer, S., Stokes, N. R., Louis, P., Jones, M. A. and Booth, I. R.** (1999). Protection of Escherichia coli cells against extreme turgor by activation of MscS and MscL mechanosensitive channels: identification of genes required for MscS activity. *EMBO J.* **18**, 1730–1737.

**Lewis, A. H. and Grandl, J.** (2015). Mechanical sensitivity of Piezo1 ion channels can be tuned by cellular membrane tension. *Elife* **4**,.

**Li, D., Takimoto, K. and Levitan, E. S.** (2000). Surface expression of Kv1 channels is governed by a C-terminal motif. *J. Biol. Chem.* **275**, 11597–11602.

**Li, T., Chen, Y. and Ma, J.** (2009). Development of a miniaturized piezoelectric ultrasonic transducer. *IEEE Trans. Ultrason. Ferroelectr. Freq. Control* **56**, 649–659.

**Li, W., Kang, L., Piggott, B. J., Feng, Z. and Xu, X. Z. S.** (2011). The neural circuits

and sensory channels mediating harsh touch sensation in Caenorhabditis elegans. *Nat. Commun.* **2**, 315.

**Li, G.-F., Zhao, H.-X., Zhou, H., Yan, F., Wang, J.-Y., Xu, C.-X., Wang, C.-Z., Niu, L.-L., Meng, L., Wu, S., et al.** (2016). Improved Anatomical Specificity of Non-invasive Neuro-stimulation by High Frequency (5 MHz) Ultrasound. *Sci. Rep.* **6**, 24738.

**Lin, S. Y. and Corey, D. P.** (2005). TRP channels in mechanosensation. *Curr. Opin. Neurobiol.* **15**, 350–357.

**Liu, Z., Gandhi, C. S. and Rees, D. C.** (2009). Structure of a tetrameric MscL in an expanded intermediate state. *Nature* **461**, 120–124.

**Maingret, F., Fosset, M., Lesage, F., Lazdunski, M. and Honoré, E.** (1999). TRAAK is a mammalian neuronal mechano-gated K+ channel. *J. Biol. Chem.* **274**, 1381–1387.

**Maingret, F., Patel, A. J., Lesage, F., Lazdunski, M. and Honoré, E.** (2000). Lysophospholipids open the two-pore domain mechano-gated K(+) channels TREK-1 and TRAAK. *J. Biol. Chem.* **275**, 10128–33.

**Maingret, F., Honoré, E., Lazdunski, M. and Patel, A. J.** (2002). Molecular Basis of the Voltage-Dependent Gating of TREK-1, a Mechano-Sensitive K+ Channel. *Biochem. Biophys. Res. Commun.* **292**, 339–346.

**Maniotis, A. J., Chen, C. S. and Ingber, D. E.** (1997). Demonstration of mechanical connections between integrins, cytoskeletal filaments, and nucleoplasm that stabilize nuclear structure. *Proc. Natl. Acad. Sci. U. S. A.* **94**, 849–54.

**Marino, A., Arai, S., Hou, Y., Sinibaldi, E., Pellegrino, M., Chang, Y., Mazzolai, B., Mattoli, V., Suzuki, M. and Ciofani, G.** (2015). Piezoelectric Nanoparticle-Assisted Wireless Neuronal Stimulation. *ACS Nano* **9**, 7678–7689.

**Marino, A., Arai, S., Hou, Y., Degl'Innocenti, A., Cappello, V., Mazzolai, B., Chang, Y. T., Mattoli, V., Suzuki, M. and Ciofani, G.** (2017). Gold Nanoshell-Mediated Remote Myotube Activation. *ACS Nano* **11**, 2494–2505.

**Martinac, B.** (2004). Mechanosensitive ion channels: molecules of mechanotransduction. *J. Cell Sci.* **117**, 2449–2460.

**Martinac, B.** (2012). An evolutionary and scientific tour de force in mechanobiology. *Channels* **6**, 211–213.

**Martinac, B.** (2014). The ion channels to cytoskeleton connection as potential mechanism of mechanosensitivity. *Biochim. Biophys. Acta - Biomembr.* **1838**, 682–691.

**Martinac, B. and Kloda, A.** (2003). Evolutionary origins of mechanosensitive ion channels. *Prog. Biophys. Mol. Biol.* **82**, 11–24.

**Martinac, B., Buechner, M., Delcour, A. H., Adler, J. and Kung, C.** (1987). Pressure-sensitive ion channel in Escherichia coli. *Proc. Natl. Acad. Sci.* **84**, 2297–2301.

**Martinac, B., Nomura, T., Chi, G., Petrov, E., Rohde, P. R., Battle, A. R., Foo, A., Constantine, M., Rothnagel, R., Carne, S., et al.** (2014). Bacterial mechanosensitive channels: models for studying mechanosensory transduction. *Antioxid. Redox Signal.* **20**, 952–69.

**Matus, A.** (2000). Actin-Based Plasticity in Dendritic Spines. *Science (80-. ).* **290**, 754–758.

**Maurer, J. A. and Dougherty, D. A.** (2003). Generation and Evaluation of a Large Mutational Library from the Escherichia coli Mechanosensitive Channel of Large Conductance, MscL. *J. Biol. Chem.* **278**, 21076–21082.

**Mazumder, A., Roopa, T., Basu, A., Mahadevan, L. and Shivashankar, G. V.** (2008). Dynamics of Chromatin Decondensation Reveals the Structural Integrity of a

Mechanically Prestressed Nucleus. *Biophys. J.* **95**, 3028–3035.
**Meister, M.** (2016). Physical limits to magnetogenetics. *Elife* **5**,.
**Menz, M. D., Oralkan, O., Khuri-Yakub, P. T. and Baccus, S. A.** (2013). Precise Neural Stimulation in the Retina Using Focused Ultrasound. *J. Neurosci.* **33**, 4550–4560.
**Meyer, G. R., Gullingsrud, J., Schulten, K. and Martinac, B.** (2006). Molecular Dynamics Study of MscL Interactions with a Curved Lipid Bilayer. *Biophys. J.* **91**, 1630–1637.
**Miller, D. L., Smith, N. B., Bailey, M. R., Czarnota, G. J., Hynynen, K., Makin, I. R. S. and Bioeffects Committee of the American Institute of Ultrasound in Medicine** (2012). Overview of therapeutic ultrasound applications and safety considerations. *J. Ultrasound Med.* **31**, 623–34.
**Moe, P. and Blount, P.** (2005). Assessment of Potential Stimuli for Mechano-Dependent Gating of MscL: Effects of Pressure, Tension, and Lipid Headgroups. *Biochemistry* **44**, 12239–12244.
**Moore, S. W. and Sheetz, M. P.** (2011). Biophysics of substrate interaction: Influence on neural motility, differentiation, and repair. *Dev. Neurobiol.* **71**, 1090–1101.
**Morris, C. E. and Horn, R.** (1991). Failure to Elicit Neuronal Macroscopic Mechanosensitive Currents Anticipated by Single- Channel Studies. **251**, 1246–1249.
**Mukhopadhyay, R., Kumar, S. and Hoh, J. H.** (2004). Molecular mechanisms for organizing the neuronal cytoskeleton. *BioEssays* **26**, 1017–1025.
**Murphy, M. C., Huston, J., Jack, C. R., Glaser, K. J., Manduca, A., Felmlee, J. P. and Ehman, R. L.** (2011). Decreased brain stiffness in Alzheimer's disease determined by magnetic resonance elastography. *J. Magn. Reson. Imaging* **34**, 494–498.
**Nelson, T. R., Fowlkes, J. B., Abramowicz, J. S. and Church, C. C.** (2009). Ultrasound Biosafety Considerations for the Practicing Sonographer and Sonologist. *J. Ultrasound Med.* **28**, 139–150.
**Neukirchen, D. and Bradke, F.** (2011). Neuronal polarization and the cytoskeleton. *Semin. Cell Dev. Biol.* **22**, 825–33.
**Nicholson-Dykstra, S., Higgs, H. N. and Harris, E. S.** (2005). Actin dynamics: growth from dendritic branches. *Curr. Biol.* **15**, R346-57.
**Nomura, T., Cranfield, C. G., Deplazes, E., Owen, D. M., Macmillan, A., Battle, A. R., Constantine, M., Sokabe, M. and Martinac, B.** (2012). Differential effects of lipids and lyso-lipids on the mechanosensitivity of the mechanosensitive channels MscL and MscS. *Proc. Natl. Acad. Sci.* **109**, 8770–8775.
**Norman, L. L. and Aranda-Espinoza, H.** (2010). Cortical neuron outgrowth is insensitive to substrate stiffness. *Cell. Mol. Bioeng.* **3**, 398–414.
**North, R. A.** (1996). Families of ion channels with two hydrophobic segments. *Curr. Opin. Cell Biol.* **8**, 474–483.
**Nourse, J. L. and Pathak, M. M.** (2017). How cells channel their stress: Interplay between Piezo1 and the cytoskeleton. *Semin. Cell Dev. Biol.* **71**, 3–12.
**O'Brien Jr., W.** (2007). Ultrasound–biophysics mechanisms. *Prog. Biophys. Mol. Biol.* **93**, 212–255.
**Paefgen, V., Doleschel, D. and Kiessling, F.** (2015). Evolution of contrast agents for ultrasound imaging and ultrasound-mediated drug delivery. *Front. Pharmacol.* **6**, 1–16.
**Palazzolo, G., Moroni, M., Soloperto, A., Aletti, G., Naldi, G., Vassalli, M., Nieus, T. and Difato, F.** (2017). Fast wide-volume functional imaging of engineered in vitro

brain tissues. *Sci. Rep.* **7**, 8499.
**Panzeri, S., Harvey, C. D., Piasini, E., Latham, P. E. and Fellin, T.** (2017). Cracking the Neural Code for Sensory Perception by Combining Statistics, Intervention, and Behavior. *Neuron* **93**, 491–507.
**Patel, A. J., Honoré, E., Maingret, F., Lesage, F., Fink, M., Duprat, F. and Lazdunski, M.** (1998). A mammalian two pore domain mechano-gated S-like K+ channel. *EMBO J.* **17**, 4283–4290.
**Perozo, E.** (2006). Gating prokaryotic mechanosensitive channels. *Nat. Rev. Mol. Cell Biol.* **7**, 109–119.
**Perozo, E., Kloda, A., Cortes, D. M. and Martinac, B.** (2002a). Physical principles underlying the transduction of bilayer deformation forces during mechanosensitive channel gating. *Nat. Struct. Biol.* **9**, 696–703.
**Perozo, E., Cortes, D. M., Sompornpisut, P., Kloda, A. and Martinac, B.** (2002b). Open channel structure of MscL and the gating mechanism of mechanosensitive channels. *Nature* **418**, 942–948.
**Peyronnet, R., Tran, D., Girault, T. and Frachisse, J.-M.** (2014). Mechanosensitive channels: feeling tension in a world under pressure. *Front. Plant Sci.* **5**, 1–14.
**Plaksin, M., Kimmel, E. and Shoham, S.** (2016). Cell-Type-Selective Effects of Intramembrane Cavitation as a Unifying Theoretical Framework for Ultrasonic Neuromodulation. *eNeuro* **3**, 1–16.
**Pliotas, C., Dahl, A. C. E., Rasmussen, T., Mahendran, K. R., Smith, T. K., Marius, P., Gault, J., Banda, T., Rasmussen, A., Miller, S., et al.** (2015). The role of lipids in mechanosensation. *Nat. Struct. Mol. Biol.* **22**, 991–998.
**Poole, K., Moroni, M. and Lewin, G. R.** (2014). Sensory mechanotransduction at membrane-matrix interfaces. *Pflugers Arch. Eur. J. Physiol.* **467**, 121–132.
**Postema, M., van Wamel, A., Lancée, C. T. and de Jong, N.** (2004). Ultrasound-induced encapsulated microbubble phenomena. *Ultrasound Med. Biol.* **30**, 827–840.
**Prager-Khoutorsky, M., Khoutorsky, A. and Bourque, C. W.** (2014). Unique Interweaved Microtubule Scaffold Mediates Osmosensory Transduction via Physical Interaction with TRPV1. *Neuron* **83**, 866–878.
**Reed, A., Kohl, P. and Peyronnet, R.** (2014). Molecular candidates for cardiac stretch-activated ion channels. *Glob. Cardiol. Sci. Pract.* **2014**, 9–25.
**Renema, W. K. J., Kan, H. E., Wieringa, B. and Heerschap, A.** (2007). In vivo magnetic resonance spectroscopy of transgenic mouse models with altered high-energy phosphoryl transfer metabolism. *NMR Biomed.* **20**, 448–467.
**Rezayat, E. and Toostani, I. G.** (2016). A review on brain stimulation using low intensity focused ultrasound. *Basic Clin. Neurosci.* **7**, 187–194.
**Richman, D. P., Stewart, M. R., Hutchinson, J. W. and Caviness, V. S.** (1975). Mechanical model of brain convolutional development. *Science (80-. ).* **189**, 18–21.
**Riek, K., Millward, J. M., Hamann, I., Mueller, S., Pfueller, C. F., Paul, F., Braun, J., Infante-Duarte, C. and Sack, I.** (2012). Magnetic resonance elastography reveals altered brain viscoelasticity in experimental autoimmune encephalomyelitis. *NeuroImage Clin.* **1**, 81–90.
**Rivnay, J., Wang, H., Fenno, L., Deisseroth, K. and Malliaras, G. G.** (2017). Next-generation probes, particles, and proteins for neural interfacing. *Sci. Adv.* **3**, e1601649.
**Ronan, L., Voets, N., Rua, C., Alexander-Bloch, A., Hough, M., Mackay, C., Crow, T. J., James, A., Giedd, J. N. and Fletcher, P. C.** (2014). Differential tangential expansion as a mechanism for cortical gyrification. *Cereb. Cortex* **24**, 2219–2228.
**Rosholm, K. R., Baker, M. A. B., Ridone, P., Nakayama, Y., Rohde, P. R., Cuello, L.**

**G., Lee, L. K. and Martinac, B.** (2017). Activation of the mechanosensitive ion channel MscL by mechanical stimulation of supported Droplet-Hydrogel bilayers. *Sci. Rep.* **7**, 1–10.

**Roudaut, Y., Lonigro, A., Coste, B., Hao, J., Delmas, P. and Crest, M.** (2012). Functional organization and molecular determinants of mechanosensitive receptors. *Channels* **6**, 234–245.

**Sack, I., Beierbach, B., Wuerfel, J., Klatt, D., Hamhaber, U., Papazoglou, S., Martus, P. and Braun, J.** (2009). The impact of aging and gender on brain viscoelasticity. *Neuroimage* **46**, 652–657.

**Sandoz, G., Douguet, D., Chatelain, F., Lazdunski, M. and Lesage, F.** (2009). Extracellular acidification exerts opposite actions on TREK1 and TREK2 potassium channels via a single conserved histidine residue. *Proc. Natl. Acad. Sci. U. S. A.* **106**, 14628–14633.

**Sassaroli, E. and Vykhodtseva, N.** (2016). Acoustic neuromodulation from a basic science prospective. *J. Ther. Ultrasound* **4**, 17.

**Sboros, V.** (2008). Response of contrast agents to ultrasound. *Adv. Drug Deliv. Rev.* **60**, 1117–1136.

**Scarcelli, T., Jordão, J. F., O'Reilly, M. A., Ellens, N., Hynynen, K. and Aubert, I.** (2014). Stimulation of Hippocampal Neurogenesis by Transcranial Focused Ultrasound and Microbubbles in Adult Mice. *Brain Stimul.* **7**, 304–307.

**Schindelin, J., Rueden, C. T., Hiner, M. C. and Eliceiri, K. W.** (2015). The ImageJ ecosystem: An open platform for biomedical image analysis. *Mol. Reprod. Dev.* **82**, 518–529.

**Shapiro, M. G., Goodwill, P. W., Neogy, A., Yin, M., Foster, F. S., Schaffer, D. V. and Conolly, S. M.** (2014). Biogenic gas nanostructures as ultrasonic molecular reporters. *Nat. Nanotechnol.* **9**, 311–316.

**Shapovalov, G. and Lester, H. A.** (2004). Gating Transitions in Bacterial Ion Channels Measured at 3 μs Resolution. *J. Gen. Physiol.* **124**, 151–161.

**Shulyakov, A. V., Fernando, F., Cenkowski, S. S. and Del Bigio, M. R.** (2009). Simultaneous determination of mechanical properties and physiologic parameters in living rat brain. *Biomech. Model. Mechanobiol.* **8**, 415–425.

**Siechen, S., Yang, S., Chiba, A. and Saif, T.** (2009). Mechanical tension contributes to clustering of neurotransmitter vesicles at presynaptic terminals. *Proc. Natl. Acad. Sci.* **106**, 12611–12616.

**Soloperto, A., Bisio, M., Palazzolo, G., Chiappalone, M., Bonifazi, P. and Difato, F.** (2016). Modulation of Neural Network Activity through Single Cell Ablation: An in Vitro Model of Minimally Invasive Neurosurgery. *Molecules* **21**, 1018.

**Stockklausner, C., Ludwig, J., Ruppersberg, J. . and Klöcker, N.** (2001). A sequence motif responsible for ER export and surface expression of Kir2.0 inward rectifier K + channels. *FEBS Lett.* **493**, 129–133.

**Streitberger, K. J., Sack, I., Krefting, D., Pfüller, C., Braun, J., Paul, F. and Wuerfel, J.** (2012). Brain viscoelasticity alteration in chronic-progressive multiple sclerosis. *PLoS One* **7**,.

**Suchyna, T. M., Markin, V. S. and Sachs, F.** (2009). Biophysics and structure of the patch and the gigaseal. *Biophys. J.* **97**, 738–747.

**Sukharev, S.** (2002). Purification of the Small Mechanosensitive Channel of Escherichia coli (MscS): the Subunit Structure, Conduction, and Gating Characteristicsin Liposomes. *Biophys. J.* **83**, 290–298.

**Sukharev, S. I., Martinac, B., Arshavsky, V. Y. and Kung, C.** (1993). Two types of mechanosensitive channels in the Escherichia coli cell envelope: solubilization and

functional reconstitution. *Biophys. J.* **65**, 177–183.
**Sukharev, S. I., Blount, P., Martinac, B., Blattner, F. R. and Kung, C.** (1994). A large-conductance mechanosensitive channel in E. coli encoded by mscL alone. *Nature* **368**, 265–268.
**Sukharev, S. I., Blount, P., Martinac, B. and Kung, and C.** (1997). MECHANOSENSITIVE CHANNELS OF ESCHERICHIA COLI :The MscL Gene, Protein, and Activities. *Annu. Rev. Physiol.* **59**, 633–657.
**Sukharev, S. I., Sigurdson, W. J., Kung, C. and Sachs, F.** (1999). Energetic and Spatial Parameters for Gating of the Bacterial Large Conductance Mechanosensitive Channel, MscL. *J. Gen. Physiol.* **113**, 525–540.
**Sukharev, S., Durell, S. R. and Guy, H. R.** (2001). Structural Models of the MscL Gating Mechanism. *Biophys. J.* **81**, 917–936.
**Tallinen, T., Chung, J. Y., Rousseau, F., Girard, N., Lefèvre, J. and Mahadevan, L.** (2016). On the growth and form of cortical convolutions. *Nat. Phys.* **12**, 588–593.
**Tay, A. and Di Carlo, D.** (2017). Magnetic Nanoparticle-Based Mechanical Stimulation for Restoration of Mechano-Sensitive Ion Channel Equilibrium in Neural Networks. *Nano Lett.* **17**, 886–892.
**Tay, A., Kunze, A., Murray, C. and Di Carlo, D.** (2016). Induction of Calcium Influx in Cortical Neural Networks by Nanomagnetic Forces. *ACS Nano* **10**, 2331–2341.
**Teng, J., Loukin, S., Anishkin, A. and Kung, C.** (2015). The force-from-lipid (FFL) principle of mechanosensitivity, at large and in elements. *Pflügers Arch. - Eur. J. Physiol.* **467**, 27–37.
**Tofangchi, A., Fan, A. and Saif, M. T. A.** (2016). Mechanism of Axonal Contractility in Embryonic Drosophila Motor Neurons In Vivo. *Biophys. J.* **111**, 1519–1527.
**Tsai, I.-J., Liu, Z.-W., Rayment, J., Norman, C., McKinley, A. and Martinac, B.** (2005). The role of the periplasmic loop residue glutamine 65 for MscL mechanosensitivity. *Eur. Biophys. J.* **34**, 403–412.
**Tufail, Y., Matyushov, A., Baldwin, N., Tauchmann, M. L., Georges, J., Yoshihiro, A., Tillery, S. I. H. and Tyler, W. J.** (2010). Transcranial Pulsed Ultrasound Stimulates Intact Brain Circuits. *Neuron* **66**, 681–694.
**Tufail, Y., Yoshihiro, A., Pati, S., Li, M. M. and Tyler, W. J.** (2011). Ultrasonic neuromodulation by brain stimulation with transcranial ultrasound. *Nat. Protoc.* **6**, 1453–1470.
**Tyler, W. J.** (2011). Noninvasive neuromodulation with ultrasound? A continuum mechanics hypothesis. *Neuroscientist* **17**, 25–36.
**Tyler, W. J.** (2012). The mechanobiology of brain function. *Nat. Rev. Neurosci.* **13**, 867–878.
**Tyler, W. J., Tufail, Y., Finsterwald, M., Tauchmann, M. L., Olson, E. J. and Majestic, C.** (2008). Remote Excitation of Neuronal Circuits Using Low-Intensity, Low-Frequency Ultrasound. *PLoS One* **3**, e3511.
**Tyler, W. J., Tufail, Y. and Pati, S.** (2010). Pain: Noninvasive functional neurosurgery using ultrasound. *Nat. Rev. Neurol.* **6**, 13–14.
**Ursell, T., Agrawal, A. and Phillips, R.** (2011). Lipid bilayer mechanics in a pipette with glass-bilayer adhesion. *Biophys. J.* **101**, 1913–1920.
**Vanbavel, E.** (2007). Effects of shear stress on endothelial cells: Possible relevance for ultrasound applications. *Prog. Biophys. Mol. Biol.* **93**, 374–383.
**Wang, Y. and Guo, L.** (2016). Nanomaterial-enabled neural stimulation. *Front. Neurosci.* **10**, 1–7.
**Wang, N., Tytell, J. D. and Ingber, D. E.** (2009). Mechanotransduction at a distance: mechanically coupling the extracellular matrix with the nucleus. *Nat. Rev. Mol. Cell*

*Biol.* **10**, 75–82.

**Wells, J., Kao, C., Mariappan, K., Albea, J., Jansen, E. D., Konrad, P. and Mahadevan-Jansen, A.** (2005). Optical stimulation of neural tissue in vivo. *Opt. Lett.* **30**, 504–6.

**Wheeler, M. A., Smith, C. J., Ottolini, M., Barker, B. S., Purohit, A. M., Grippo, R. M., Gaykema, R. P., Spano, A. J., Beenhakker, M. P., Kucenas, S., et al.** (2016). Genetically targeted magnetic control of the nervous system. *Nat. Neurosci.* **19**, 756–761.

**Whitesides, G. M.** (2006). The origins and the future of microfluidics. *Nature* **442**, 368–373.

**Woe, P. C., Blount, P. and Kung, C.** (1998). Functional and structural conservation in the mechanosensitive channel MscL implicates elements crucial for mechanosensation. *Mol. Microbiol.* **28**, 583–592.

**Wu, J. and Nyborg, W. L.** (2008). Ultrasound, cavitation bubbles and their interaction with cells. *Adv. Drug Deliv. Rev.* **60**, 1103–1116.

**Wu, J., Ross, J. P. and Chiu, J.-F.** (2002). Reparable sonoporation generated by microstreaming. *J. Acoust. Soc. Am.* **111**, 1460–1464.

**Wu, J., Lewis, A. H. and Grandl, J.** (2017). Touch, Tension, and Transduction – The Function and Regulation of Piezo Ion Channels. *Trends Biochem. Sci.* **42**, 57–71.

**Yang, L.-M., Wray, R., Parker, J., Wilson, D., Duran, R. S. and Blount, P.** (2012). Three Routes To Modulate the Pore Size of the MscL Channel/Nanovalve. *ACS Nano* **6**, 1134–1141.

**Yang, L.-M., Zhong, D. and Blount, P.** (2013). Chimeras Reveal a Single Lipid-Interface Residue that Controls MscL Channel Kinetics as well as Mechanosensitivity. *Cell Rep.* **3**, 520–527.

**Yao, M., Qiu, W., Liu, R., Efremov, A. K., Cong, P., Seddiki, R., Payre, M., Lim, C. T., Ladoux, B., Mège, R.-M., et al.** (2014). Force-dependent conformational switch of α-catenin controls vinculin binding. *Nat. Commun.* **5**,.

**Ye, P. P., Brown, J. R. and Pauly, K. B.** (2016a). Frequency dependence of ultrasound neurostimulation in the mouse brain. *Ultrasound Med. Biol.* **42**, 1512–1530.

**Ye, P. P., Brown, J. R. and Pauly, K. B.** (2016b). Frequency dependence of ultrasound neurostimulation in the mouse brain. *Ultrasound Med. Biol.*

**Yoo, S.-S., Bystritsky, A., Lee, J.-H., Zhang, Y., Fischer, K., Min, B.-K., McDannold, N. J., Pascual-Leone, A. and Jolesz, F. A.** (2011). Focused ultrasound modulates region-specific brain activity. *Neuroimage* **56**, 1267–1275.

**Yoshimura, K. and Sokabe, M.** (2010). Mechanosensitivity of ion channels based on protein-lipid interactions. *J. R. Soc. Interface* **7**, S307–S320.

**Yoshimura, K., Batiza, A., Schroeder, M., Blount, P. and Kung, C.** (1999). Hydrophilicity of a single residue within MscL correlates with increased channel mechanosensitivity. *Biophys. J.* **77**, 1960–72.

**Younan, Y., Deffieux, T., Larrat, B., Fink, M., Tanter, M. and Aubry, J.-F.** (2013). Influence of the pressure field distribution in transcranial ultrasonic neurostimulation. *Med. Phys.* **40**, 82902.

**Zanzotto, A., Szita, N., Boccazzi, P., Lessard, P., Sinskey, A. J. and Jensen, K. F.** (2004). Membrane-aerated microbioreactor for high-throughput bioprocessing. *Biotechnol. Bioeng.* **87**, 243–254.

**Zhang, H. and Labouesse, M.** (2012). Signalling through mechanical inputs - a coordinated process. *J. Cell Sci.* **125**, 4172–4172.

**Zhang, Q.-Y., Zhang, Y.-Y., Xie, J., Li, C.-X., Chen, W.-Y., Liu, B.-L., Wu, X., Li, S.-N., Huo, B., Jiang, L.-H., et al.** (2015). Stiff substrates enhance cultured

neuronal network activity. *Sci. Rep.* **4**, 6215.
**Zheng, J.** (2013). Molecular Mechanism of TRP Channels. *Compr Physiol* **3**, 221–242.
**Zhou, W., Wang, J., Wang, K., Huang, B., Niu, L., Li, F., Cai, F., Chen, Y., Liu, X., Zhang, X., et al.** (2017). Ultrasound neuro-modulation chip: activation of sensory neurons in Caenorhabditis elegans by surface acoustic waves. *Lab Chip* **17**, 1725–1731.